



Aristotle University of Thessaloniki
School of Natural Sciences
Department of Geology- Geophysics Sector

Angelos Plageras

Mineral Resources Engineer

Geophysical Prospection of Underwater Archaeological Sites in
Greece

Master Thesis

Scientific Advisory Committee:

Dr. Nikos Papadopoulos, Researcher A, Supervisor

Professor Panagiotis Tsourlos, Scientific Advisory Committee Member

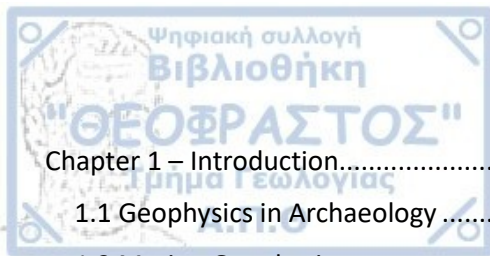
Professor Grigoris Tsokas, Scientific Advisory Committee Member

Thessaloniki 2022

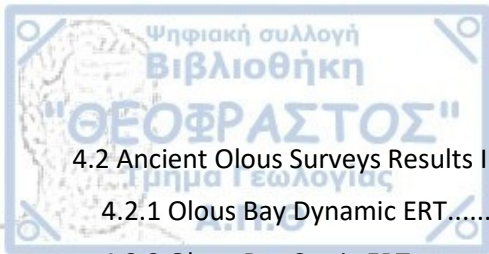


To my mother Argyro, my father Dimitris and my partner Eleni

"Together we stand, divided we fall"



Chapter 1 – Introduction.....	1
1.1 Geophysics in Archaeology	1
1.2 Marine Geophysics.....	2
1.3 Thesis Purpose	4
1.4 Study Areas	5
1.4.1 Ancient Olous.....	6
1.4.2 Delos Island	9
Chapter 2 – Methodology	13
2.1 Introduction	13
2.2 Electrical Resistivity Tomography	13
2.2.1 Basic Principles.....	13
2.2.2 Data Collection.....	17
2.2.2.1 Bathymetry	17
2.2.2.2 Dynamic ERT	19
2.2.2.3 Static ERT.....	22
2.3 Multisensor Magnetic Gradiometry.....	23
2.3.1 Basic Principles.....	23
2.3.2 Data Collection.....	25
Chapter 3 – Data Processing and Results.....	27
3.1 ERT Data Processing.....	27
3.2 ERT Coverage and Results.....	38
3.2.1 Skhardanas Dynamic ERT	38
3.2.2 Olous Dynamic ERT	45
3.2.3 Olous Static ERT	49
3.3 Multisensor Magnetic Gradiometry Processing	52
3.4 Multisensor Magnetic Gradiometry Results	59
3.5 Bathymetry Results	61
3.5.1 Skhardanas Bay Bathymetric Results.....	61
3.5.2 Ancient Olous Bathymetric Results.....	62
Chapter 4 - Interpretation.....	63
4.1 Delos Island Surveys Results Interpretation	63
4.1.1 Skhardanas Bay Dynamic ERT	63
4.1.2 Stadio Bay: Magnetic Gradiometry	67



4.2 Ancient Olous Surveys Results Interpretation	69
4.2.1 Olous Bay Dynamic ERT.....	69
4.2.2 Olous Bay Static ERT.....	75
Chapter 5 – Conclusions.....	81
References	84
Appendix A : Results of 2D Inversion of the Skhardanas Data Set	87
Appendix B – Inversion parameters.....	102
1) Skhardanas and Static Olous data sets Inversion Parameters.....	102
2) Dynamic Olous Data Set Inversion Parameters	107



Abstract

The main subject of this thesis is the use of different geophysical techniques in the prospection of two underwater archaeological sites in Greece. The purpose of this thesis is to showcase those techniques, to test their effectiveness in underwater archaeological prospecting and to make a contribution to the field of shallow marine geophysics and in geophysics in general.

For that purpose, the Electrical Resistivity Tomography (ERT) and the multisensor magnetic gradiometry methods were selected. The study areas were the island of Delos and the bay of ancient Olous in Elounda, Crete. Two differentiations of the ERT method were used, the dynamic mode in the bay of Skhardanas in Delos and in the south bay of Ancient Olous and the static variant in the north bay of Ancient Olous. The magnetic gradiometry technique was used in Stadio bay, in Delos Island.

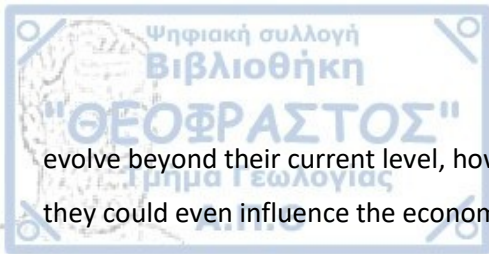
In the first chapter, a brief introduction regarding the use of geophysics in archaeological research (archaeometry) and marine geophysics is given. The main goals of the thesis are explained and finally a description of the study areas is outlined, focusing on both their history as well as their general geological setting.

In the second chapter the methodology behind the surveys is explained. This includes the basic principles of each technique, the instrumentation and all the steps followed during the in situ data collection.

The third chapter gives an overview of all the processing stages the data sets had to undergo before they could be safely interpreted. After the processing description for each used technique, the respective results and geophysical images are also presented.

In the fourth chapter, an interpretation of the results is given. The focus of the interpretation is mainly archaeological, but some geological information could also be extracted. The results in all four surveys successfully managed to pinpoint many targets of archaeological value, some of which could be ground proofed from an in-situ inspection, while others are buried below the seabed and would require an underwater excavation to verify them.

Finally, the fifth chapter draws some conclusions regarding the effectiveness of the methods used in the surveys, the future of shallow marine geophysics in solving archaeological problems, how they could



evolve beyond their current level, how they can help in the progress of archaeological surveys, and how they could even influence the economic life of the local communities.



First of all, I want to thank Dr. Nikos Papadopoulos from the bottom of my heart, not only for being my scientific supervisor during this last year, not only for the constant advise and care he showed for me during the course of this master that without them this thesis could never be materialized, but also because he showed me that we are human beings first and researchers second.

Next, I want to thank Professor Panagiotis Tsourlos for his participation in my advisory committee, for all those things he taught me during my first year in this master, and most of all because he believed in me. I also want to thank Professor Grigoris Tsokas for his participation in my advisory committee and for his teachings.

I want to thank all the members of GEOSAT research lab for showing me an excellent working environment and the Institute of Mediterranean Studies in Rethymno for allowing me to use their state-of-the-art facilities and equipment, without which this study could never be completed.

A special thanks is due to Dimitrios Oikonomou for his contribution of some of the codes used in the data processing, his moral encouragement and his friendly advice.

Concerning the Delos survey, I want to thank Prof. Mantha Zarmakoupi and the Ecole Francaise d' Athenes for allowing me to use the data sets for this thesis, Magda Athanasoula, archaeologist from the Ephorate of Underwater Antiquities, for her help during the period we stayed on Delos Island. Regarding data collection I want to thank Dr. Nikos Papadopoulos, Dimitrios Oikonomou and Dr. Nasos Argyriou.

Concerning the Olous survey, I want to thank the Ephorate of Underwater Antiquities and especially Dr. Theotokis Theodoulou for allowing me to use the data sets for this thesis. The data collection was completed with the help of Dr. Nikos Papadopoulos, Dimitrios Oikonomou, Dr. Kleanthis Simyrdanis, Dr. Gianluca Cantoro, Dr. Nasos Argyriou and Dr. Christos Polykretis.

Next, I want to express my gratitude to my friends and co-students in this master Georgios Psathas, Eleni Mπαρκα and Evangelia Georgakopoulou for their constant help and support during this two-year endeavor. You helped me climb a mountain I never could have climbed alone. I also want to thank MSc student Georgios Tsoungaris, who also helped and supported me during this time.



Finally, I want to thank my family: my father Dimitris, my mother Argyro and my partner and comrade Eleni. Their love and their constant support help me become better every day. Nothing would be possible without them.



Chapter 1– Introduction

1.1 Geophysics in Archaeology

Applied Geophysics can be defined as the scientific and research subdomain that measures the physical quantities of the subsurface in order to determine the variation of physical parameters in Earth's interior (Tsokas et al. 2007). A wide range of diverse geophysical methods have been introduced throughout the years which can be widely categorized as electrical, electromagnetic, magnetic, seismic and gravity depending on the physical quantities that are measured. Thus, the applications of these methods are numerous including the detection of mineral deposits (Combes et al. 2022), the discovery of underground water aquifers (Aguila et al. 2022), the mapping of structures related to oil deposits (Sharma et al. 2021), geological mapping (Osorio-Granada et al. 2022), geotechnical applications (Orfanos et al. 2022), glaciometry (Onaka et al. 2022) and reconstructing the Archaeoenvironment (Fukuyo et al. 2020) among others.

After World War II, the application of natural sciences in order to solve various archaeological, historical and anthropological problems gained significant attraction and interest in the scientific community. The collective use of these methods and techniques in the field of archaeological prospection referred as Archaeophysics. At the end of the 1950's the more accurate term of Archaeometry was first used by the Research Laboratory for Archaeology and the History of Art at Oxford University, a term that is used until this day. The term prospection was also introduced, at first to describe all those techniques and exploits sharing the same goal of uncovering the buried past. This term became later synonymous with archaeometry (Tsokas et al. 2007, Linford 2006).

The first geophysical method used to solve a specific archaeological problem was the geoelectrical mapping in 1938 in a site of a suspected buried vault near the Bruton Parish Church at Williamsburg, Virginia, USA. Despite the non-conclusive results for the location of buried archeological structures its innovation character is evident as it opened in a new era in archaeological prospection. The first fully archaeological geophysical survey took place in 1946 by Atkinson in a Neolithic site near Dorchester-on-Thames. The geoelectrical mapping method was also used, this time successfully pinpointing a buried ditch which was later excavated. The magnetic method was introduced later, in 1958 again by Atkinson.

Decades later, the GPR (ground penetrating radar) method and the ERT (electrical resistivity tomography) method were also very successfully introduced in archaeological prospection. These are the four primary geophysical methods used in archaeometry, with some of the supplementary methods being the seismic and self-potential methods. Table 1 below illustrates all the geophysical methods used in archaeological research (Gaffney 2007, Linford 2006)

<i>Method</i>	<i>Active or passive</i>	<i>Frequency of use</i>
Magnetometry	Passive	High
Electrical resistance/resistivity	Active	High
Ground penetrating radar	Active	High–middle
Electromagnetic	Active	Middle
Magnetic susceptibility	Active	Middle
Metal detectors	Active	Low
Seismic	Active	Low
Microgravity	Passive	Low
Induced polarization	Active	Low
Self-potential	Passive	Low
Thermal	Passive	Low

Table 1.1: Most frequently used geophysical techniques in archaeometry presenting the frequency of use and the characterization of each technique as active or passive (Table 1 from Gaffney 2007)

1.2 Marine Geophysics

Archaeological prospection of aquatic and marine sites comprises a distinct scientific field, where many adjustments must be made in order to overcome specific difficulties towards the completion of a successful survey in relation to explorations made on the land. During recent years, substantial efforts have been made towards the direction of modifying known instrumentation and proposing processing flowcharts to map the archaeological structures in marine sites of a sea depth of more than 10m. More specifically, Renkewitz et al. (2021) utilized a high-end laser scanner attached to an inspection class ROV to map a possible underwater archaeological site in Lake Arendsee in Germany in depths exceeding 20m. Georgiou et al. (2021) performed a multidisciplinary survey in the ancient Aegina Harbour complex using bathymetric analyzed with the “Canny” edge detection method and further verified via the use of acoustic data with the use of a photogrammetric ROV to successfully map an underwater archaeological complex. Pachero-Ruiz et al. in 2019 combined the aforementioned techniques with seismic data for deep sea cataloging of shipwrecks in the Black Sea. A total of 65 shipwrecks have been recorded, dating from the 4th century BC to the 19th AD in depths ranging between 40m and 2200m. Due to the high data



quality, as well as the range of the deep sea techniques, accurate 3D and 4D models of the shipwreck sites were reconstructed.

While the marine geophysics field present many advances during the last decade, the implementation of similar approaches in very shallow and coastal areas, that constitute a “gray zone” in marine archaeological surveys, is still a challenging tasks. Coastal areas show unique conditions compared to deep water and dryland areas, combining aspects of both environments. For that reason, neither the equipment for deep water surveys nor for dryland surveys can be used and has to be modified specifically for the coastal and ultra-shallow archaeological sites (Papadopoulos 2021).

The documentation of cultural heritage of shallow water areas becomes increasingly important in recent years for many reasons. First, constant coastal erosion combined with the rise of sea levels on a global scale render these areas endangered both in terms of accessibility and deformation. Overall, the lack of proper documentation and the associated protection measures will increase the risk of being utterly lost. Secondly, the tectonic history of certain areas may add extra danger to this effect. For example, in seismic active regions, the tectonic regime can influence the eustatic equilibrium of a landscape, leading to further degradation. Finally, human activities close to those sites also contribute to the faster deterioration of unseen areas important to archaeology and cultural heritage in general. Within the above context recent advances in shallow depth geophysical methods have shown the importance of these approaches in mapping cultural objects in these dynamic changing environments.

Schwardt et al. (2021) experimented with both synthetic and field seismic data, to assess the seismic method’s capability in detecting archaeological targets in very shallow waters of depths less than 5m. Two model-driven approaches were evaluated first on the synthetic dataset and then on the field collected data. The final results were more than satisfactory in both the synthetic and the real data set, proving that the seismic method, combined with the new “Prediction and Subtraction” is suitable for shallow water prospection.

Simyrdanis et al. (2016) conducted a geophysical survey of the littoral area of Ancient Olous in Elounda, Crete. The purpose of the survey was the mapping of some of the ultra-shallow regions surrounding the site. The static and dynamic variations of the underwater ERT method were used to complete the survey in the ultra-shallow part of the site. The results of the prospecting were the mapping of a marine area of more than 7.000 m², revealing the possible position of numerous buried antiquities below sea-level.



Papadopoulos et al. (2021) presented a multidisciplinary survey in the prehistoric site of Lambayanna, Peloponnese where the aforementioned static and dynamic ERT methods were combined with multisensor magnetic gradiometry, as well as the use of GPR to cover the littoral terrestrial areas surrounding the marine survey area. The survey covered an area larger than 4.4 hectares of both marine and coastal parts of the site and it revealed some promising targets of archaeological value which have yet to be excavated and thus verified.

1.3 Thesis Purpose

The present thesis will try to contribute to the newborn field of ultra-shallow marine and coastal archaeological geophysics showing the importance of such a scientific subdomain, especially in a country with numerous littoral archaeological sites such as Greece. This relatively new branch has not been extensively tested indicating two factors

- a) New techniques, methodologies and configurations are being introduced every day, for example the marine configuration used for the multisensory magnetic gradiometry survey presented in this thesis.
- b) Many survey factors, such as the correct configuration for each unique survey field, the time consumed during the data collection, the data quality and the processing stage afterwards are still problematic and require further polishing. Especially if the extra difficulties presented by the marine environment are taken into consideration.

The employment of geophysical prospection method in such challenging environments are driven by a series of research questions that have not found answers so far in the academic and scientific community, including the following: 1) How effective are these methods at locating and mapping archaeological material in the littoral shallow offshore zone? 2) What kind of structures are present both beneath the seabed and beneath water at the archaeological sites selected by this thesis? 3) What are the cultural dynamics of the archaeological sites? 4) What was the extent of the ancient structures (submerged or buried under the seafloor near the shore)?

Taking the above into consideration, the goals of this thesis are:

- 1) To showcase different geophysical techniques in marine prospection.

- 2) To assess the effectiveness of each method in each study area.
- 3) To pinpoint possible faulty or incomplete steps in all stages, from data collection to data processing, in order for them to be improved in the future.
- 4) To make a contribution to ultra-shallow marine geophysics, and in geophysics in general by accomplishing the above and by proposing ideas for future research.

1.4 Study Areas

For the purposes of this thesis, two different case studies in Greece were selected. The first study area selected is the site of Ancient Olous in Elounda, Crete and the second area is the sacred island of Delos. In Delos island, two different sites were surveyed, the first being Skhardanas bay and the second Stadium bay (**Figure 1.1**). In the sections below, some brief information about the historical and geological background of each site will be presented.

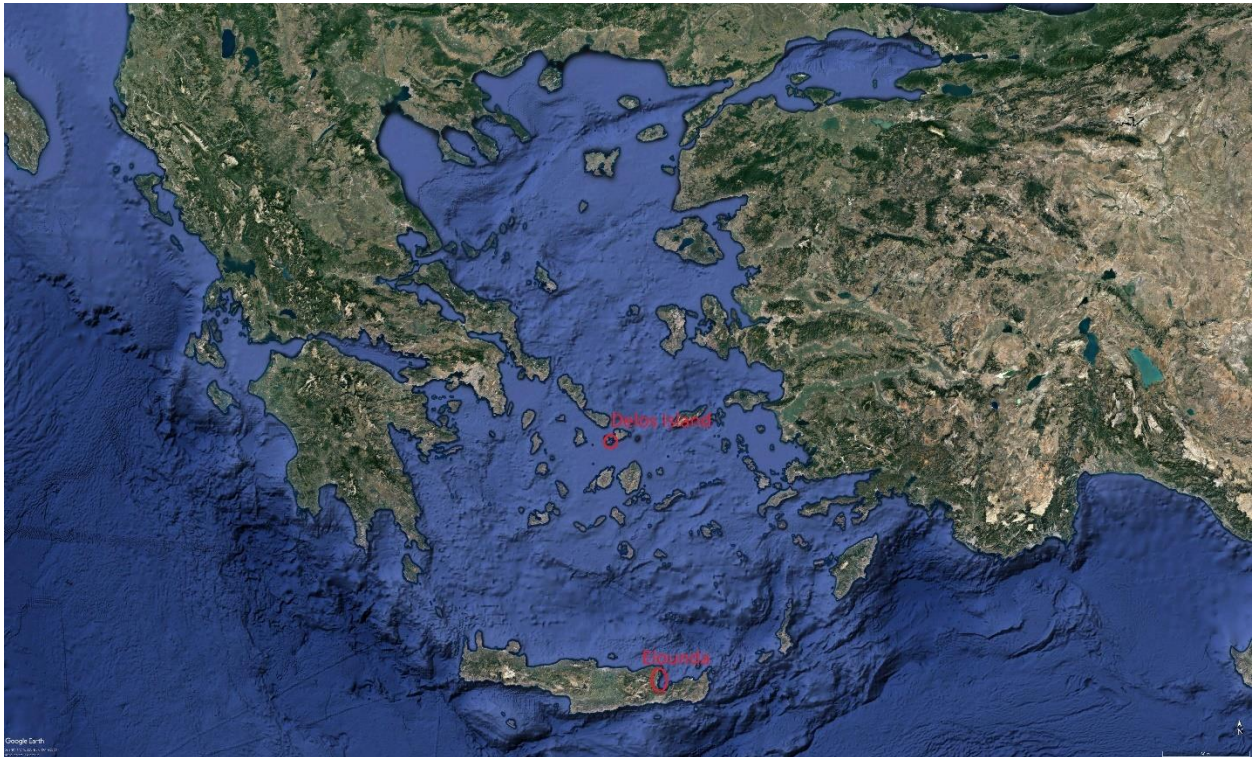


Figure 1.1: Satellite Picture of Greece from Google Earth with the survey areas marked



1.4.1 Ancient Olous

Elounda is located on the eastern coast of Lasithi, Crete near the county capital of Agios Nikolaos (**Figure 1.2**). Archaeological findings in ancient Olous attest to the fact that the area was inhabited at least since the Archaic period. Minoan tombs have been found in the broader area, while saved scriptures from the Hellenistic times reveal the existence of a great harbor centered city during that time. The city was expanding in the isthmus region that connects the Kolokytha peninsula with the Elounda Bay. A significant part of the city it is nowadays submerged underwater since the isthmus was narrowed from the sea levels variations. Several tombs and statues from the Roman Imperial period have been found, with the majority of the submerged visible constructions on the site believed to be from that time period. A great basilica with a mosaic pavement declares the presence of the Byzantines in the area as well. However, strong evidence indicate that the city was abandoned after the 6th century A.D, which was a common practice in all of the Aegean offshore settlements during the centuries of the Arabian raids. (Symirdanis et al. 2016; Theodoulou and Tourtas 2022)



Figure 1.2: Satellite Images of Crete (up) and Elounda (down) from Google Earth

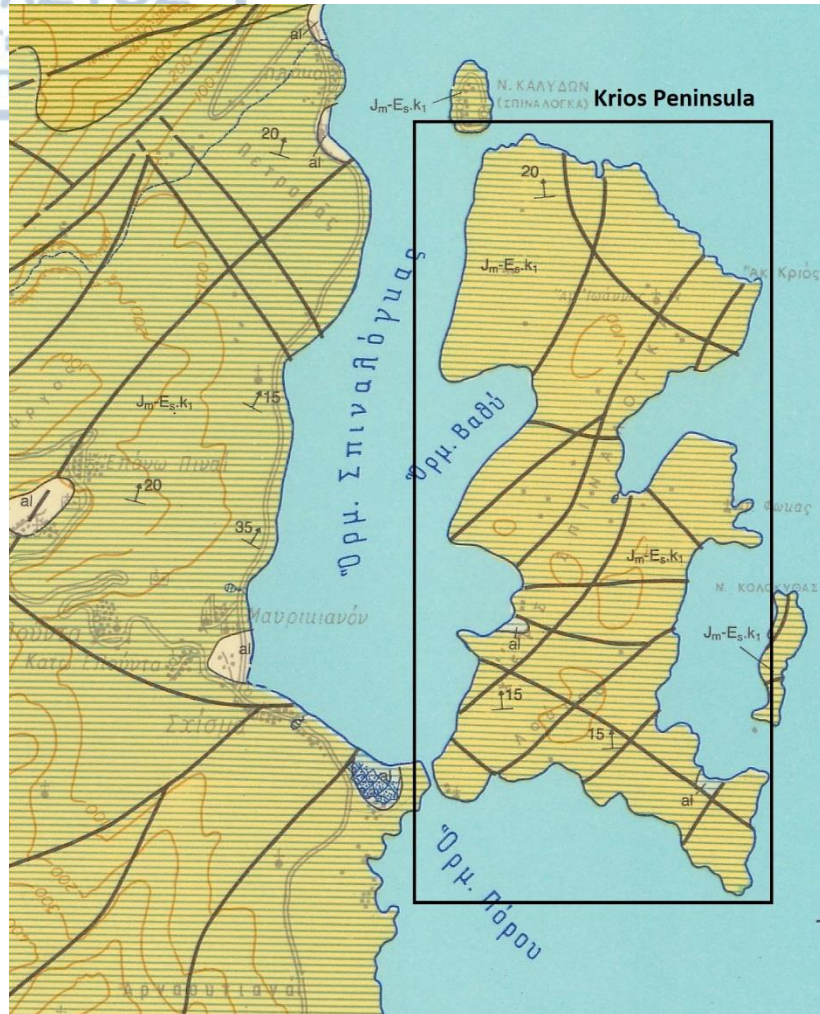
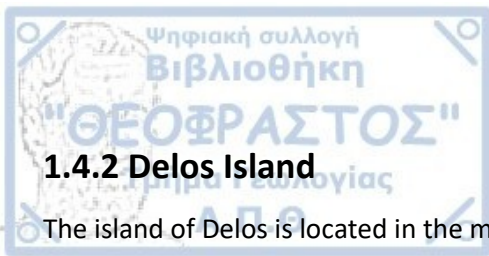


Figure 1.3: Geological Map of the broader Elounda area

Geologically, the broader area of Elounda is dominated by Plattenkalk (platy limestones) which are formations of crystalline limestones and locally marbles, medium to coarse crystalline, with thickness from a few cm to 1m. Some alluvial deposits can be seen in smaller areas consisting of loose sandy-clayey material, terra rosa with pebbles and unconsolidated material of sand and clay. The tectonic of the broader area shows a plethora of faults seen on the respective geological map of the area, with the majority of them being on Krios peninsula. It is possible that some of these faults extend underwater towards the investigation area (**Figure 1.3**).



1.4.2 Delos Island

The island of Delos is located in the middle of the Cyclades archipelago in the central part of the Aegean Sea. In fact, the archipelagos name comes from the Greek word “cyclos” which means circle, because all the other islands form a circle around Delos (**Figure 1.4**). The significance of Delos in political, economic and religious affairs of ancient Greece was undisputed. Though archaeological evidence of human traces attest to the fact that the island was populated even before the Mycenaean times (1400-1200 BC), it's religious importance as the sanctuary of the sun god Apollo has been documented from the early archaic times (700 BC).

The advantageous geographical position of Delos in the center of the Aegean made it perfect for commerce and as such, some great city states of Greece such as Naxos and Paros showed interest in investing in order to politically and culturally dominate over the island. Later during the archaic times the city of Athens started to affirm it's authority over the sanctuary, which eventually led to Athenian domination over the island. The Athenian occupation of Delos lasted for more than 100 years and ended in about 315 BC. During that time the Delians were expelled from Delos and a full purification of the island was conducted. This meant that the island became a full sanctuary of Apollo where it was illegal to give birth or to die.

During the early Hellenistic era, the successors of Alexander the Great gave the leadership of Delos back to the Delians, so the island enjoyed an independent period from 314-167 BC. A second Athenian occupation occurred then, with the Roman senate declaring the island as a duty free zone, which naturally made the commerce to flourish. It was during that time that Delos reached it's highest levels of prosperity, with the population of the island estimated between 10 and 20 thousand people. This is remarkable considering the extremely small size of the island.

The island's degradation started when Delos was completely ransacked twice, first by the army of Mithridatis Eupator, king of Pontus in 88 BC and then in 69 BC by Mithridati's allies, the pirates of Athenodorus. After these events the city of Delos was reduced to a mere village during the imperial era.

Finally, after the pagan era it was populated by a small Christian community and by the eight century it was completely abandoned. One of the reason why Delos is considered as one of the most important archaeological site in the world, is due to lack of inhabitants after the 8th century. The complete desertion of the island created a perfect scenario for archaeologists and scientists in general, since most of the ancient city and building are completely untampered.

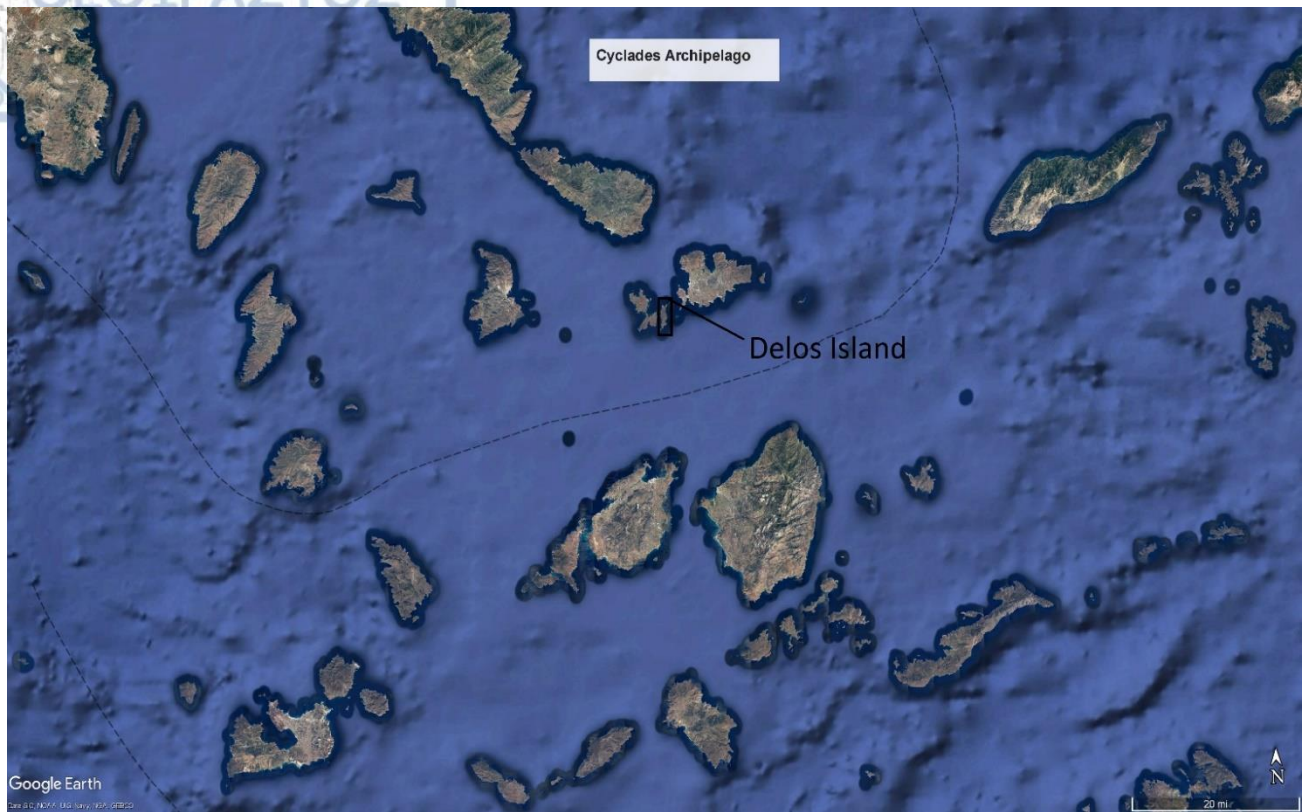


Figure 1.4: Satellite Pictures from Google Earth of Cyclades Archipelago (up) and Delos-Rinneia Islands with Delos marked (down)

The topography of Delos is rough and is characterized by rock outcrops. The surface at the northwestern part of the island consists of alluvial deposits of unconsolidated sediments, various sized gravels and silts. The main petrographic unit that occupies the island is medium-crystalline to coarse-crystalline granites and granodiorites. The mineral composition of granites-granodiorites includes quartz, alkaline, feldspars, plagioclases, biotite, or amphibole as main minerals and orthite, sphene as secondary minerals. According to the percentage of the main minerals, various local differentiations occur from granite granodiorite to amphibole granodiorite. A large number of faults run across all of Delos island, but two in particular are located near Skardhanas bay apparently extending to the underwater area of the bay where the survey took place. The first fault extends in S-N direction, while the second extends in NE-SW direction (**Figure 1.5**).

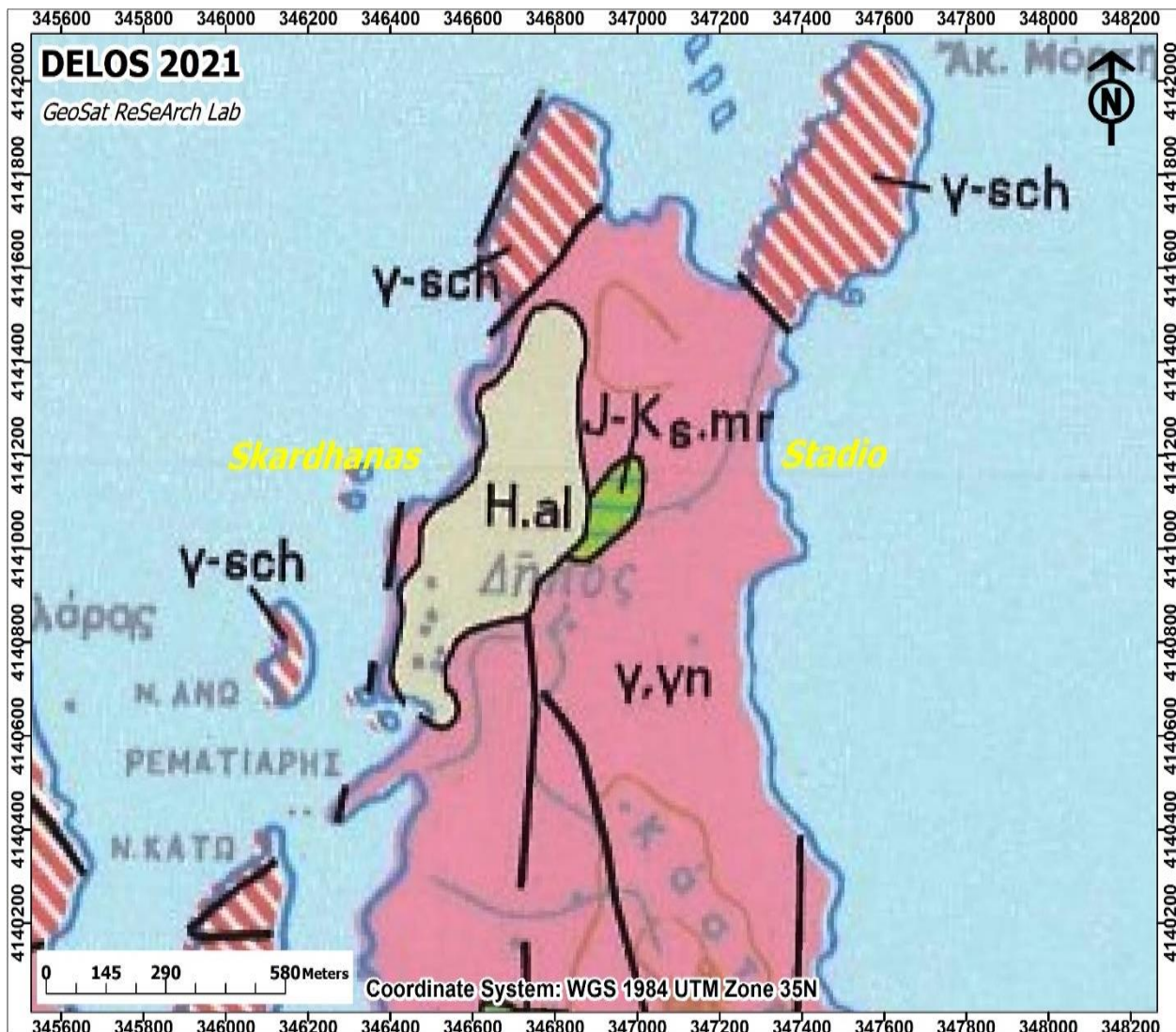


Figure 1.5: Geological Map of the Northern Delos Island with the investigation areas marked



Mourtzas (2011) presented a study concerning the rise of the sea level in Delos Island since the Hellenistic era. All the available indicators of sea level change were taken into account, such as the positioning of sea rock formations, and the location of the visible submerged ancient structures. The study revealed that the sea level around Delos has risen by about 2.15 m. This corresponds to a coastal zone of width greater than 30m. This revelation further outlines the need of marine geophysics in order for that vast sunken cultural heritage to be able to be documented and perhaps saved.

Chapter 2– Methodology

2.1 Introduction

In this chapter, both the Electrical Resistivity Tomography (ERT) and the multisensor magnetic gradiometry geophysical prospecting methods used in this thesis will be presented. Firstly, some basic theoretical background will be given for each method. Furthermore, the instrumentation used in the surveys as well as the data collection chain will be explained. Finally, the data processing flowchart and the respective softwares used will be mentioned.

2.2 Electrical Resistivity Tomography

2.2.1 Basic Principles

The Electrical Resistivity Tomography method is an active geophysical method with the aim to map the subsurface resistivity by measuring the potential differences caused by the injection and flow of direct current into the earth. In this method, four electrodes are constantly utilized. Two current electrodes used to inject electricity in the substratum, the potential is measured in two other potential electrodes (*Figure 2.1*).

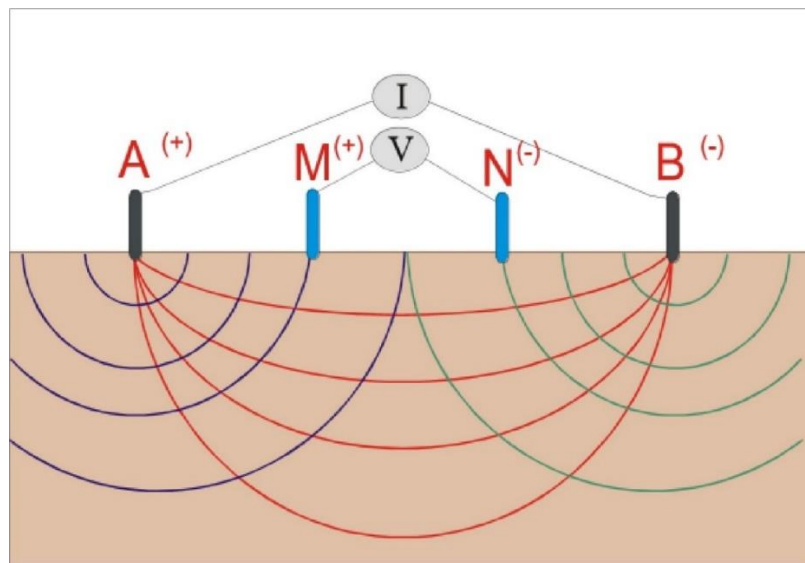
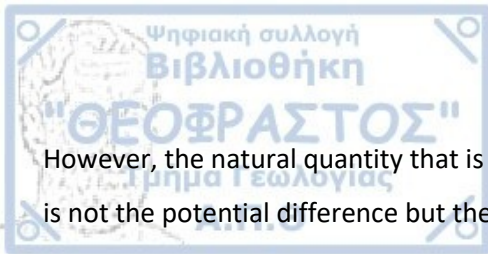


Figure 2.1: Basic Measuring Principle of Electric Method using an array of four electrodes. A, B current electrodes and M, N potential electrodes.



However, the natural quantity that is frequently used for the characterization of the underground layers is not the potential difference but the **resistivity**:

$$\rho = \frac{R \cdot S}{l} \quad (1)$$

R is defined as the electrical resistance of a cylindrical conductor

S is the cross section of the cylindrical conductor

l is the length of the cylindrical conductor

The SI measuring unit for resistivity is $1 \Omega m$ and the reverse of resistivity $\sigma = 1/\rho$ is called conductivity.

All geological formations are comprised of a combination of rocks and minerals with varying resistive and conductive properties. The driving factor that actually affects the resistivity of a specific formation is the water that flows within the pores of the rocks (Papazachos V. 1996). Consequently, the porosity of the rocks has to be taken into consideration in order to define its conductivity and as a result its resistivity. Archie in 1942 proposed the following empirical equation which takes into account the rock's porosity and is known as **Archie's Law**:

$$\rho = \alpha * \rho_v * \phi^{-m} \quad (2)$$

a, m are constants which usually take the values $a=1$ and $m=2$

ρ_v is the resistivity of the water inside the pores of the rocks

ϕ is the rock's porosity

Since the interior of the earth is not homogenous, meaning that the resistivity is changing laterally and vertically, its actual (real) value cannot be directly measured or calculated. For that reason the term **apparent resistivity** ρ_α is defined that shows the resistivity value the earth would have if it was divided into homogenous blocks. The value of ρ_α depends on the relative position and the distance between the current and potential electrodes used to complete the resistivity measurements:

$$\rho_{\alpha} = \frac{2\pi V}{i} * \frac{1}{\frac{1}{AM} + \frac{1}{BM} + \frac{1}{AN} + \frac{1}{BN}} = \frac{2\pi V}{i} * K \quad (3)$$

A, B, M, N are the positions of the two current electrodes and the two potential electrodes respectively

V is the measured potential difference between the two potential electrodes

i is the intensity of the electrical current that is being injected into the earth

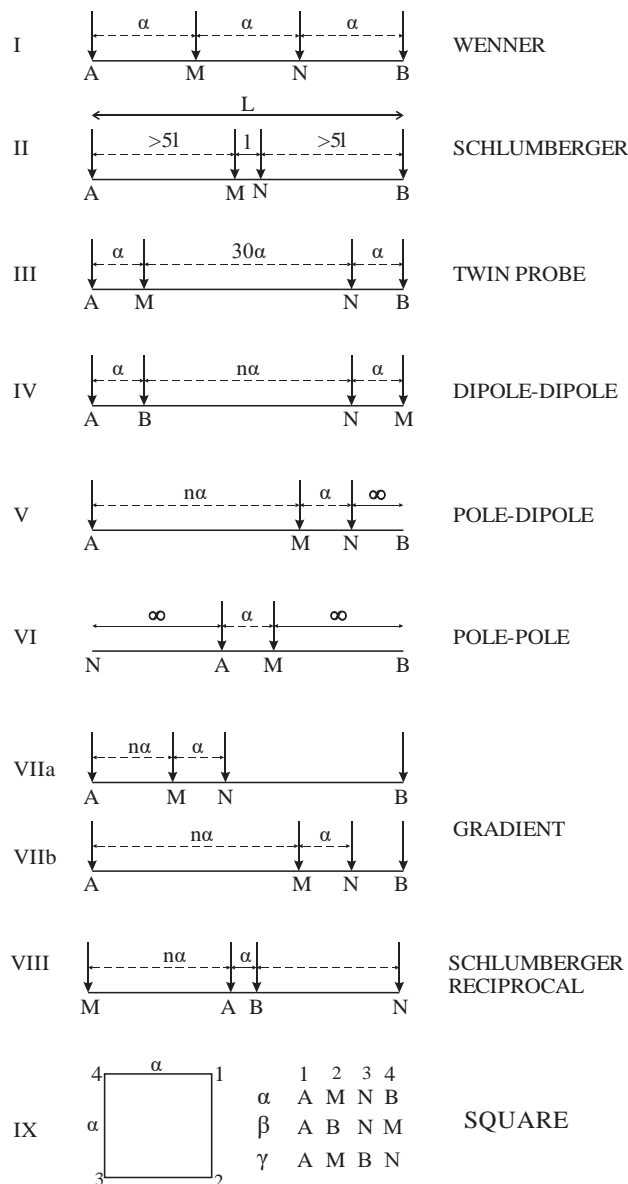


Figure 2.2: Illustration of the most common electrode arrays

The quantity K is called the geometrical factor and its value depends on the positions of the current and potential electrodes. It is considered a key factor in the Electrical Resistivity method because even slight alterations to the geometric factor can drastically change the apparent resistivity values recorded in a survey as well as the resolution and the depth of investigation. Thus, many different electrode arrays have been proposed over the years that exhibit different resolving capabilities depending on the subsurface electrical resistivity structure (Σφάλμα! Το αρχείο προέλευσης της αναφοράς δεν βρέθηκε.).

In this chapter only the two arrays that were used for the surveys will be briefly described.

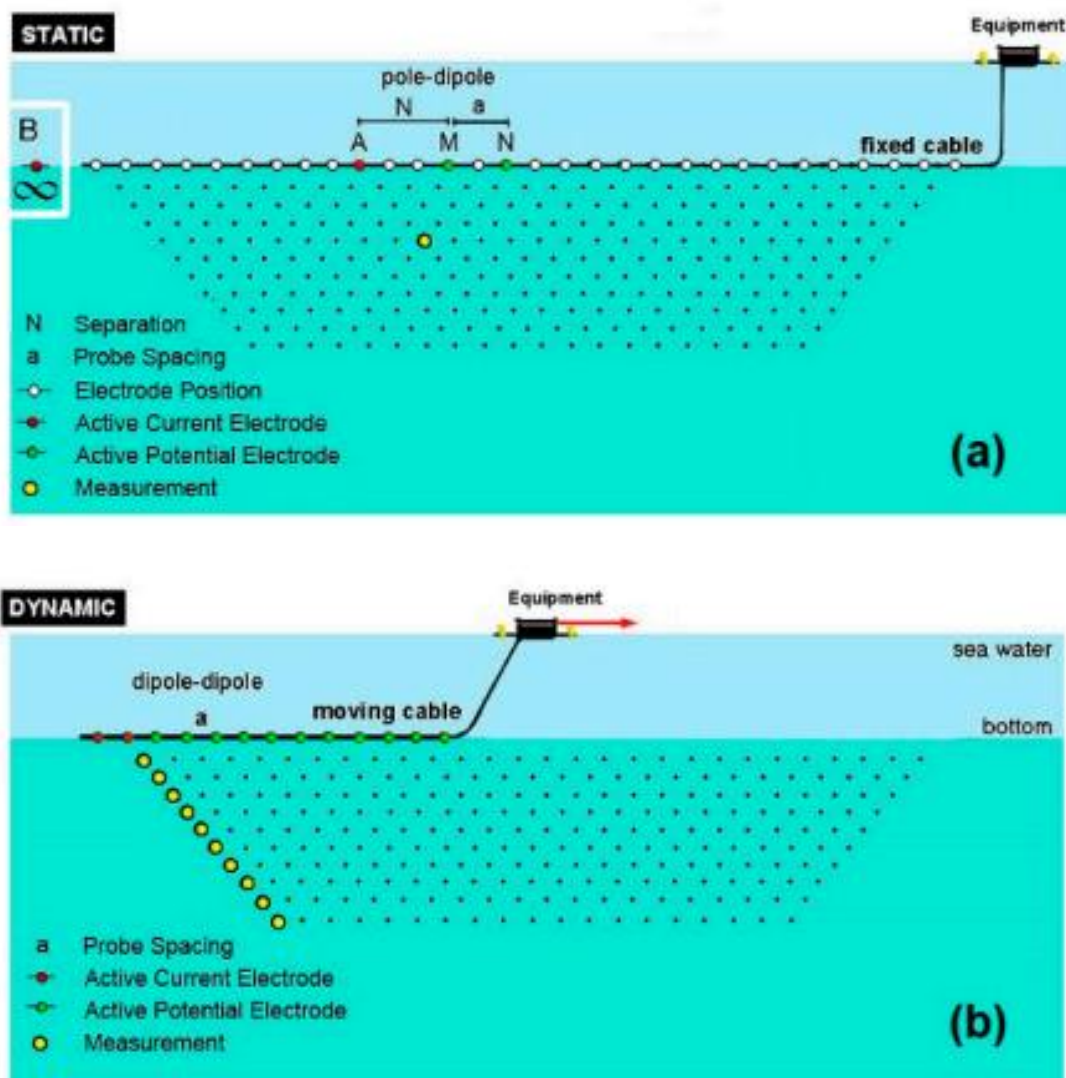


Figure 2.3: Pole-Dipole and Dipole-Dipole arrays as used in the static and dynamic ERT methods (adopted from figure 4 Simyrdanis et al. 2016)

Dipole-Dipole Array: In this array the distance between the electrodes is: $AB=MN=2l$, $BM=n*2l$. For $n \gg 1$ $\rho_{\alpha} = 2\pi n(n+1)(n+2)l \frac{\Delta V}{I}$. During the survey the positions of the A, B, M, N electrodes constantly change while the distance between them remains the same. This array was used for the dynamic marine ERT surveys (**Figure 2.3(b)**).

Pole-Dipole Array: In this array, the distance between the electrodes is: $AB > 15nl$, $MN=l$, $BM=nl$ and $\rho_{\alpha} = 2\pi n(n+1)l \frac{\Delta V}{I}$. The same principle as the dipole-dipole array applies here too, constantly moving the electrode positions during the array but keeping the distance between them stable. This array was used for the static marine ERT survey (**Figure 2.3(a)**).

2.2.2 Data Collection

2.2.2.1 Bathymetry

One of the main reasons that marine geophysics present a greater level of difficulty compared to their dryland counterparts is the fact that all the data collected on the field must be superimposed correctly to the sea bottoms complex topography in order for them to be accurate. For that reason, a bathymetric survey must be undertaken first. The bathymetric measurements in both study areas were conducted by combining two different mapping methods depending on the thickness of the sea water.

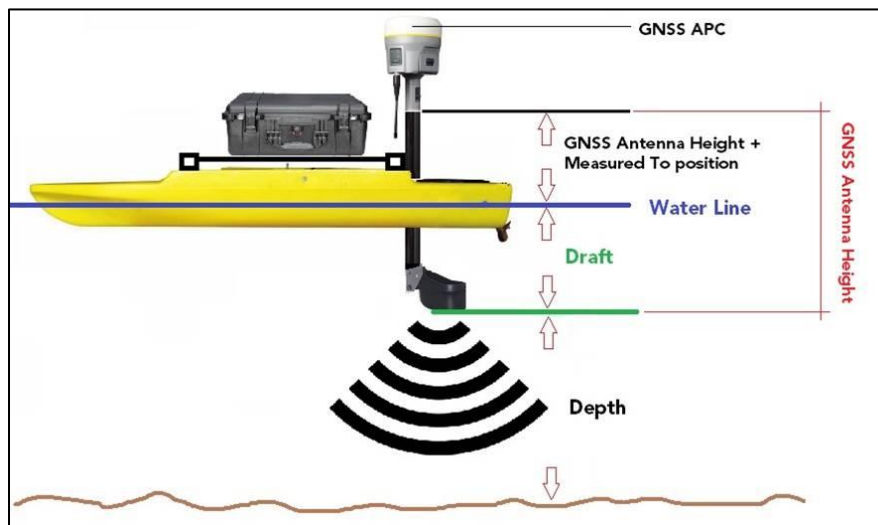
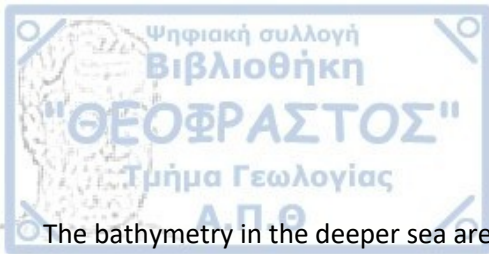


Figure 2.4: Standard configuration of the echo sounder combined with the GNSS antenna and the logger



The bathymetry in the deeper sea areas was completed with the help of a motor driven boat carrying the appropriate instrumentation. More specifically, a SonarMite BTX sonar unit was mounted to the boat and combined with a Javad Triumph-1 GPS unit, thus making possible to associate every bathymetric point measured with the Real Time Kinematic (RTK) Global Navigation Satellite System (GNSS) coordinates (**Figure 2.4**).

On the other hand, it was impossible to utilize the boat to approach the shallower parts of the study areas which in some cases was rough and extremely rocky. So a different field approach was followed to complete the bathymetric measurements in these parts. Two separate Javad Triumph-1 units were utilized, one configured as base station and positioned near the investigation area (**Figure 2.5**), and the second one as rover (**Figure 2.6**). The absolute coordinates of the base point were stored in a specific projection (eg UTM Zone 34N) through the Hellenic POsitioning System (HEPOS). HEPOS consists of 98 permanent reference stations and a Control Center that collects and processes all streaming data from the reference stations, thus providing “real time” sub-centimeter positioning accuracy of the coordinates’ points for RTK techniques. The rover GNSS unit was constantly communicating with the base station through internal UHF protocol. The rover unit was mounted on a pole, which was then used to manually acquire a large number of bathymetric measurements in the shallower parts of the study areas, with a mean positioning and elevation accuracy of 1,4 cm .



Figure 2.5: Base GNSS Unit which is constantly communicating with a rover unit.



Figure 2.6: GNSS unit mounted on a pole and used as a rover for the shallow bathymetric survey

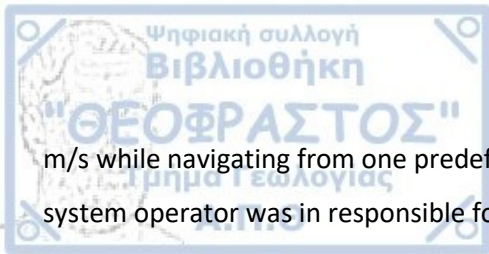
2.2.2.2 Dynamic ERT

The dynamic survey mode employs a constantly moving array along a predefined line. In the submerged mode the cable is underwater and attached on the seabed. The survey configuration is comprised of an inflatable boat with length of 3m, equipped with a 10hp 4-stroke outboard motor, a special marine cable with 13 graphite electrodes, the 10-channel Syscal Pro Switch resistivity tomography system generating a 2.5 Amp and an external toughpad to store and check in situ the data quality (**Figure 2.7**). Finally, a RTK GNSS array of two Javad Triumph-1 GPS was used, one configured as a base located near the research area and the other as a rover mounted to the boat, which works in the same exact way as described in the bathymetry section above.



Figure 2.7: The Syscal Pro Switch resistivity tomography system along with an external battery and a toughpad

The dipole-dipole electrode configuration was chosen for the submerged dynamic surveys. The lines were predefined and the motor driven boat was pulling the cable along them while carrying the instrumentation and two operators. The navigator had to drive the boat at a steady speed of about 1.5



m/s while navigating from one predefined GPS point to the next along a specific line and the resistivity system operator was in responsible for the proper operation of the whole instrumentation.

A total of thirty seven dynamic (37) lines were surveyed in Skardhanas bay. The five lines that were surveyed at the shallowest parts of the bay, were characterized as ultra shallow lines since they were surveyed with the boat being pushed manually along the shore (**Figure 2.88**). On the other hand the southern bay in Ancient Olous was surveyed with twenty seven (27) dynamic lines.



Figure 2.8: In situ ERT survey with dynamic lines to cover the ultra shallow part of the site in Skardhanas.

2.2.2.3 Static ERT

The static survey mode was utilized to investigate totally sixty two (62) lines forming two predefined grids across the northern part of Olous bay. The grids was accurately marked with the help of a RTK GNSS unit. The array configuration was comprised of the 10-channel Syscal Pro Switch resistivity tomography system identical to the one used for the dynamic survey and a marine cable equipped with 48 stainless steel electrodes with 1m spacing between them. The cable was used to collect the data along parallel lines in the grids with the pole-dipole array configuration with an interline spacing was 1m (**Figure 2.9**). The submerged grids was situated near the shore, so the instrumentation was always safely kept on shore.



Figure 2.9: View of the submerged cable with the stainless-steel electrodes attached on the sea bottom to complete the Static ERT Survey

2.3 Multisensor Magnetic Gradiometry

2.3.1 Basic Principles

Magnetic measurements deal with anomalies of the geomagnetic field, which are caused by contrasts of the rock magnetization \vec{J} or by soils rich in magnetic oxides. The magnetization of rocks contains shares of inductive and remnant magnetization. The inductive magnetization originates from the magnetic earth field and depends on its actual strength and direction \vec{H} and on the susceptibility κ of rocks or soils following the equation:

$$\vec{J} = \kappa * \vec{H}. \quad (4)$$

In contrast, the remnant magnetization is constant and is not changed by alterations of the recent magnetic field. The remnant magnetization is a long-term effect, which is independent of the recent geomagnetic field (**Figure 2.110**). Only iron and ferrimagnetic minerals can be strongly magnetized. The latter are mostly oxides and sulphides of iron. Other materials may be ferro-, para- and dia- magnetic. While the similarly strong ferromagnetism is combined with high magnetic susceptibility, the para- and dia- magnetism are so weak that they can be ignored in field measurements.

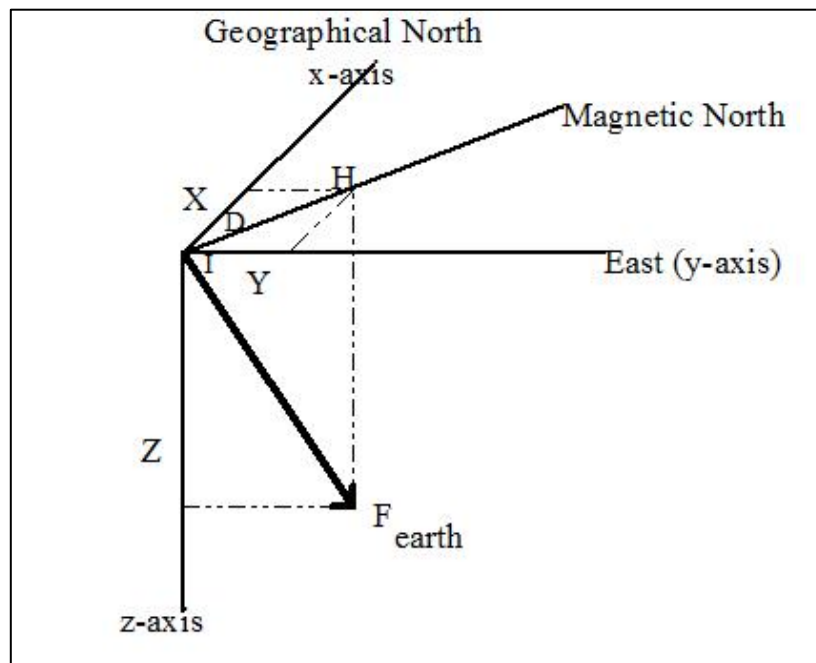


Figure 2.1: Components of the Earth's magnetic field

The magnetic effects of the respective bodies, which can be surveyed on the surface of the earth depend on their magnetization, form and size and their burial depth, since the magnetic field weakens



with increasing distance. In archaeological investigations various constructions such as kilns, ovens or fireplaces show increased remnant magnetism thus producing pronounced magnetic signatures. The task of the interpretation is to separate the results of human activity from the geological variations in subsurface materials.

The measurement of the magnetic field is carried out by proton or caesium magnetometers, which measure the total magnetic field strength, or by gradiometers (proton, caesium or fluxgate), which measure the vertical or the horizontal gradient of the total magnetic field or one of its components, correspondingly. The measurements of the first derivative of the vertical component (vertical magnetic gradient) are measured with a fluxgate gradiometers that have accuracy of the order of magnitude of 0.1 - 1nT/m. The magnetic field is measured at a constant distance and close to the surface of the ground. Measurements are usually taken at constant step intervals (usually 0.5-1m depending on the size of the archaeological targets) within rectangular grids of relatively small dimensions (such as 10x10m or 20x20m). Similar is the case of proton or caesium gradiometers, which measure the vertical or horizontal gradient of the total magnetic field intensity.

Subsurface targets with magnetic properties different from those of the surrounding soil matrix change the local magnetic field at some large or small degree. This kind of perturbation of the magnetic field is observed as an "anomaly" in the measurements. The disturbance of the upper layers of the soil due to anthropogenic causes can create observable magnetic anomalies.

The magnetic anomalies are directly related to the measurement of the magnetic susceptibility of the soil. Areas with enhanced magnetic susceptibility (with respect to the one of the surrounding soil) are represented as positive anomalies, whereas areas with smaller percentage content in iron oxides (i.e. smaller values of the magnetic susceptibility) are represented as negative magnetic anomalies. Both kinds of anomalies are interesting in the process of interpretation of the magnetic data. Generally, the existence of archaeological relics in the subsoil is characterized by an increase in the magnetic susceptibility levels of the corresponding area, causing a weak magnetic field, which alters the local magnetic field of the earth.

2.3.2 Data Collection

Sensorik & Systemtechnologie (SENSYS) MX Compact Survey System was used for the geomagnetic data collection at Stadio Bay in Delos. SENSYS MX is a multi-channel measurement system, equipped with five FGM600 magnetometers. The system is dependent on valid GPS information with the NMEA 0183 standard. Five magnetometers are mounted on a non-magnetic cart with 50 cm separation. While the distance between sensors are fixed along the array (X-axis), measurements along the track (Y-axis) depend on the speed of survey as the sensors read magnetic data in fixed time intervals; a faster movement of array results in fewer readings and vice versa. The whole system was mounted on a specific frame made of fiberglass for carrying the sensors, the GPS and the electronic box during the offshore geomagnetic survey.

Data acquisition is provided by the MonMX 4.0 software which communicates with the MXcompact box of the multi-channel system. The software interface is used for configuring channels and sensor compensation prior to a survey. It also enables the surveyor to navigate in the landscape and helps in creating an even coverage of the survey area



Figure 2.2: Sensorik & Systemtechnologie (SENSYS) MX Compact Survey System mounted on a plastic frame during the survey in the very shallow part of an archaeological site.



A total area of 1,443 square meters was scanned with the SENSYS array in Delos. Due to the difficulties presented by the rocky terrain, the survey area was split into two sections. The magnetic prospecting was limited to an area of sea depth up to 1.5m. Even though all the magnetometers, the cables, and the electronic box are completely waterproof, the GPS attached to the frame is not, so the investigation had to be narrowed down up to that depth to prevent the risk of sea water damaging it. The magnetic array was operated by a team of three surveyors that navigated the frame across the rocky shore along parallel lines in a S-N direction. At the same time, a fourth surveyor stayed inside an inflatable boat where the sensitive equipment (the external battery and the toughpad) was safely kept inside a wooden box. This particular magnetic survey configuration was used for the first time in the very shallow parts of Stadio Bay in Delos Island (**Figure 2.2**).

Chapter 3– Data Processing and Results

All the data collected from the aforementioned geophysical methods had to undergo a processing stage which transforms them from the original raw data to a form that can be interpreted. In this chapter all the steps followed in the data processing will be presented along with the final results.

3.1 ERT Data Processing

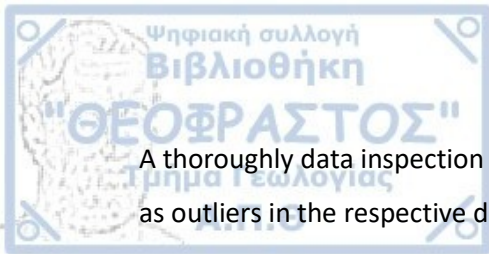
The same processing flowchart has been followed for all three ERT data sets (Delos Dynamic, Elounda Dynamic, Elounda Static) with some slight differentiations depending on the special conditions each survey presented (data quality, terrain difficulties etc.).

1) Extermination of Bad Data Points

For every ERT line surveyed, a binary file is created. This file contains all the geographical and geophysical information collected including the measured potential differences in every point, the injected current intensity, the apparent resistivity distribution for each channel and the exact coordinates of every data point. This information can be inspected and processed through the Prosys II software (**Σφάλμα! Το αρχείο προέλευσης της αναφοράς δεν βρέθηκε.**).

#	El-stay	Filo	Dev	Vr	In	Latitude	Longitude	Name	Oveibo	Tr-Bat	Pot-Bat	Temp	Date	Gsp/Bat	Synchron	Cole Tau	Cole M	Cole A
1	Δρόση Δρόση	0.37	0.00	-8.926	2480.302	3724.250488	2515.574609	1	0	0.00	0.00	0.0	9/17/2021 11:50:46.	0	0	0.0	0.0	0.00
2	Δρόση Δρόση	0.52	0.00	-17.169	2480.302	3724.250488	2515.574609	2	0	0.00	0.00	0.0	9/17/2021 11:50:46.	0	0	0.0	0.0	0.00
3	Δρόση Δρόση	0.65	0.00	-8.926	2480.302	3724.250488	2515.574609	3	0	0.00	0.00	0.0	9/17/2021 11:50:46.	0	0	0.0	0.0	0.00
4	Δρόση Δρόση	0.97	0.00	-6.349	2480.302	3724.250488	2515.574609	4	0	0.00	0.00	0.0	9/17/2021 11:50:46.	0	0	0.0	0.0	0.00
5	Δρόση Δρόση	1.03	0.00	-3.070	2480.302	3724.250488	2515.574609	5	0	0.00	0.00	0.0	9/17/2021 11:50:46.	0	0	0.0	0.0	0.00
6	Δρόση Δρόση	1.20	0.00	-2.900	2480.302	3724.250488	2515.574609	6	0	0.00	0.00	0.0	9/17/2021 11:50:46.	0	0	0.0	0.0	0.00
7	Δρόση Δρόση	1.52	0.00	-2.379	2480.302	3724.250488	2515.574609	7	0	0.00	0.00	0.0	9/17/2021 11:50:46.	0	0	0.0	0.0	0.00
8	Δρόση Δρόση	1.44	0.00	-1.576	2480.302	3724.250488	2515.574609	8	0	0.00	0.00	0.0	9/17/2021 11:50:46.	0	0	0.0	0.0	0.00
9	Δρόση Δρόση	1.42	0.00	-1.132	2480.302	3724.250488	2515.574609	9	0	0.00	0.00	0.0	9/17/2021 11:50:46.	0	0	0.0	0.0	0.00
10	Δρόση Δρόση	7.69	0.00	4.599	2480.302	3724.250488	2515.574609	10	0	0.00	0.00	0.0	9/17/2021 11:50:46.	0	0	0.0	0.0	0.00
11	Δρόση Δρόση	0.34	0.00	44.759	2469.954	3724.250732	2515.575342	1	0	0.00	0.00	0.0	9/17/2021 11:50:48.	0	0	0.0	0.0	0.00
12	Δρόση Δρόση	0.95	0.00	-18.015	2469.954	3724.250732	2515.575342	2	0	0.00	0.00	0.0	9/17/2021 11:50:48.	0	0	0.0	0.0	0.00
13	Δρόση Δρόση	0.75	0.00	9.944	2469.954	3724.250732	2515.575342	3	0	0.00	0.00	0.0	9/17/2021 11:50:48.	0	0	0.0	0.0	0.00
14	Δρόση Δρόση	1.03	0.00	-6.779	2469.954	3724.250732	2515.575342	4	0	0.00	0.00	0.0	9/17/2021 11:50:48.	0	0	0.0	0.0	0.00
15	Δρόση Δρόση	1.15	0.00	-4.315	2469.954	3724.250732	2515.575342	5	0	0.00	0.00	0.0	9/17/2021 11:50:48.	0	0	0.0	0.0	0.00
16	Δρόση Δρόση	1.43	0.00	-3.353	2469.954	3724.250732	2515.575342	6	0	0.00	0.00	0.0	9/17/2021 11:50:48.	0	0	0.0	0.0	0.00
17	Δρόση Δρόση	1.66	0.00	-2.994	2469.954	3724.250732	2515.575342	7	0	0.00	0.00	0.0	9/17/2021 11:50:48.	0	0	0.0	0.0	0.00
18	Δρόση Δρόση	1.71	0.00	-1.863	2469.954	3724.250732	2515.575342	8	0	0.00	0.00	0.0	9/17/2021 11:50:48.	0	0	0.0	0.0	0.00
19	Δρόση Δρόση	1.70	0.00	-1.347	2469.954	3724.250732	2515.575342	9	0	0.00	0.00	0.0	9/17/2021 11:50:48.	0	0	0.0	0.0	0.00
20	Δρόση Δρόση	8.49	0.00	5.197	2469.954	3724.250732	2515.575342	10	0	0.00	0.00	0.0	9/17/2021 11:50:48.	0	0	0.0	0.0	0.00
21	Δρόση Δρόση	0.34	0.00	44.915	2467.721	3724.250977	2515.576563	1	0	0.00	0.00	0.0	9/17/2021 11:50:50.	0	0	0.0	0.0	0.00
22	Δρόση Δρόση	0.57	0.00	-18.680	2467.721	3724.250977	2515.576563	2	0	0.00	0.00	0.0	9/17/2021 11:50:50.	0	0	0.0	0.0	0.00
23	Δρόση Δρόση	0.76	0.00	-10.073	2467.721	3724.250977	2515.576563	3	0	0.00	0.00	0.0	9/17/2021 11:50:50.	0	0	0.0	0.0	0.00
24	Δρόση Δρόση	1.09	0.00	-7.224	2467.721	3724.250977	2515.576563	4	0	0.00	0.00	0.0	9/17/2021 11:50:50.	0	0	0.0	0.0	0.00
25	Δρόση Δρόση	1.21	0.00	-4.973	2467.721	3724.250977	2515.576563	5	0	0.00	0.00	0.0	9/17/2021 11:50:50.	0	0	0.0	0.0	0.00
26	Δρόση Δρόση	1.47	0.00	-3.453	2467.721	3724.250977	2515.576563	6	0	0.00	0.00	0.0	9/17/2021 11:50:50.	0	0	0.0	0.0	0.00
27	Δρόση Δρόση	1.74	0.00	-2.737	2467.721	3724.250977	2515.576563	7	0	0.00	0.00	0.0	9/17/2021 11:50:50.	0	0	0.0	0.0	0.00
28	Δρόση Δρόση	1.81	0.00	-1.592	2467.721	3724.250977	2515.576563	8	0	0.00	0.00	0.0	9/17/2021 11:50:50.	0	0	0.0	0.0	0.00
29	Δρόση Δρόση	1.90	0.00	-1.919	2467.721	3724.250977	2515.576563	9	0	0.00	0.00	0.0	9/17/2021 11:50:50.	0	0	0.0	0.0	0.00
30	Δρόση Δρόση	8.96	0.00	-5.373	2467.721	3724.250977	2515.576563	10	0	0.00	0.00	0.0	9/17/2021 11:50:50.	0	0	0.0	0.0	0.00
31	Δρόση Δρόση	0.36	0.00	47.951	2491.407	3724.251221	2515.577295	1	0	0.00	0.00	0.0	9/17/2021 11:50:52.	0	0	0.0	0.0	0.00
32	Δρόση Δρόση	0.60	0.00	-18.935	2491.407	3724.251221	2515.577295	2	0	0.00	0.00	0.0	9/17/2021 11:50:52.	0	0	0.0	0.0	0.00
33	Δρόση Δρόση	0.85	0.00	-11.200	2491.407	3724.251221	2515.577295	3	0	0.00	0.00	0.0	9/17/2021 11:50:52.	0	0	0.0	0.0	0.00
34	Δρόση Δρόση	1.19	0.00	-7.854	2491.407	3724.251221	2515.577295	4	0	0.00	0.00	0.0	9/17/2021 11:50:52.	0	0	0.0	0.0	0.00
35	Δρόση Δρόση	1.28	0.00	-4.931	2491.407	3724.251221	2515.577295	5	0	0.00	0.00	0.0	9/17/2021 11:50:52.	0	0	0.0	0.0	0.00
36	Δρόση Δρόση	1.65	0.00	-3.897	2491.407	3724.251221	2515.577295	6	0	0.00	0.00	0.0	9/17/2021 11:50:52.	0	0	0.0	0.0	0.00
37	Δρόση Δρόση	1.91	0.00	-3.010	2491.407	3724.251221	2515.577295	7	0	0.00	0.00	0.0	9/17/2021 11:50:52.	0	0	0.0	0.0	0.00
38	Δρόση Δρόση	2.04	0.00	-2.250	2491.407	3724.251221	2515.577295	8	0	0.00	0.00	0.0	9/17/2021 11:50:52.	0	0	0.0	0.0	0.00
39	Δρόση Δρόση	2.13	0.00	-1.705	2491.407	3724.251221	2515.577295	9	0	0.00	0.00	0.0	9/17/2021 11:50:52.	0	0	0.0	0.0	0.00
40	Δρόση Δρόση	9.06	0.00	-5.444	2491.407	3724.251221	2515.577295	10	0	0.00	0.00	0.0	9/17/2021 11:50:52.	0	0	0.0	0.0	0.00

Figure 3.1: Binary file of Dynamic Line 003



A thoroughly data inspection showed the appearance of extreme resistivity values that appear as outliers in the respective data sets.. These points that clearly diverge greatly from the main volume of measurements must be cleared out in order to minimize their effect and the final error in the results. This was originally based on filtering the data by keeping the measurements that lied within specific limits based on the distribution of the current intensity, the potential, the apparent resistivity and the measurement's deviation.

Concerning the Skhardanas data set, the in situ survey faced a problem related to the rough topography of the seabed which caused delays in the data collection and deteriorated the quality of the measurements. More specifically, the seabed was covered with sharp and uneven in height rocks that caused two problems: a) the inability to approach the ultra-shallow parts of the bay with the boat which resulted to complete the survey manually, b) the submerged cable was getting stuck between the large boulders interrupting the smooth data collection. This caused significant delays as the specific lines had to be resurveyed since the boat was twisting and losing its direction. As a result, some of the lines ended up with length significantly shorter than originally planned. Moreover, after an in situ analysis of the data, it was proven that the cable was damaged due to the force applied to it from the boat due to these obstacles. This explains why after a certain point, only five of the ten channels of the instrument was recording the apparent resistivity values correctly and as such, only 30 of the 37 lines were further processed.

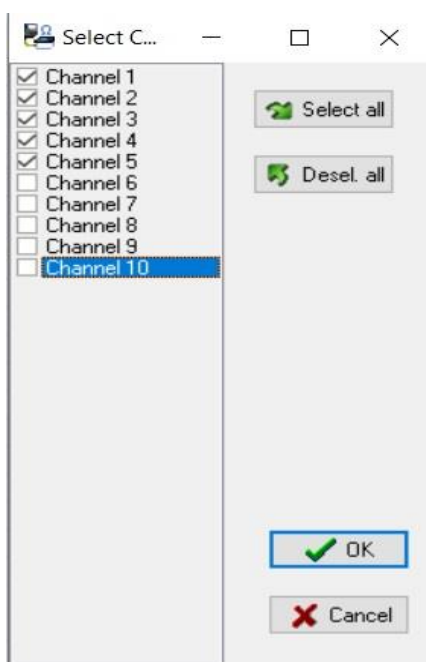
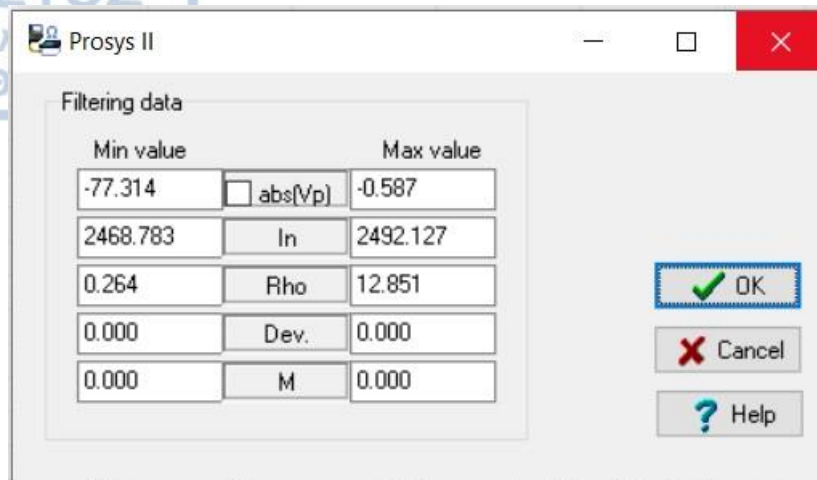


Figure 3.2: Data Filtering of a specific dynamic line (Line 003) (up) and removal of channels 5 to 10 related to deeper N separations for the dipole-dipole array data in Skardhanas due to poor data quality caused by the malfunction of the submerged cable (down)

After a careful inspection of each line, it was concluded that despite the fact that measured potential difference and the injected current seemed valid, the computed apparent resistivity in channels 6-10 was either too high or too low. As such, during the pre-processing stage inside Prosys II software, only the measurements with apparent resistivity ranging from 0.1 to 1 Ohm were taken into account. In addition, channels 6-10 were excluded, leaving only channels 1-5 for further processing (**Figure 3.2**). Obviously, this was a consequence of the severe damage of the cable during the data collection due to the rocky seabed of Skardhanas bay (**Figure 3.3**).

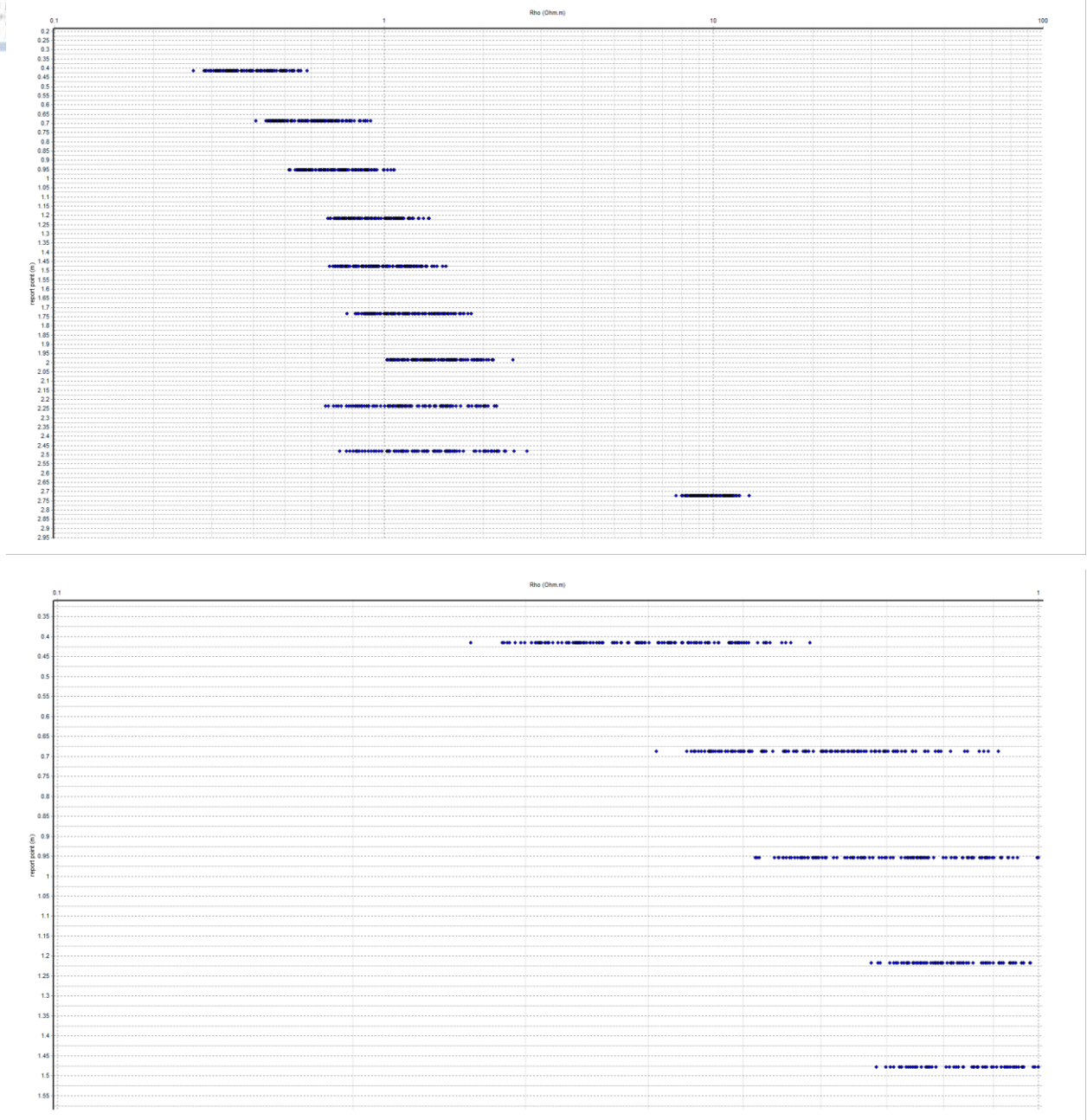


Figure 3.3: Distribution of apparent resistivity distribution of Line 003 before (up) and after (down) the bad data point extermination

2) Combination of ERT with the correct bathymetric data and sea water conductivity



The next step of the processing requires merging the electric data with the bathymetry of the associated survey site. This is extremely important because if the bathymetry is disregarded or for some reason an incorrect bathymetry is used, the error of the produced model will increase and the final results may be altered, resulting in an interpretation not responding to reality.

Fox et al. in 1980 presented a paper studying the effects of topography in both apparent resistivity and induced polarization data. The study observed that different topographic terrains presented different anomalies, for example a specific anomaly is produced from a ridge, from a valley, from a slope etc. Thus, those anomalies can lead to erroneous interpretation if the correct topography is not taken into consideration.

The integration of the apparent resistivity data and the sequence of electrodes with the appropriate bathymetric point in a specific area was made possible with a Matlab script (Dimitrios Oikonomou personal communication). The script reads the filtered binary tomographic files, uses as input the bathymetry of the site and then it makes the necessary coordinate transformations exporting an ascii file that can be imported to the inversion software for further processing.

Even though the topography is extremely important in an ERT survey, the sea water conductivity another must be also taken into account in a marine ERT survey. The conductivity of the saline water was monitored through repeated daily measurements with a high precision and accuracy conductivity meter (**Figure 3.4**) and was then converted into resistivity. Its resistivity value was stable throughout the period and equal to 0.18 Ohm-m in both Delos and Elounda survey areas.



Figure 3.4: The YSI-Pro 30 Water Conductivity Meter used in the surveys

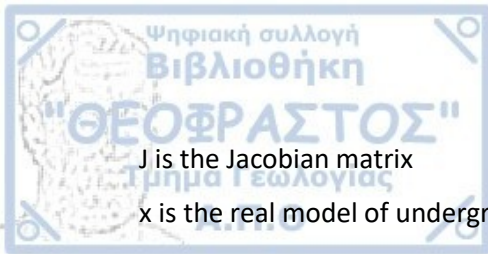
3) Inversion

As it was mentioned above, the measured quantity of the ERT method is the apparent resistivity of the subsurface, which does not correspond to the real resistivity of the subsurface because the earth is inhomogeneous. The methodological tool to estimate the real resistivity of each underground structure is the mathematical procedure of inversion.

In geophysics, the term forward resistivity problem refers to the process of calculating the observed apparent resistivity data set given a known resistivity. As expected, the inverse resistivity problem refers to the exact opposite procedure, which is to calculate the subsurface resistivity distribution given the observed data set. Inversion method tries to reconstruct a subsurface resistivity model through an iterative procedure that attempts to match the synthetic apparent resistivity measurements created by the model with the real measurements observed on the field as much as possible. (Tsourlos 1995).

The linearized inverse problem can be expressed in a formula as seen below:

$$J(x - x_0) = y - F(x) \quad (5)$$



J is the Jacobian matrix

x is the real model of underground resistivities

x_0 is the initial model of resistivities

y represents the real apparent resistivity measurements

$F(x)$ represents the synthetic apparent resistivity data which are produced after the forward problem is solved with the finite element method

The above system can be solved with the least squares method in order to estimate the correction resistivity vector dx of the initial resistivity model

$$dx = x - x_0 = (J^T J)^{-1} J^T (y - F(x)) \quad (6)$$

Thus, a new model is produced from the above equation:

$$x_1 = x_0 + dx \quad (7)$$

Since the goal of the inversion technique is to reconstruct a model that matches the real resistivity values, a number of iterations are necessary in order to minimize the difference between the real data and the response of the model. So, the final resistivity model after a number of k iterations can be represented by the equation:

$$x_{k+1} = x_k + [(J_k W)^T J_k W + m_k C^T C]^{-1} (J_k W)^T (y - F(x_k)) \quad (8)$$

W is the statistical data weight matrix

m_k is the appropriate Lagrangian multiplier

C is the model smoothing matrix

Equation (8) describes the formula of the smooth inversion process that tries to find the model with smooth variations in the respective resistivity correction vector. A different type of inversion also exists, called robust inversion which is less influenced by outliers and other non-Gaussian noise leading to the creation of more “blocky” and geologically realistic models



(Farquharson and Oldenburg 1998). The equation for the robust inversion routine is given by the formula:

$$(J^T R_d J + \lambda F_R) \Delta q_k = J^T R_d g - \lambda F_R q_k \quad (9)$$

$$\text{with } F_R = \alpha_x C_x^T R_m C_x + \alpha_y C_y^T R_m C_y + \alpha_z C_z^T R_m C_z \quad (10)$$

where M represents the number of measurements and N the number of parameters

The formula for the calibration of the R matrixes is given by Eklblom's measure:

$$R_{ii} = p(x_i^2 + \varepsilon^2)^{\frac{p}{2}-1} \quad (11)$$

ε can be any positive number

$1 \leq p < \infty$

R is a diagonal matrix given by the formula:

$$R = \text{diag}\{\rho'(x_1)/x_1, \dots, \rho'(x_N)/x_n\} \quad (12)$$

The iterative inversion process stops when the specified number of iterations are complete, or when the minimum error criteria are met. The root mean square deviation (RMS) is the main criterion by which the convergence of the theoretical and the real resistivity values is represented given by the following formula

$$\%RMS = 100 \frac{1}{m} \left(\sum_{i=1}^m \left| \frac{d_i^{obs} - d_i^{calc}}{d_i^{obs}} \right|^k \right)^{1/k} \quad (13)$$

All the inversion routines shown in this thesis took place in the Res2dinv (2D inversion) and Res3dinv (3D inversion) software. Inside the software the user can manually control a great number of parameters affecting the inversion process. Through the process of trial and error, the optimal inversion parameters for each data set were established, with the main criteria for that choice being to minimize the RMS and reconstruct a final 2D or 3D resistivity model that has respective physical meaning and corresponds to the local geological conditions.

Figure 3.5 shows a 2D inverted resistivity section along a dynamic line. The final stage of processing included a respective RMS error analysis (Figure 3.6). If the errors in the final model are deemed too high, a trimming process took place, where the outliers having large deviations are removed and a new inversion of the data was performed. Most of the inversion models shown in this thesis have been slightly trimmed based on this procedure.

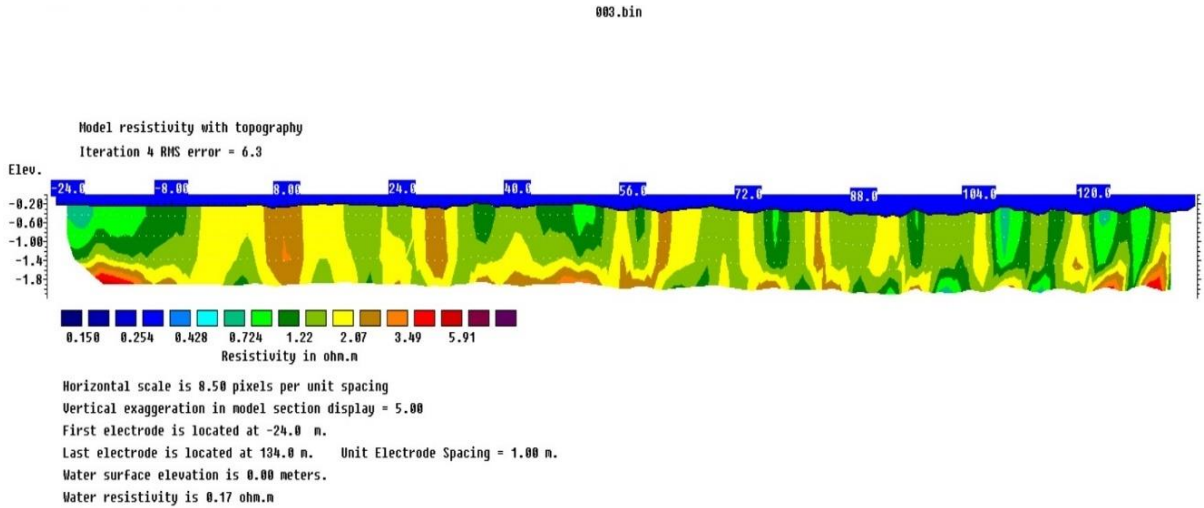


Figure 3.5: Inversion results of line 003 from the Skhardanas Dynamic ERT data set

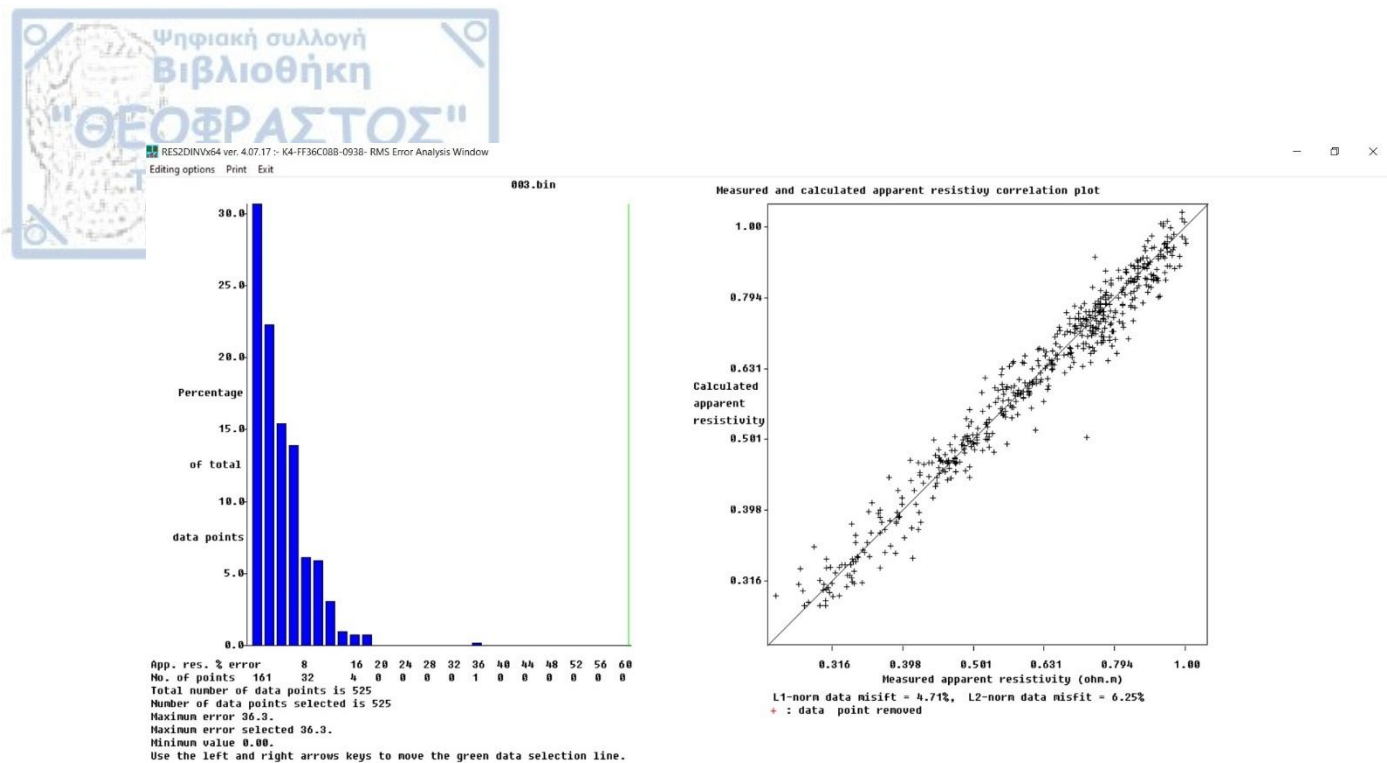


Figure 3.6: RMS analysis of a specific ERT line. Data with deviation more than 20% have been removed from the original set. The left image shows the histogram for distribution of the errors between the measured and the calculated apparent resistivity data. The right image shows the scatterplot between the measured and the calculated apparent resistivity data.

4) Pseudo 3D Volumetric Representation

Concerning the Skhardanas data set, due to the fact that the line spacing for most of the lines surveyed didn't allow for a full 3d inversion, only the 5 ultra shallow lines were selected for a pseudo 3D volumetric representation. In this final processing stage, the UTM coordinates were assigned to each one of the shallow individual 2-D resistivity sections. These were then merged to form volumetric representation of the submerged resistivity variation. A 3-D inverse distance algorithm was used for interpolation and finally horizontal slices in different depths below the sea bottom were extracted from the quasi 3-D resistivity model using Voxler v3.0 software from Golden Software to compile these depth slices (**Figure 3.7**).

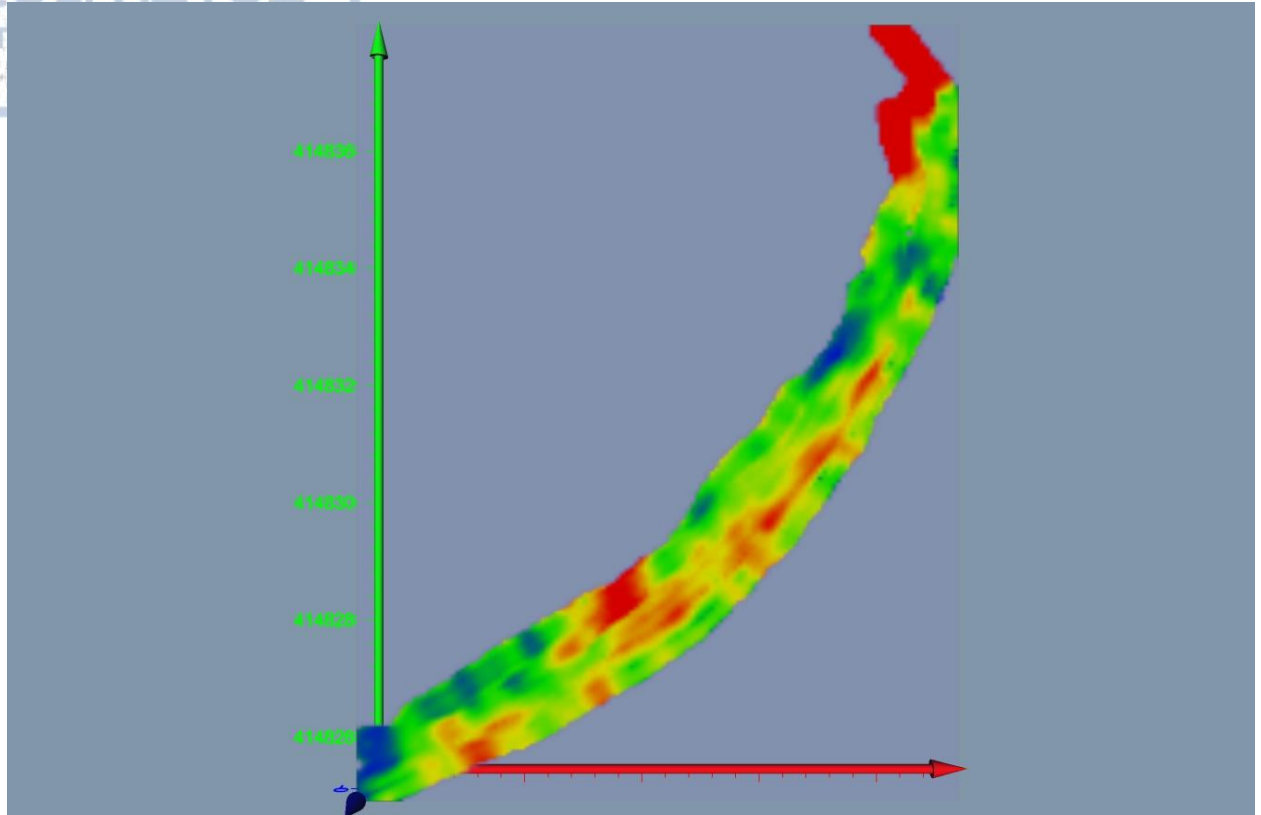


Figure 3.7: Horizontal depth slice extracted from the 3D volumetric representation of the five ultra shallow lines in Skhardanas Bay.

5) Model Grid Rotation

The model grid rotation is an option given by the Res3Dinv software. This option can be used when the survey lines are aligned at a significant angle in relation to the true North-South and East-West directions, resulting in the creation of an unnecessarily big model with empty spaces at two corners of the modelling space. By rotating the model grid, the model cells and the mesh size used in the inversion are reduced by more than half. This rotation halves the computer time and memory size needed for the inversion. (*Figure 3.8*).

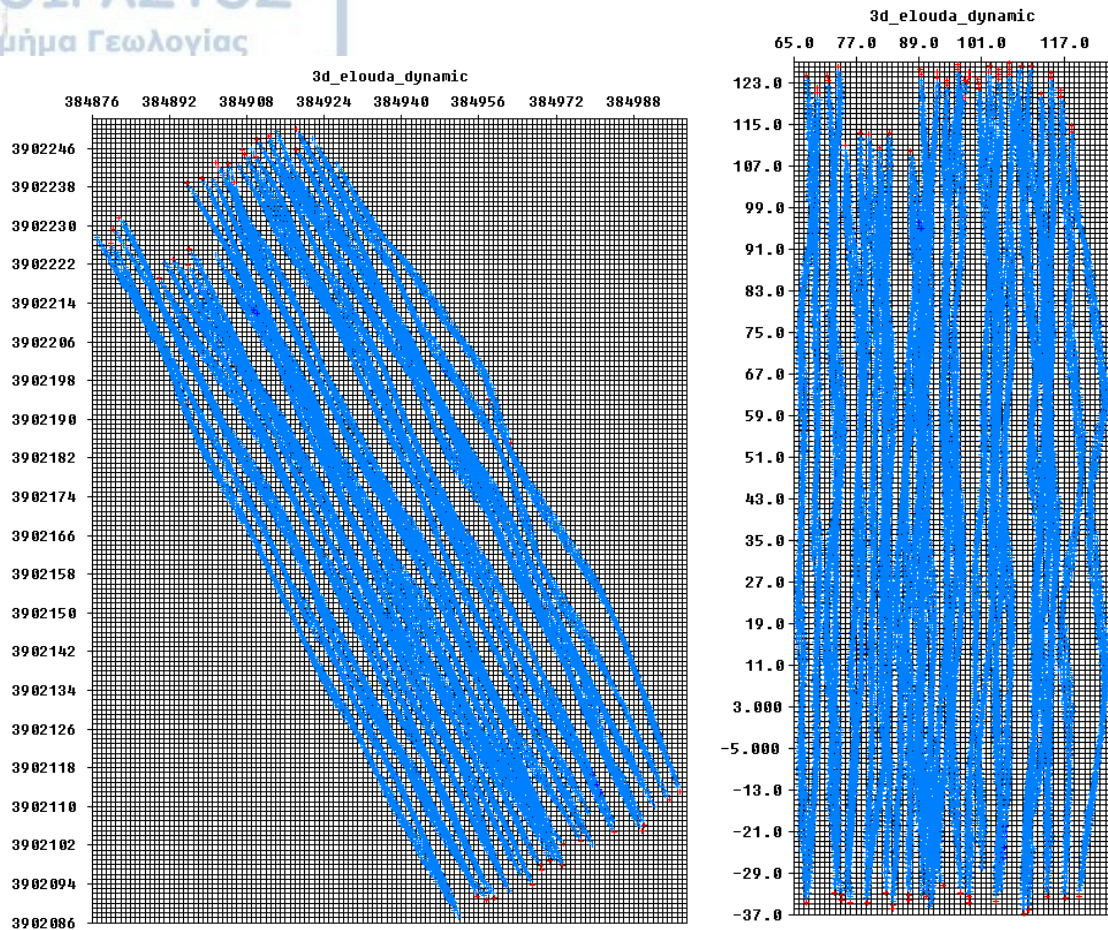
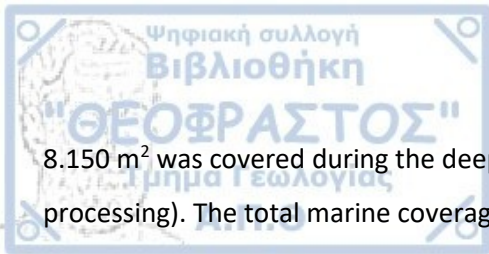


Figure 3.8: Illustration of model grids before (left) and after (right) the model grid rotation. In the rotated grid, the coordinates change from global to local, but the global coordinates remain stored in the data file

3.2 ERT Coverage and Results

3.2.1 Skhardanas Dynamic ERT

As was mentioned in chapter two, the goal of the Skhardanas survey was to collect the data along predefined parallel lines, with less than 2m spacing between them. However, this survey parameter was not met for the distance between all the lines. The drifting of the boat due to sea currents and occasional winds and the terrain difficulties presented by the rocky seabed were the main reasons for not accomplishing an even line distribution. A total of 2.235 m² was covered during the data collection of the ultra-shallow lines with the line spacing between them ranging from 1.5m to 4m, while a total of



8.150 m² was covered during the deeper line survey (including the 7 lines that weren't selected for processing). The total marine coverage of Skhardanas bay was 10.385 m² (**Figure 3.1**).

The Skhardanas Dynamic ERT data set was inverted using a smooth inversion routine. The mean RMS of the 30 lines making the final cut was 17.28% and the standard deviation 4.96. A common color scale was used for all the lines presented, as well as for the pseudo3D volumetric representation. The color scale ranges from dark blue (minimum resistivity at 0.18 Ohmm) to purple (maximum resistivity at 8.7 Ohmm).

Figure 3.2 shows the marine coverage of the 5 ultra-shallow lines and **Figure 3.3** shows the marine coverage of the three representative deeper lines selected for presentation. In **Figure 3.4** the inversion results for the ultra-shallow lines can be seen, while in **Figure 3.5** the inversion results of the representative deeper are presented. Finally, in **Figure 3.6** a depth slice of the pseudo3D representation of the ultra-shallow lines is rectified in an orthophoto of Skhardanas bay.

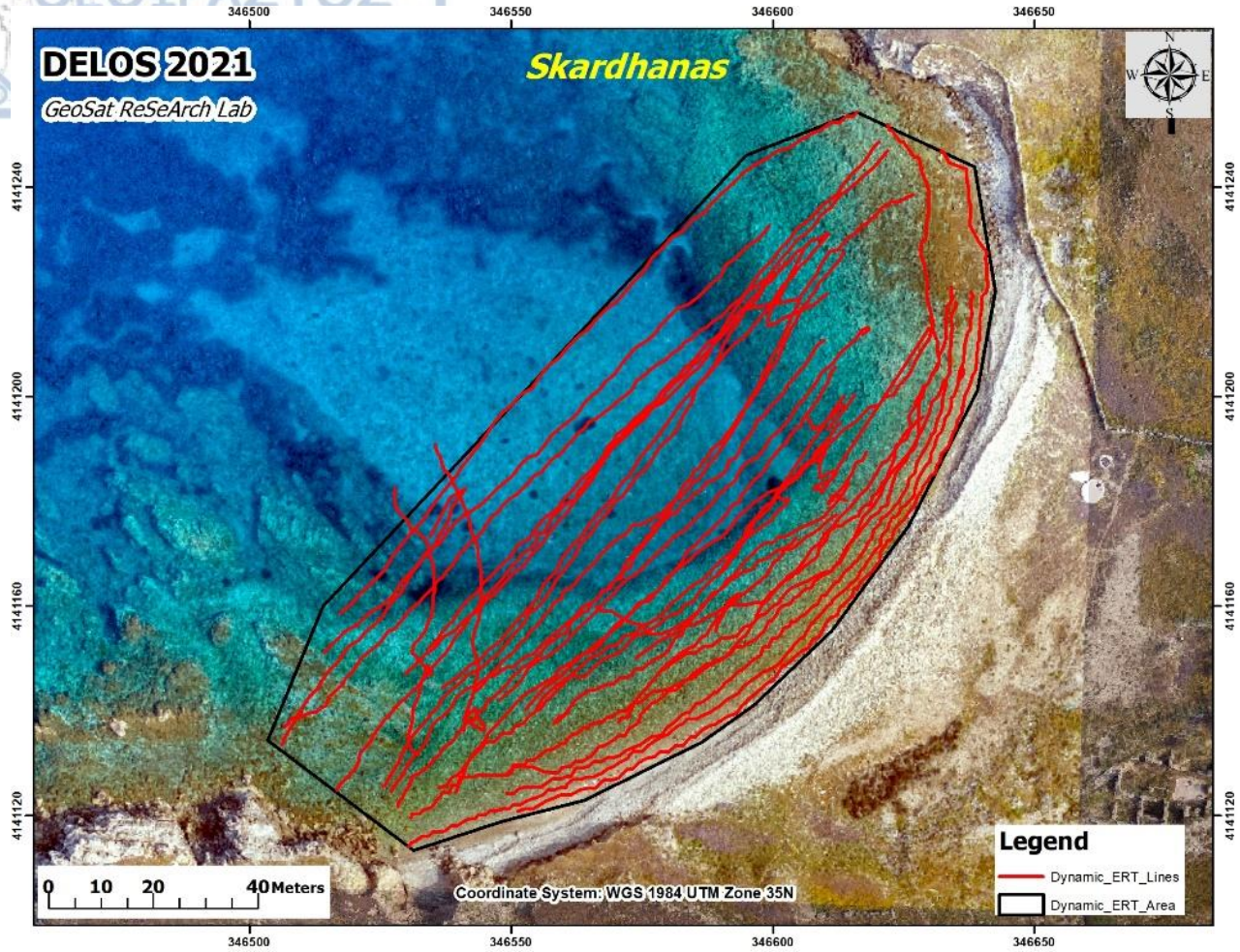


Figure 3.1: Orthophoto of Skardhanas Bay outlining the marine coverage of the Dynamic ERT technique

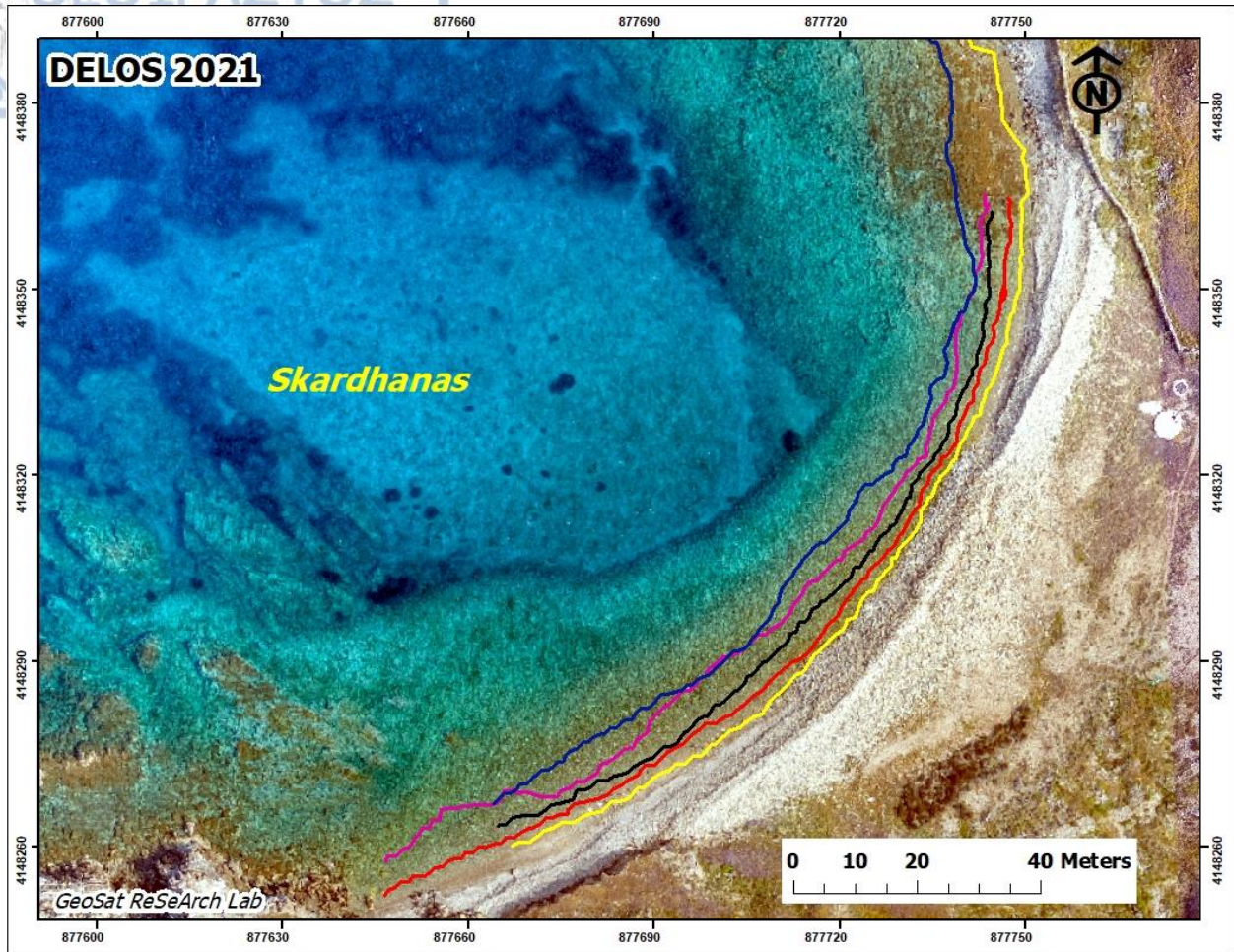


Figure 3.2: Orthophoto of Skardhanas Bay outlining the marine coverage of the ultra-shallow lines



Figure 3.3: Orthophoto of Skardhanas Bay outlining the marine coverage of the representative deeper lines

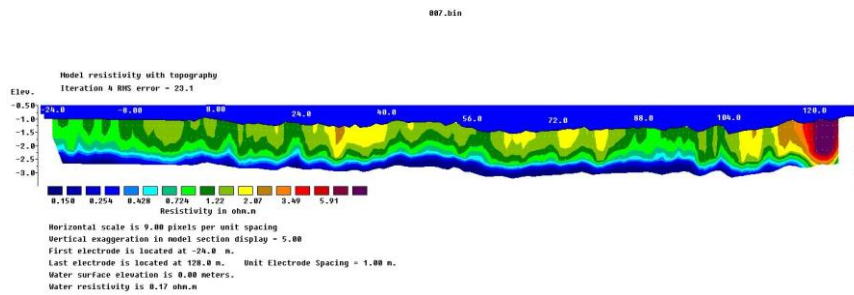
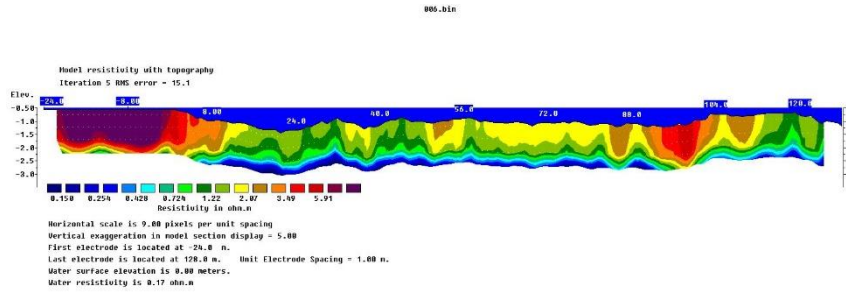
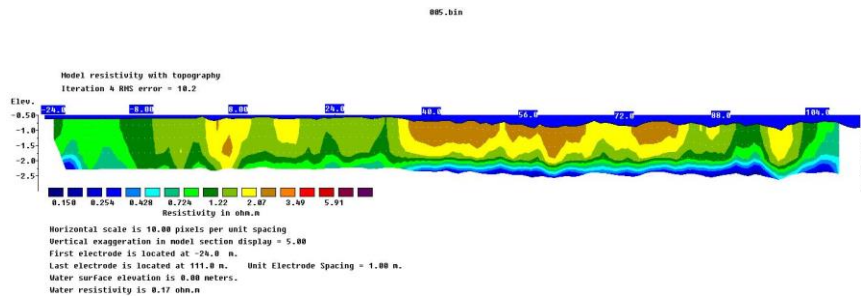
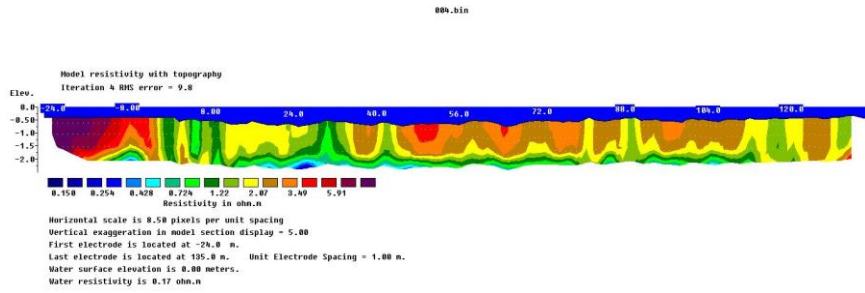
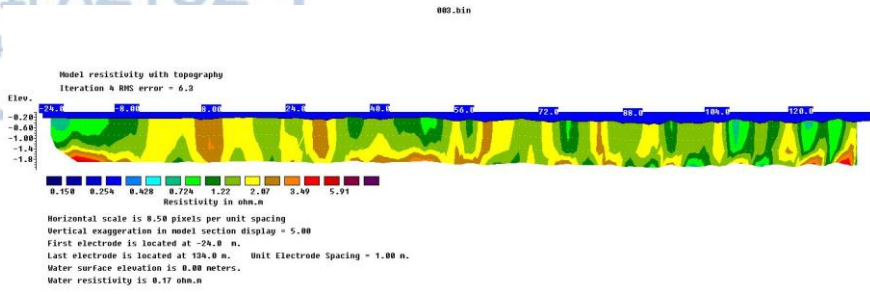
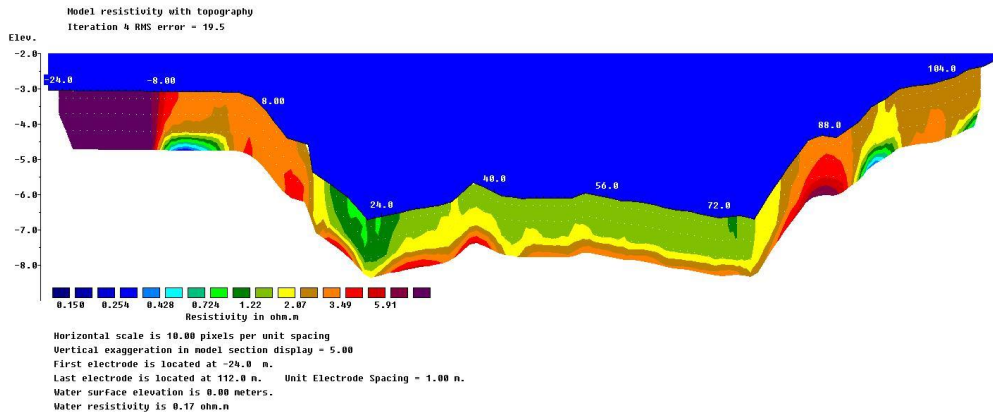
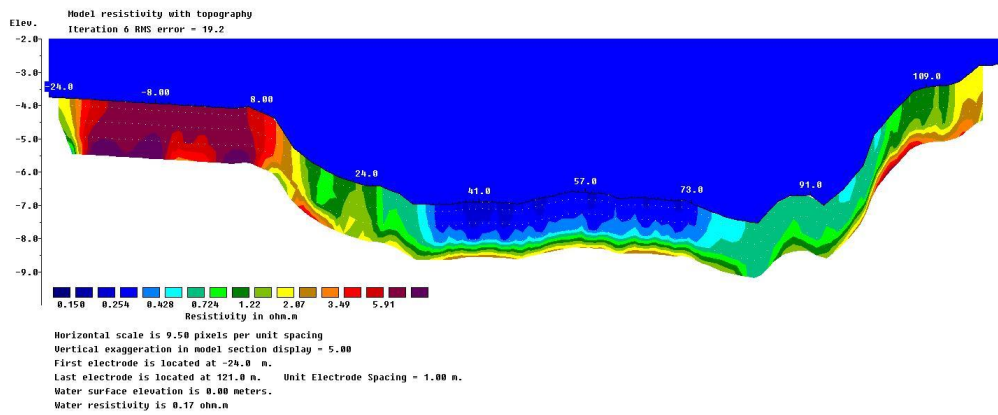


Figure 3.4: Inversion results of the ultra-shallow lines surveyed in Skhardanas Bay (Lines 003,004,005,006,007)

010.bin



018.bin



022.bin

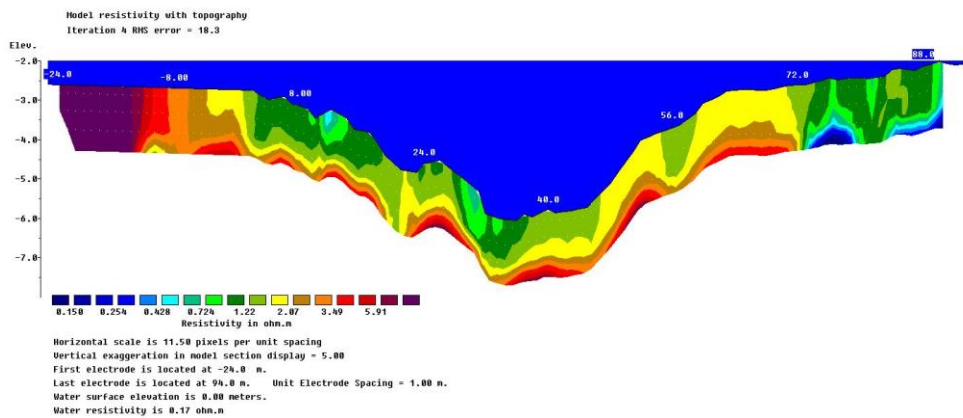


Figure 3.5: Inversion results of three representative deeper Dynamic ERT lines in Skhardanas Bay (Lines 013, 018, 022)

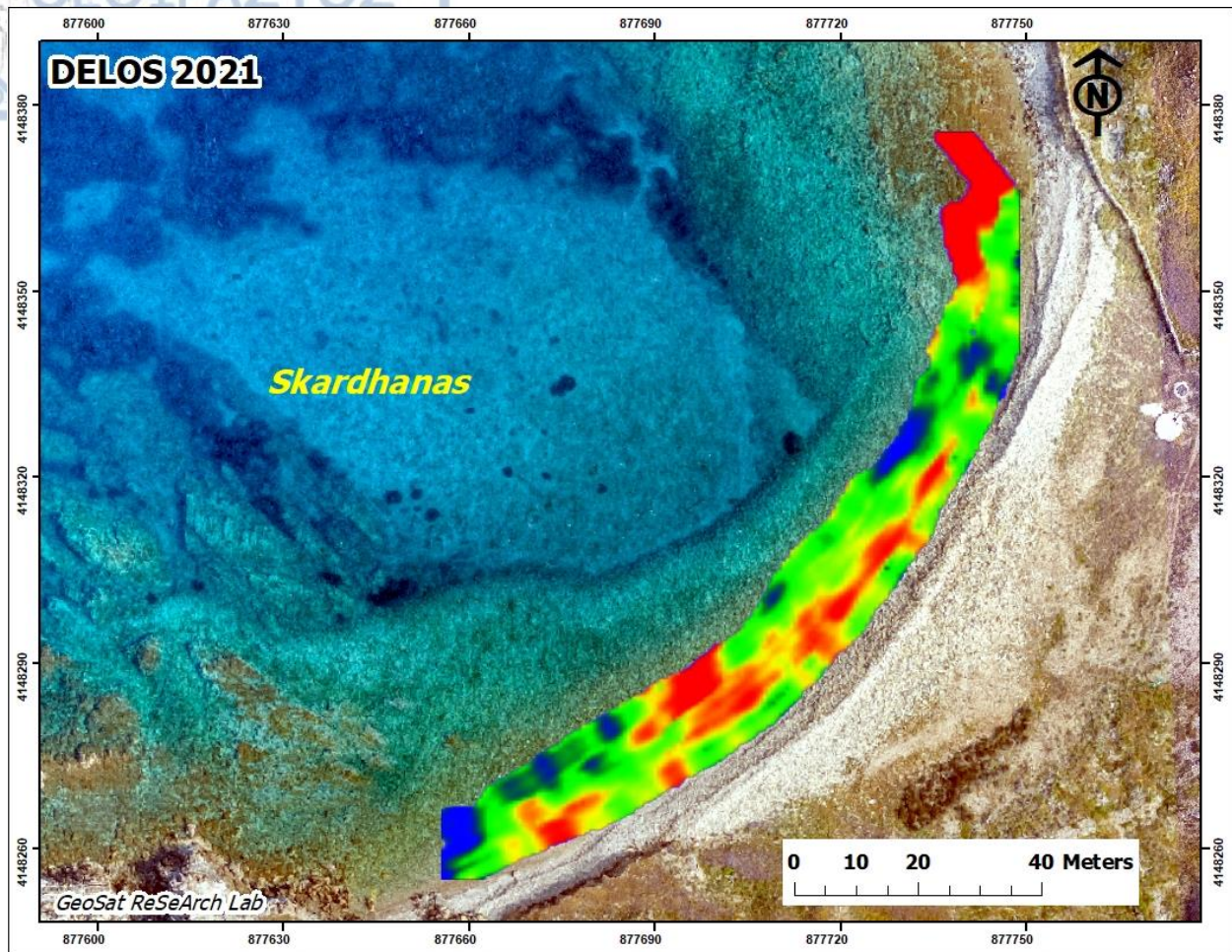


Figure 3.6: Orthophoto of Skhardanas Bay with the rectification of a resistivity slice for depth of less than 1m of the pseudo3D representation of the ultra-shallow lines

3.2.2 Olous Dynamic ERT

Totally twenty seven (27) dynamic ERT lines were surveyed in the southern part of Olous Bay covering a marine area of about 10.000 m²(**Figure 3.7, Figure 3.8****Figure 3.7**). The same methodology that was followed in Skhardanas bay was used in Olous as well. The boat was moving along predefined parallel lines and the lines had an approximate 2m spacing between them. In contrast to Skhardanas Bay, south Olous Bay was protected from winds and the sea-bottom topography was far less rocky. This allowed the boat to survey along straight lines with the predefined spacing between them.

The nature of the specific tomographic data sets allowed the processing and inversion with a 3D inversion program. Despite the ideal in situ conditions during the data collection, it is virtually



impossible to achieve perfect parallel lines when moving in the sea. That slight diversion caused the appearance of many artefacts in the first layer, during the first trial inversion runs. In order to eliminate this problem, the damping factor of the only the first layer was set at 5.00, while damping factor for the remaining layers initiated from 0.1 and slightly increased with depth to account for the limited resolution of the deeper layers. Lastly, the vertical-to-horizontal roughness filter weight was set at 0.5

Σφάλμα! Το αρχείο προέλευσης της αναφοράς δεν βρέθηκε..

Moreover, the number of layers and the depth of each layer was modified manually. The finite-element forward modeling method was used, with a 2-node horizontal mesh size. Test inversions were run with 3 and 4 nodes, but the change in accuracy was minimal while the required time for the process to complete was more than doubled.

After many lengthy trials, a robust inversion routine was selected. The inversion was carried out using a computer equipped with a CPU Intel Xeon E5-2630 2.2 GHz and 128 Gb Ram memory in a 64 bit windows system using the Res3Dinv software. The inversion process took 9 hours to complete.

Figure 3.9 shows the inversion results of the south Olous Bay dynamic survey as depth slices exhibiting RMS=32.8% after three iterations.



Figure 3.7: Originally Planned Marine Coverage with the Dynamic ERT technique of Ancient Olous South Bay



Figure 3.8: Marine Coverage with the Dynamic ERT technique of Ancient Olous South Bay

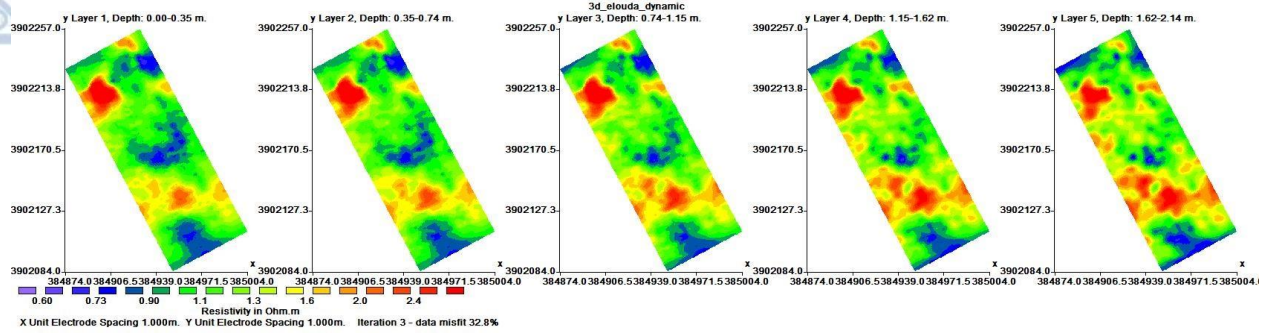


Figure 3.9: 3D Inversion Results of Elounda Dynamic ERT

3.2.3 Olous Static ERT

The Olous Static ERT survey collected data from two grid in the northern part of North Olous bay (*Figure 3.10*). The size of the East grid was set at 30mX47m while the size of the West grid was 20X47m. This means that thirty-one (31) lines were surveyed in the East grid, while twenty (21) lines were surveyed in the West grid, all with 1m spacing between them. The marine area covered with both grids was 2.350 m². Both data sets were 3D inverted in the Res3Dinv software with a smooth inversion routine. In *Figure 3.11* the inversion results of the East grid are presented and in *Figure 3.12* the results of the West grid are shown. The RMS was 3.8% for the East grid and 2.44% for the West grid.



Figure 3.10: Orthophoto of North Olous Bay showing the East (right) and the West(left) static ERT grids

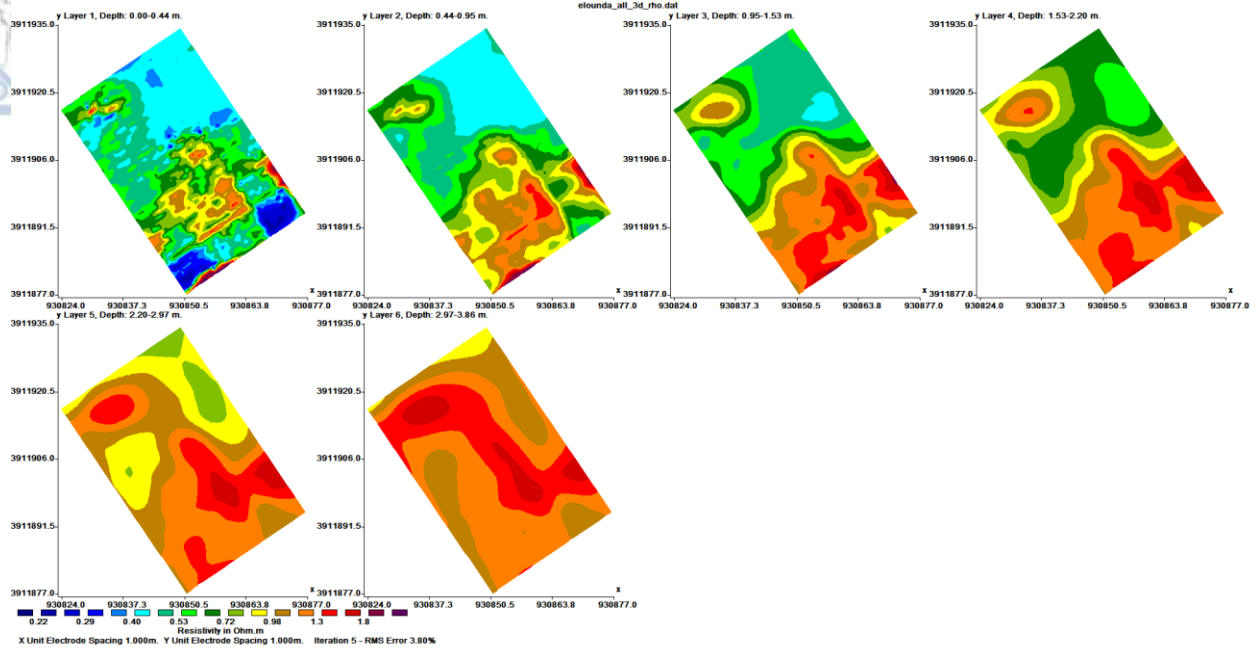


Figure 3.11: 3D inversion results of East static ERT grid

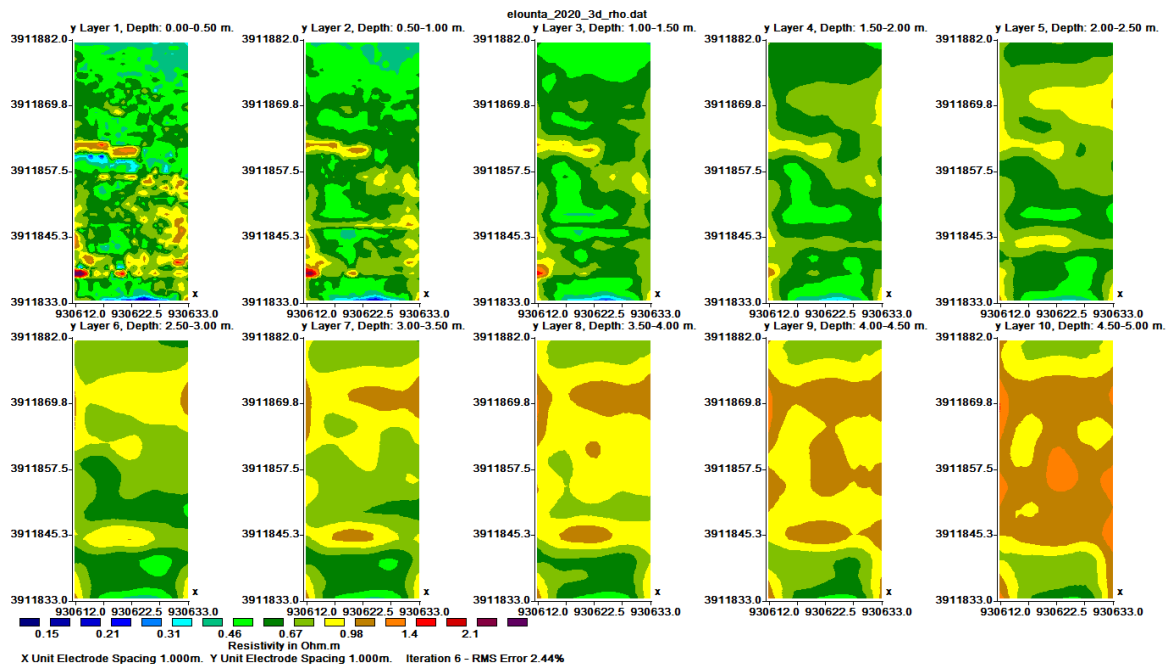


Figure 3.12: 3D inversion results of West static ERT grid

3.3 Multisensor Magnetic Gradiometry Processing

1) Track Inspection and Export

The first step of processing the multisensor magnetic gradiometry data is done through the DLMGPS software. The raw magnetic data files from twenty three (23) track lines are imported into the software where the user can inspect the length of each track and discards the short or faulty ones. During the magnetic survey, it is a common possibility that the line surveyed is interrupted and resurveyed due to terrain or equipment difficulties. Therefore, those unnecessary lines were excluded by the software and a total of nineteen (19) track files remained for further processing. In **Figure 3.1** the magnetic survey tracks are displayed along with their correct coordinates which are automatically imported from the MonMX 4.0 software.

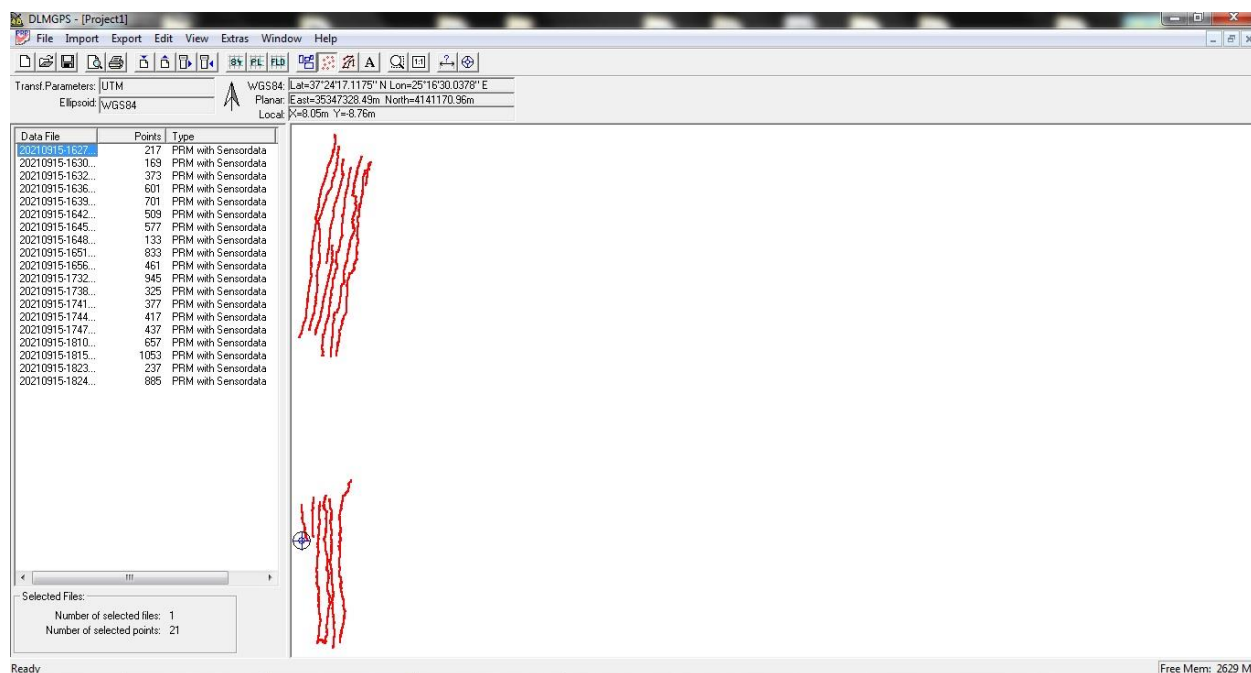
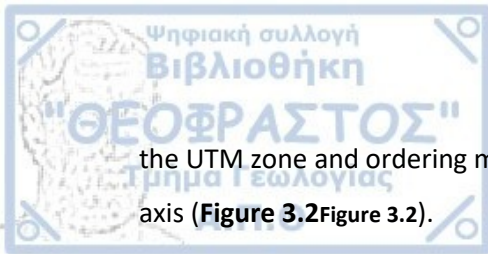


Figure 3.1: Footprint of the tTrack lines of the magnetic survey inside the DLMGPS software.

After the initial inspection, the raw files are then exported as an ASCII files in order to further continue the data processing. This involves readjusting Planar X, Y coordinates with respect to



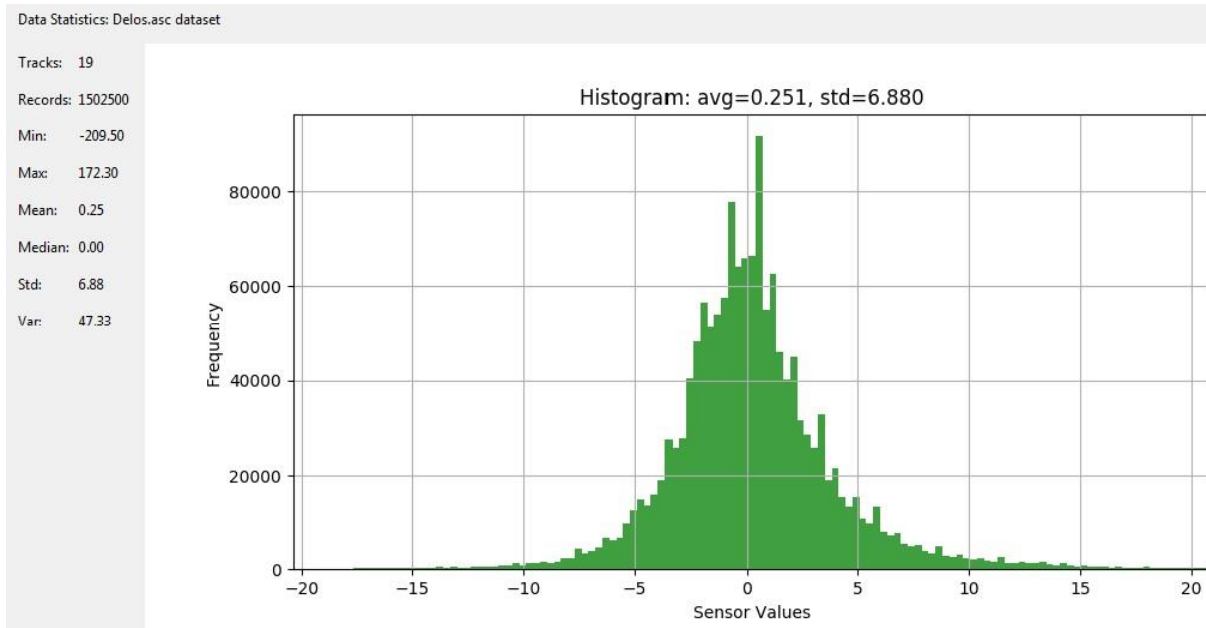
the UTM zone and ordering multi-channel data so that it becomes a linear transect along the Y axis (Figure 3.2).

PLANAR X-Coord	PLANAR Y-Coord	Value	Track ID	Sensor Number
34653845.002	4339515.568	-7.0	20131113-115922.prm	5
34653845.498	4339515.630	-1.2	20131113-115922.prm	6
34653845.994	4339515.692	-6.4	20131113-115922.prm	7
34653846.490	4339515.754	-2.4	20131113-115922.prm	8
34653849.321	4339518.274	-13.1	20131113-120117.prm	1
34653848.862	4339518.077	-17.1	20131113-120117.prm	2
34653848.403	4339517.880	-21.4	20131113-120117.prm	3
34653847.943	4339517.682	-11.6	20131113-120117.prm	4

Figure 3.2. Sample output for SENSYS sensor data and their corresponding coordinates.

2) Calibrate All sensors on all tracks

When the data are imported into the Sensys.exe software, the distribution of the recorded magnetic values from all the sensors can be inspected through a respective histogram. The first step of processing requires a calibration of all sensors on all tracks, so as to secure that all the values measured from all the magnetic sensors are brought to the same level (0-level) (Figure 3.3).



Data Statistics: Delos.asc dataset

Tracks: 19

Records: 1502500

Min: -209.75

Max: 172.05

Mean: 0.00

Median: -0.25

Std: 6.88

Var: 47.33

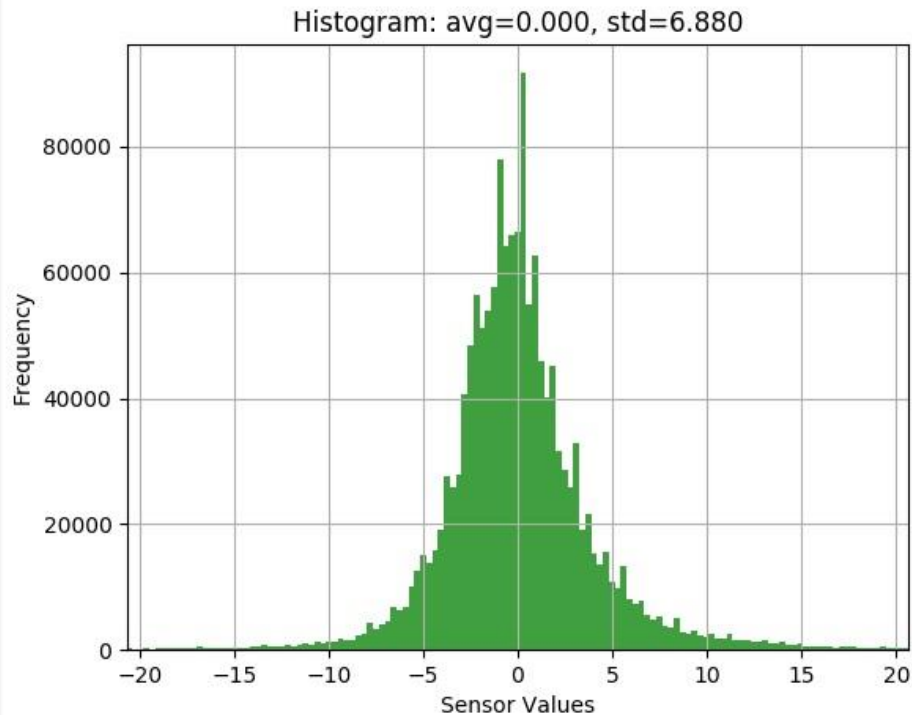


Figure 3.3: Histogram of raw magnetic values before (up) and after the sensors calibration (down).

3) Clip Track Data

The next step of processing involves despiking the data set from outliers. Due to the large volume of geomagnetic data in a unit area, it is not easily possible to employ a moving window methodology for detecting outliers in an efficient manner. This approach would take considerably long processing time to detect outliers since the window has to visit each node for descriptive statistics. To overcome this problem, a sensor transect is considered as a single dataset and the tool searches for outliers based on phase-space method. The clip track data tool conventionally clips data with user-defined upper and lower clipping values, in this case -50 to 50 n/T (**Figure 3.4**). The tool reduces the data range between these upper and lower values so that more information becomes available in 8-bit data. In **Figure 3.5** below, the corresponding histogram after the data clipping can be seen.

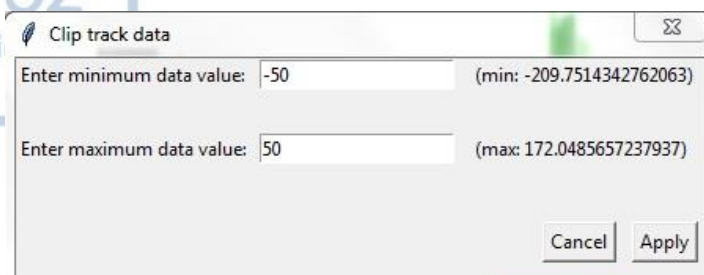


Figure 3.4: Data minimum and maximum clipping tool

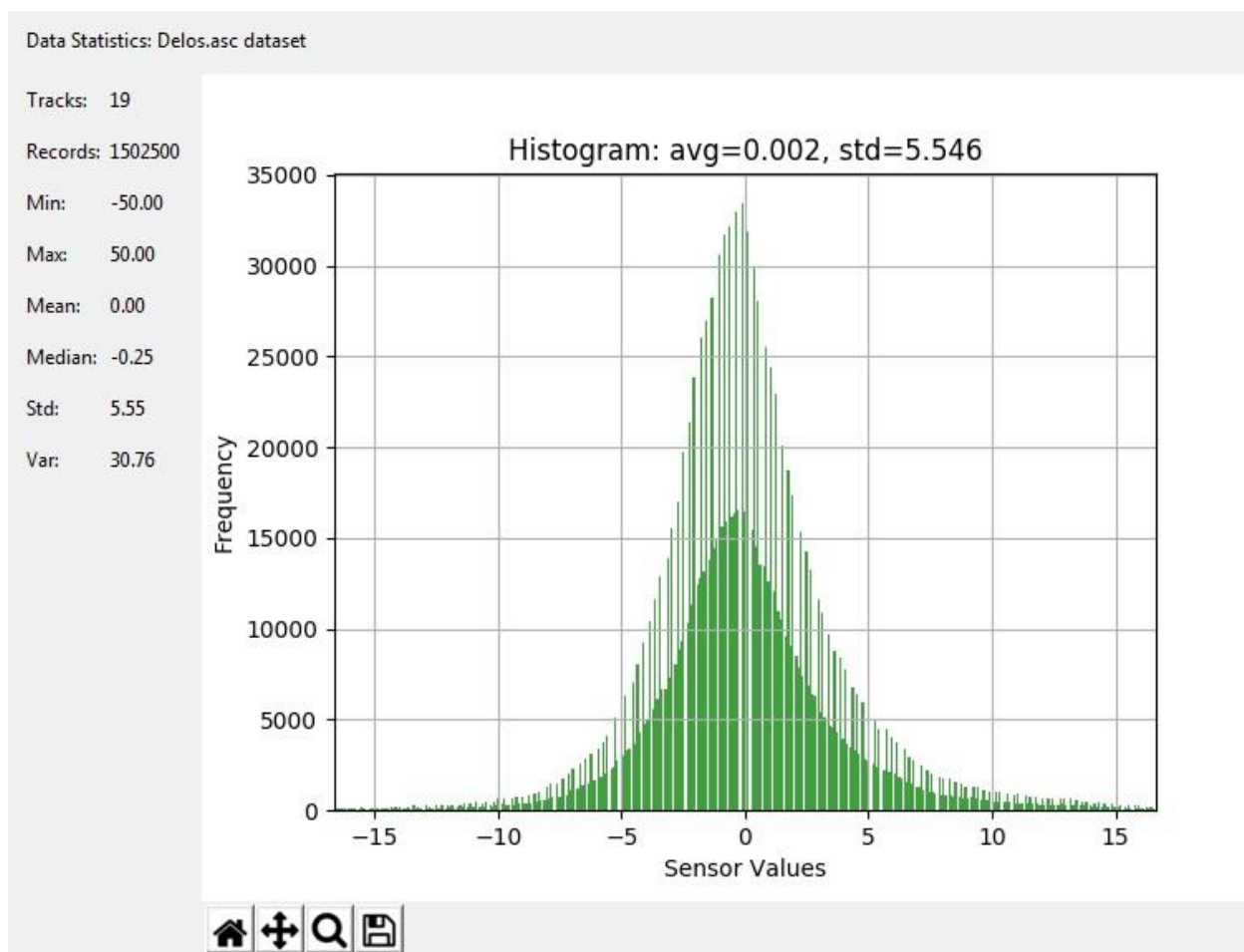


Figure 3.5: Histogram of sensor values after the track data clipping

4) Overlapping Points Removal

Geomagnetic data interpolation provides better results when there is even coverage of transects over the survey area with a minimum overlap between transects. In the case of an



overlap, interpolation produces satisfactory results only when data collection is performed under similar conditions (e.g., same distance between the sensor and the ground or same rotation angle between the sensor and the normal of the ground). In very few cases, survey is replicated with the exact setting so that for the same exact location there might be multiple readings. This creates a problem in interpolation, especially when the data is dense. Similarly, interpolation is problematic when there are considerable data gaps within the dense point pattern (**Figure 3.6**). While it is possible to sparse data for the first case in order to create a better dataset for the interpolation, the only way to “correct” for the second case is to adjust interpolation parameters for visual improvements. Here, the focus is on the first case and the solution of the second case is left for better data collection in the field. Thus, the remove overlapping points tool of the **sensys.exe** software was used. By using that tool, the interpolation of the magnetic data set provides the user with the optimal results and the size of the data file is reduced, making the final processing stages of the data set less time consuming.

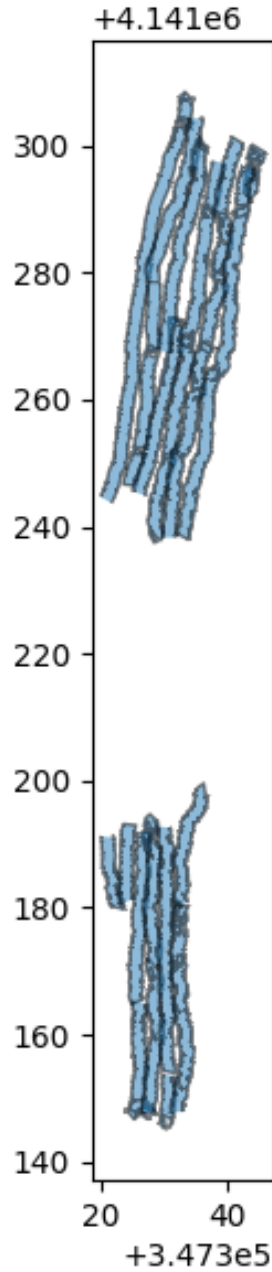


Figure 3.6: Sensys exe picture, depicting all the tracks. The areas where the tracks are overlapping, as well as the data gaps can be seen.

5) Geomagnetic Map Creation, Blanking and Low-pass Filtering

The final steps of the processing takes place inside the Surfer software. First, the data are exported to the surfer program where an interpolated grid (grd) file is compiled made which is

used to create a geomagnetic map of the survey area. Since both survey grids were treated as a single data set, the interpolation produced an undivided geomagnetic map. Thus, a blanking of the unsurveyed parts is required. Finally, a Gaussian Low Pass filter was employed to remove the high frequency noise thus resulting in a smoother grid (**Figure 3.7**).



Figure 3.7: Final Geomagnetic Results of Stadio Bay survey

3.4 Multisensor Magnetic Gradiometry Results

The results of the multisensory magnetic gradiometry performed in Stadio bay are presented in **Figure 3.1**. The specific map shows the magnetic results in the whole region covered with the magnetic gradiometry technique summing 1.443 m², divided in 942 m² in the northern region and 501 m² in the southern. **Figure 3.2** presents the results in the northern region, while **Figure 3.3** presents the results in the southern.



Figure 3.1: Magnetic gradiometry map for the whole region that was covered in Stadio Bay

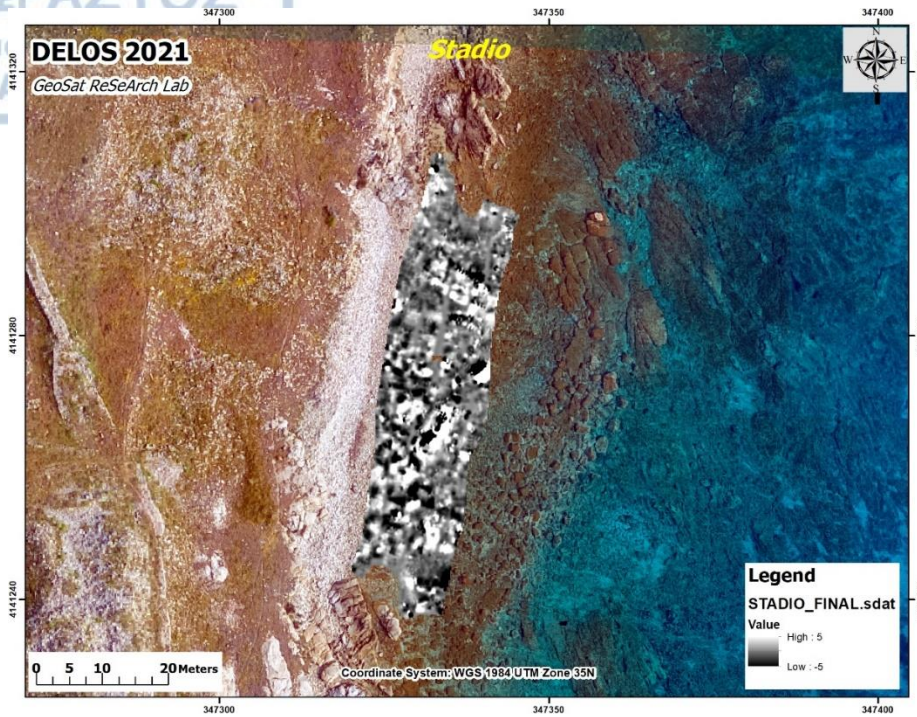


Figure 3.2: Magnetic gradiometry map for the northern region of Stadio Bay



Figure 3.3: Magnetic gradiometry map for the southern region of Stadio Bay

3.5 Bathymetry Results

3.5.1 Skardhanas Bay Bathymetric Results

At Skardhanas bay a total number of 3,444 points with values ranging between 2.45 meters above mean sea level (amsl) and -12.42 meters below mean sea level (bmsl) with an average depth of -4.06 covered about 24,000 square meters. The bathymetry data points were then interpolated using a minimum curvature algorithm with a cell size of 0.1m to compile the respective bathymetric model (*Figure 3.1*).

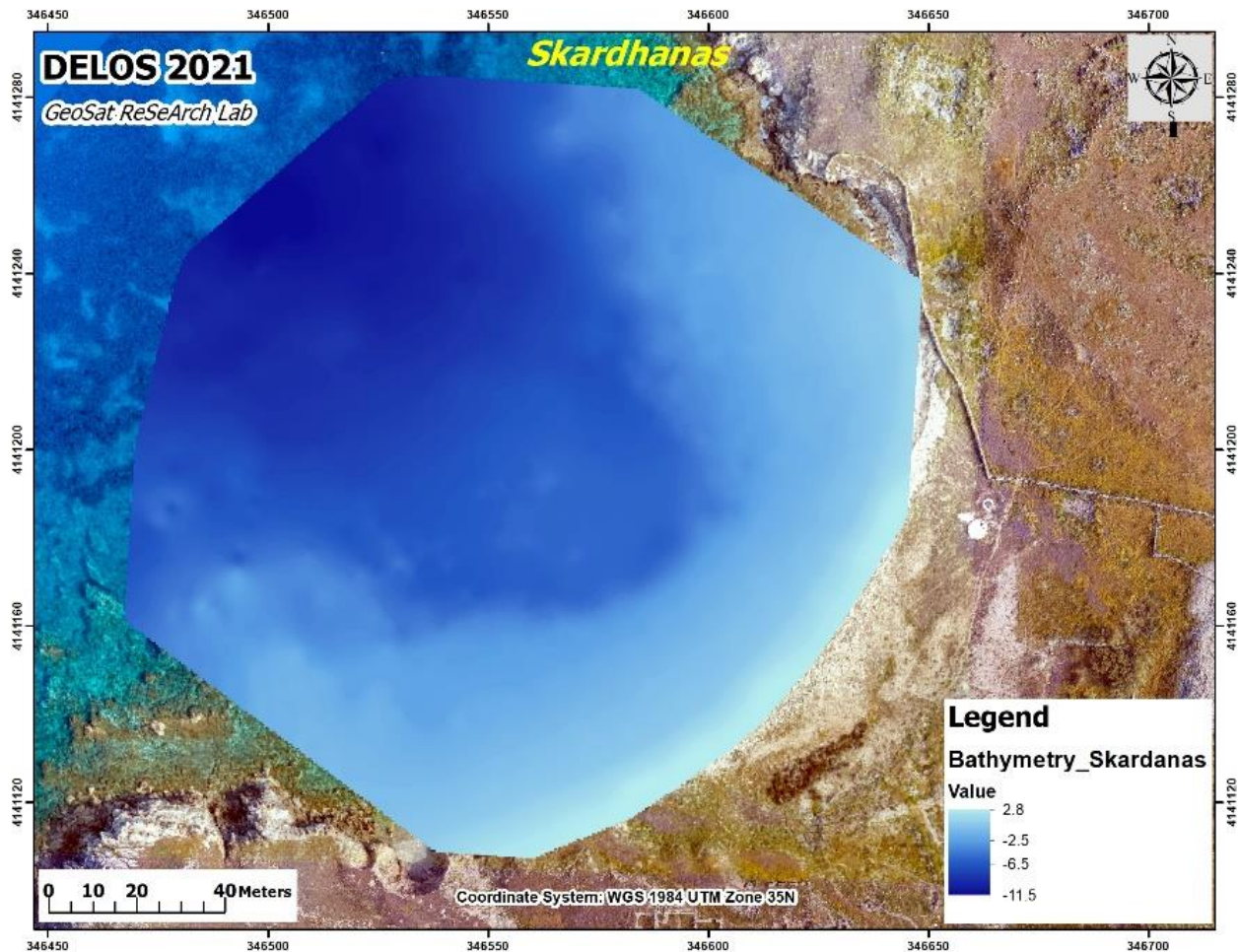


Figure 3.1: Bathymetric Results in Skardhanas Bay

3.5.2 Ancient Olous Bathymetric Results

Concerning the Ancient Olous Bathymetry, an extended bathymetric survey took place, covering all of the south bay and a large portion of the North. In this thesis, only the bathymetric results of the grids which were surveyed using the static and dynamic ERT techniques will be shown. The elevation of the 3 surveyed grids ranged from 0.134m above sea level, to 4.32m below sea level (**Figure 3.2**).

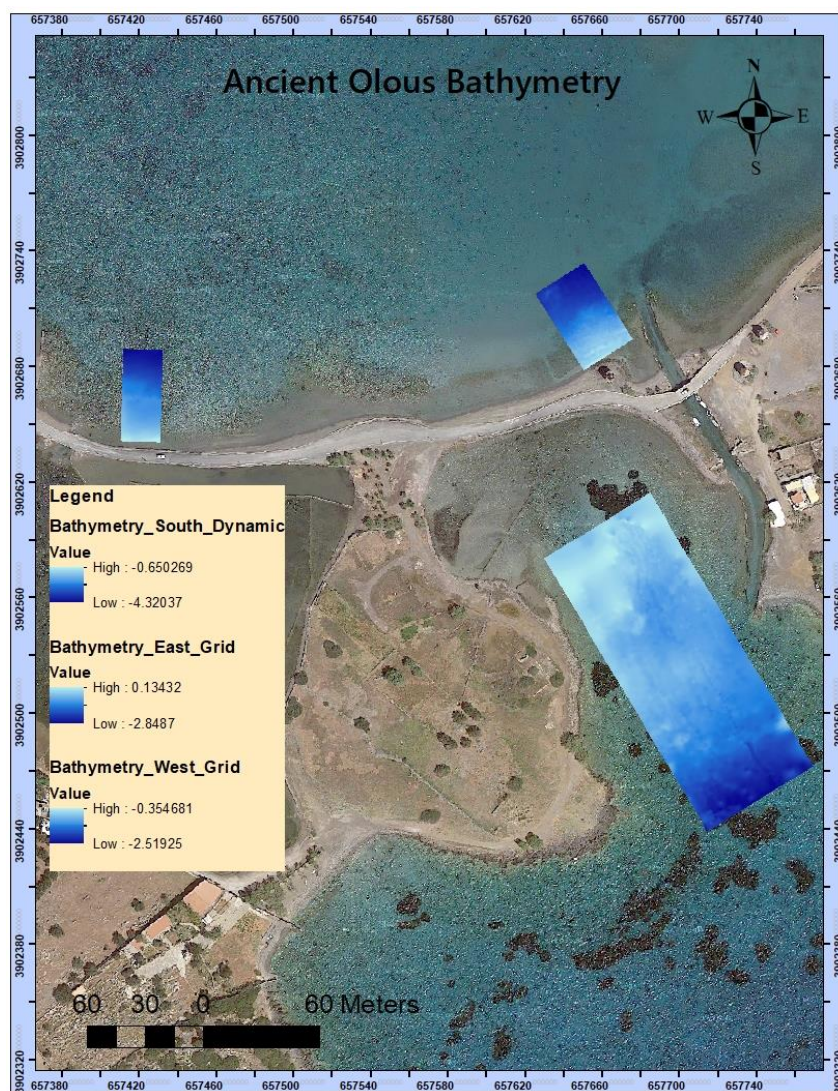


Figure 3.2: Map of Ancient Olous with the rectification of the bathymetric results corresponding to each ERT grid

Chapter 4- Interpretation

This chapter shows the interpretation of the results of all the data sets presented in the previous chapters. The final maps resulted from the processing of all the different geophysical data were rectified in the coordinate system WGS1984 UTM35N. Orthophotos and Google Earth satellite images were used as base maps to overlay the respective geophysical maps. All the cartographic outputs were integrated in a GIS environment using ArcGIS 10.7. The final geophysical maps suggested a number of candidate anomalies resulting from the interpretation of the processing procedures from all the techniques.

4.1 Delos Island Surveys Results Interpretation

4.1.1 Skhardanas Bay Dynamic ERT

Regarding the five (5) ultra-shallow lines, the buried cultural layer that is the target of this survey can be expected to exist within the first meter of the sections.

Line 003 outlines four distinct resistive anomalies possibly related to submerged targets. The first target is located at 32m from the beginning of the line, the second at 50m, the third at 85m and the fourth at 100m. The estimated thickness of each target is approximately 1.5m, 1.3m, 1.2m and 1.2m respectively.

Line 004 shows totally seven possible targets, located at 60m, 70m, 85m, 95m, 105m, 120m and 150m from the beginning of the line. All these structures seem to be around 1m thick except the seventh one which is relatively thicker and about 1.5m.

In **line 005** three possible targets can be seen. The first one is located at 30m from the beginning of the line. The second target occupies a relatively larger zone along the line and is divided into three smaller sections targets (2a located at 65m, 2b located at 80m and 2c located at 100m). The third potential target is outlined at about 125 m from the beginning of the line. The estimated thickness of all these features lies within 1.3 to 1.5m.

The deeper conductive layer is associated with seawater saturated sands. Five resistive anomalies showing correlation with structural remains have been mapped in **line 006** at a distance of about 60m, 65m, 110m, 120m and 135m from the beginning of the line. The estimated thickness of each target is

about 0.5m, 1m, 1.3m, 1.5m and 1m for each target respectively. Finally, the same conductive layer observed at the previous line can be observed in this line as well.

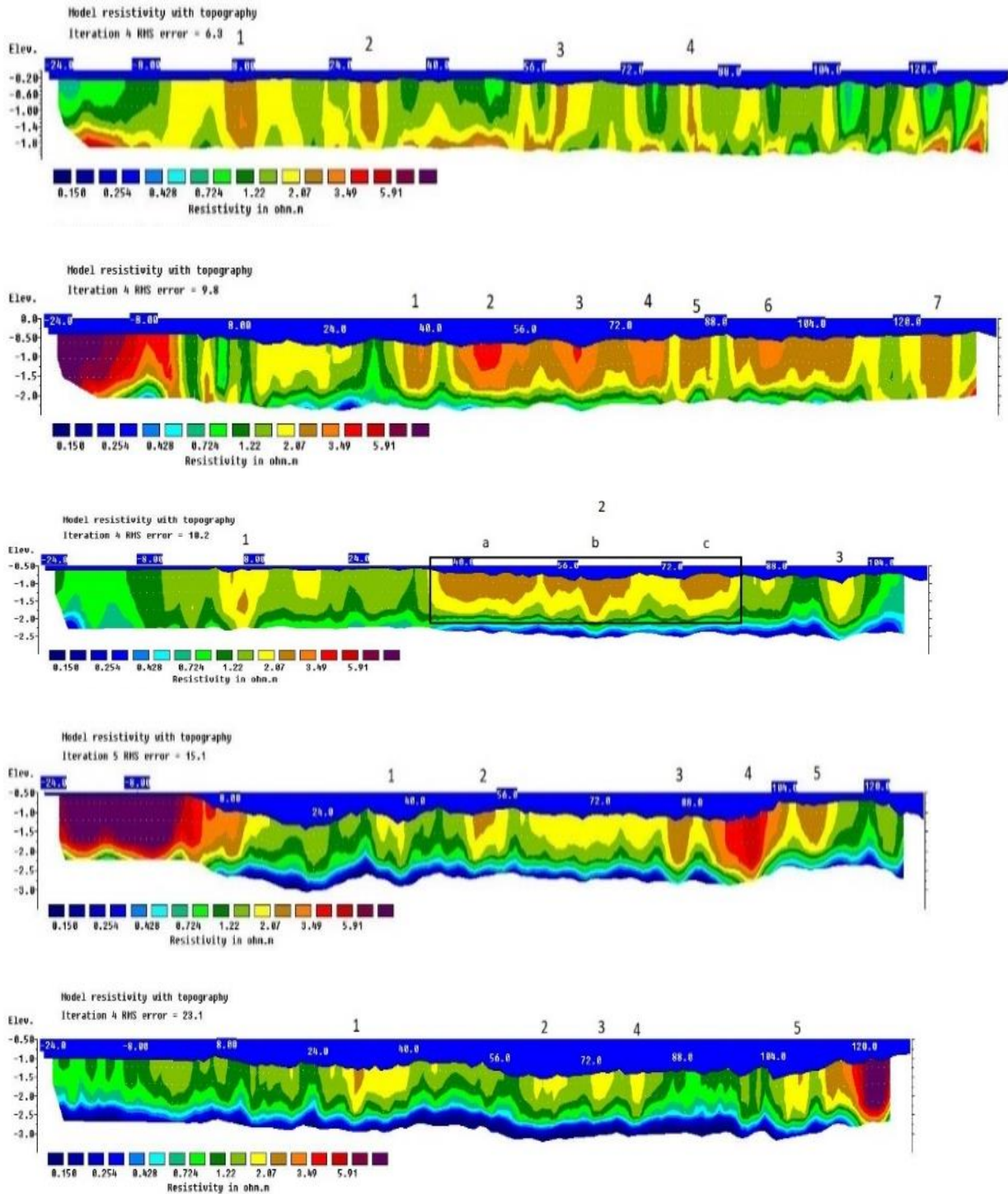


Figure 4.1: Inversion Results of the ultra-shallow lines along the shores of Skhardanas bay, with the possible targets marked

Line 007 shows five possible targets at about 55m 85m, 95m, 100m and the 135m from the beginning of the line with thickness of about 1m, 0.5m, 0.5m, 0.6m and 1m respectively. The same conductive layer can be observed at the entirety of the deeper parts of the line. The vertical sections from lines 005, 006 and 007 show a deeper conductive layer that is attributed to a sandy horizon saturated with salty water (Σφάλμα! Το αρχείο προέλευσης της αναφοράς δεν βρέθηκε.).

Figure 4.2 presents the diagrammatic interpretation of the depth slice from depth of 0.5m below the seabed. This interpolated slice was made by combining the five ultra-shallow lines creating a pseudo-3D volumetric representation of the seabed. In the slice the resistive regions related to archaeological features can be seen, as well as the target's number in the respective 2D line it was first observed.

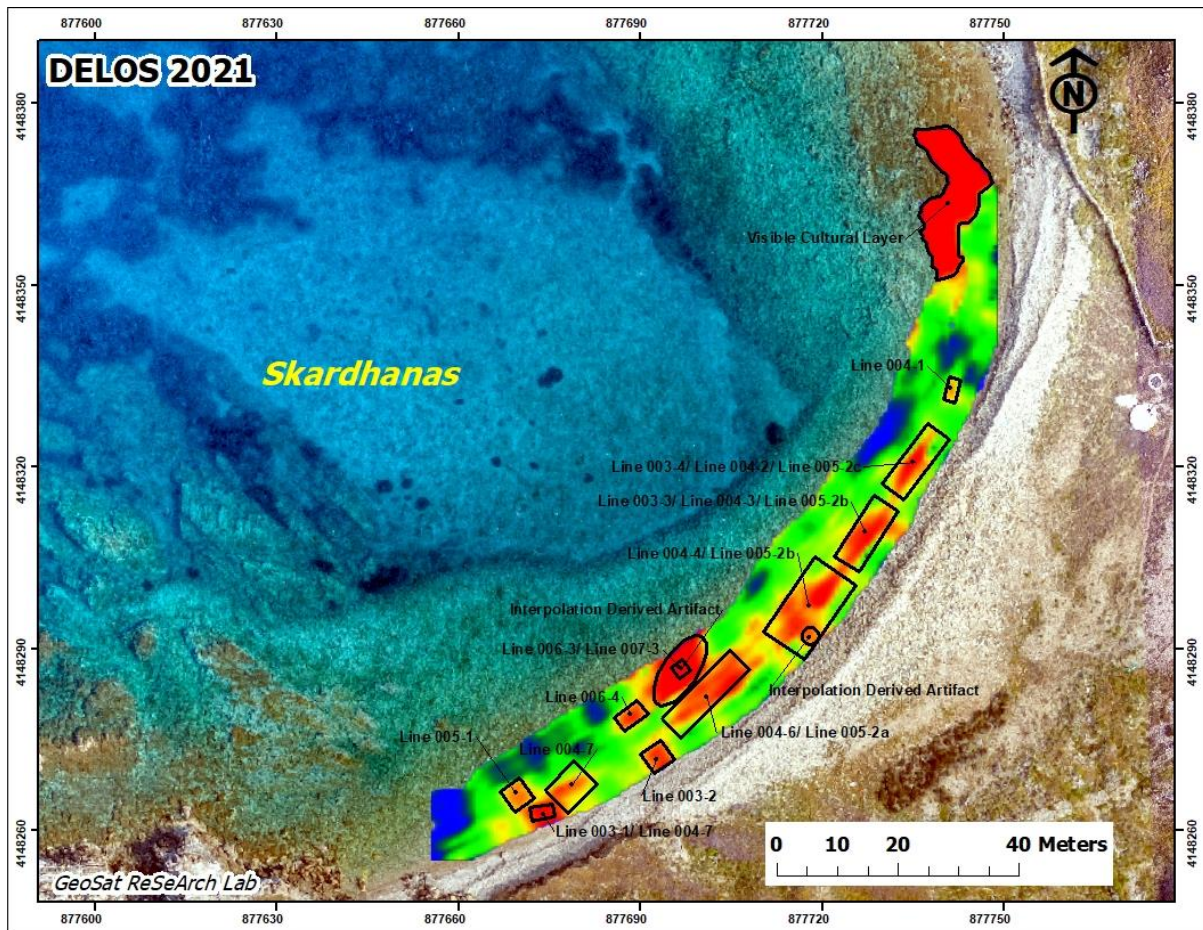


Figure 4.2: Diagrammatic Interpretation of the pseudo 3D depth slice with the possible targets marked and the corresponding ultra-shallow line the target was also seen marked

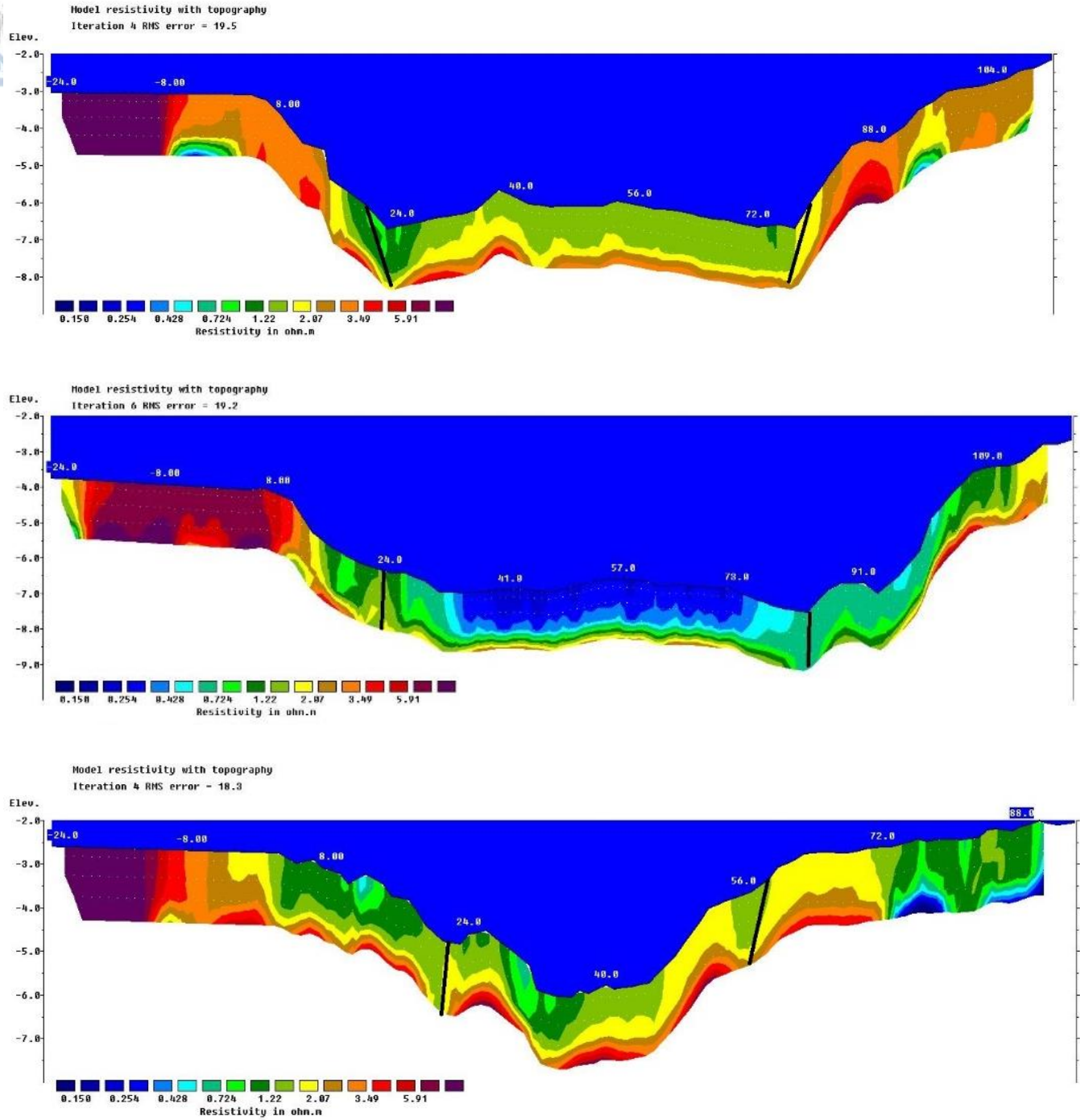
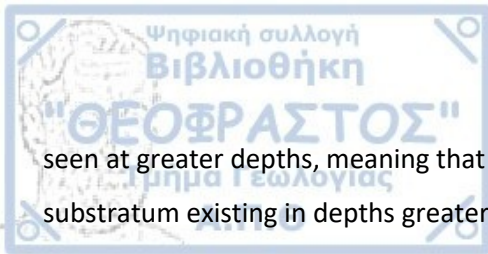


Figure 4.3: Inversion Results of lines 013,018 and 022 in the deeper parts of Skhardanas bay, with the possible faults marked.

Concerning the deeper lines, a common pattern is seen based on the resistivity vertical sections. Most of the lines show a shallow conductive layer associated with seawater saturated sands, followed by the deeper and more resistive substratum. The occasional highly resistive targets at shallow depths can be attributed to the granites-granodiorites that occupy the area. In some cases, the conductive layer can be



seen at greater depths, meaning that the saturated sands layer continues in that depth, with the granitic substratum existing in depths greater than the surveys maximum depth of investigation. Finally, two possible faults can be observed in most of the slices, as marked in lines 013,018 and 022 below (**Figure 4.3**).

4.1.2 Stadio Bay: Magnetic Gradiometry

The southern section (**Figure 4.4**) of the bay exhibits intense magnetic dipoles in the areas **M1**, **M2**, **M3**, **M4**. The values of the magnetic gradient in areas **M1** and **M3** are more than 50nT/m signifying the existence of ceramic concentration or the existence of a metal ferrous magnetic object. Anomalies **M2** and **M4** have weaker magnetic signal and could indicate an archaeological feature, perhaps a building, with poor preservation lever. The rectilinear anomaly **L1** with dimensions ~4x3m is also observed and could be related with the outline of an architectural structure. A complex of fade linear vertical segments **L2** having an E-W and N-S orientation outline another possible archaeological structure. The area **M4** is enclosed by sequence of linear segments (**L3**) that form the outline of a rectangular structure with dimensions 7.5x4.5m.

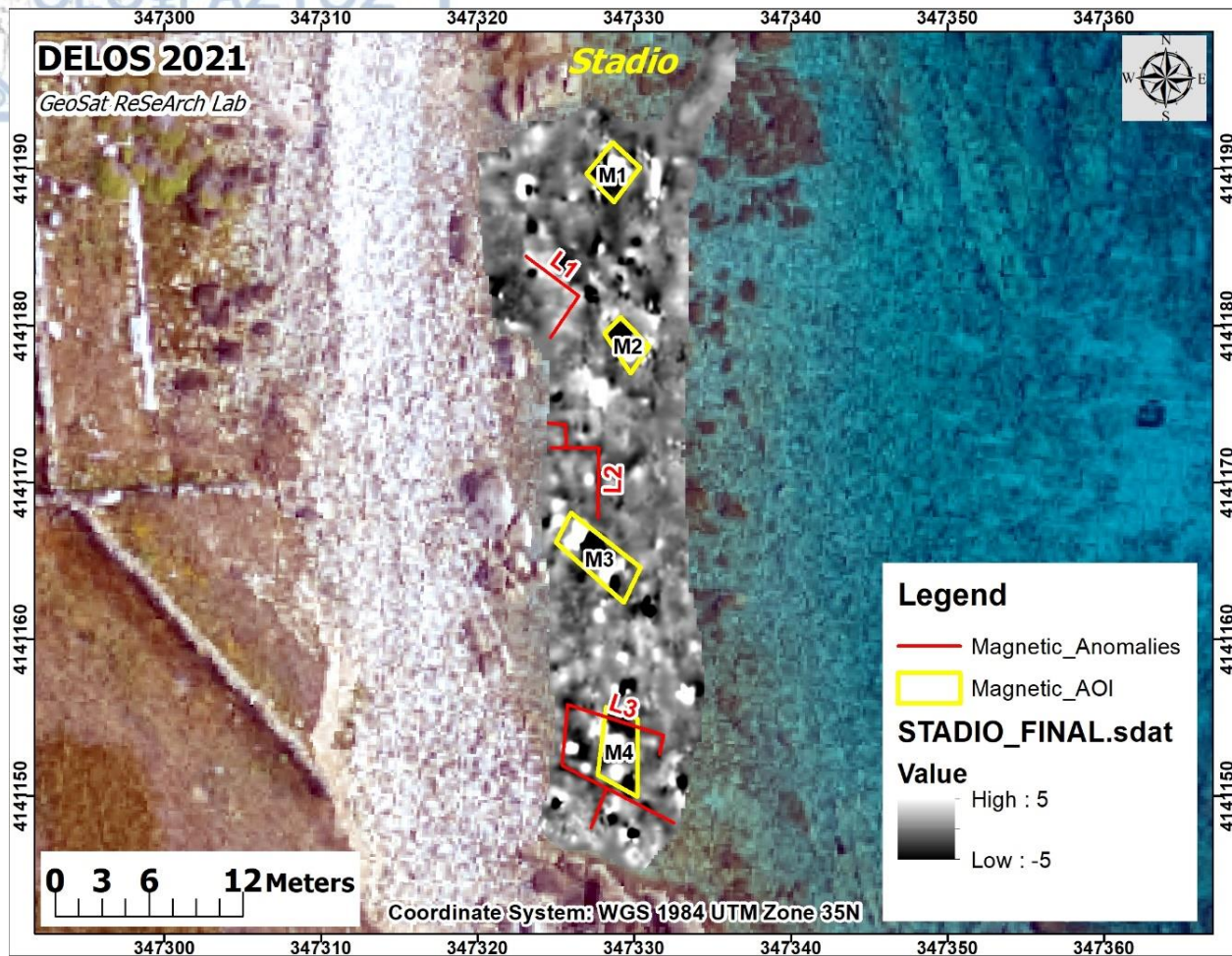


Figure 4.4: Diagrammatic interpretation of the magnetic anomalies at the southern section of Stadio Bay

The northern part (Σφάλμα! Το αρχείο προέλευσης της αναφοράς δεν βρέθηκε.) of the Stadio bay is occupied by relatively more disturbed magnetic signal in relation to the southern section. Despite the noise that was imposed by the rocky seabed, the magnetic map is rather revealing in identifying submerged anthropogenic structures. At the northern part two isolated linear segments (**L4**, **L5**) with NW-SE seem to have archaeological origin.

Towards the north, **L6** indicates remains of a rectangular structure with dimensions 11x4m that seems to be divided in different compartments with internal wall divisions. The area in **L7**, **L8** outlines rectilinear magnetic signatures showing the footprint of submerged structural remains. **L9** reveals a

small rectangular structure with dimensions 3x2.5m. Further to the south, the rectilinear features in **L10** probably belongs to the same general structural complex.

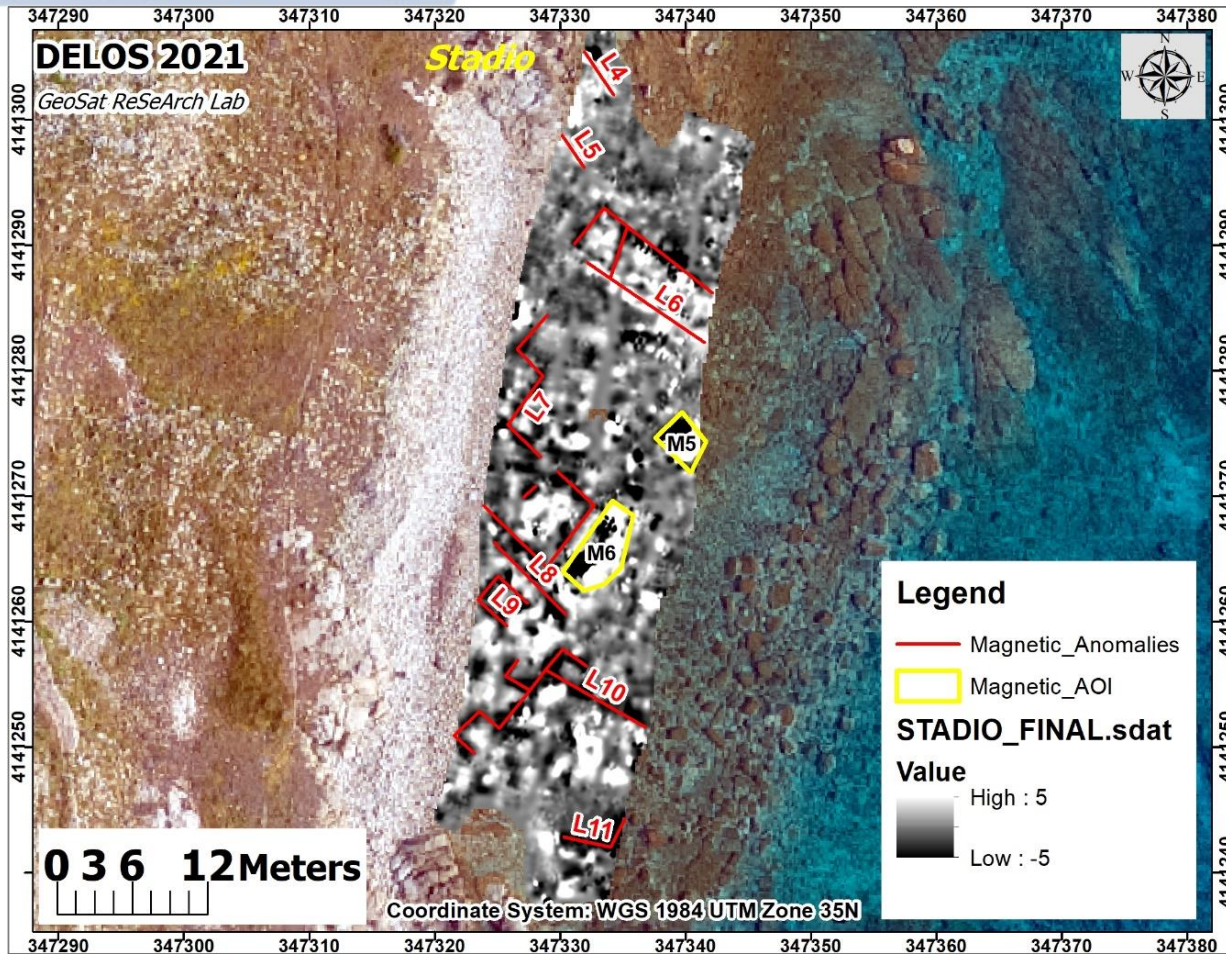


Figure 4.5: Diagrammatic interpretation of the magnetic anomalies at the northern section of Stadio Bay

The magnetic area **M5** exhibits very high values ($\sim 200\text{nT/m}$) indicating the identification of a localized metallic object. Magnetic area **M6** has lower values ($\sim 80\text{m}$) and is probably related to the structural element of **L8**. Finally, the rectilinear magnetic feature **L11** with dimensions 3.8x2.5m could indicate remains of an ancient wall. All the above magnetic features seem to follow the same general orientation along the NW-SE direction indicating that they probably belong to the same construction phase.



4.2 Ancient Olous Surveys Results Interpretation

4.2.1 Olous Bay Dynamic ERT

The depth slices from the respective 3D inversion model show a number of resistive regions with varying archaeological interest. The northeast corner is dominated by a resistive structure occupying area of 9x12 m, which is extending from the superficial layer up to a depth of ~2m below the sea bed. Based on the in situ inspection this area is related to a cluster of Posidonia sea plant, growing on beach rock.

In the northwestern corner, a large resistive anomaly can be seen. The structure occupies an area of 28x27 m can be seen from the most superficial layer up to the deepest depth slice of about 2m. This resistive anomaly corresponds to a reef, which was seen and documented in that specific location.

The most pronounced geophysical anomaly is outlined at the southern part of the surveyed area. All the depth slices show a compact resistivity region running the sea bottom along the east-west direction with a variable width ranging from 6m to 31m. This resistive feature is correlated to the trace of a submerged huge stone structure that either shows the direction of a fortress wall or the residues of the waterfront of a port.

The parts of the structure that are exposed and can be seen in the sea bed show a width ranging from 2m to 18m. Due to the use of geophysics, it is revealed that the buried structure is in fact much wider and combining the results of the 3D ERT with the documented visible structure a deduction can be made that the structure extends vertically across all of Olous Southern Bay. The structure can be seen in all of the depth slices, ranging from 0.2 m up to 2m below the sea bed.

Finally, two unknown targets of possible archaeological origins can be seen in **Figure 4.1**, **Figure 4.2** and **Figure 4.3**. The first target is located in the northern-eastern part of the grid and can be seen at all depths, with dimensions of 12x14m, while the second target appears in the western- central part of the grid and can be seen from the depth slice of about 1m to the depth slice of 2m, with dimensions of 16x13m. A careful in situ inspection was carried out on site after the conduction of the survey, but no clear evidence of geological or archaeological origin could be found, meaning that those two resistive structures are buried beneath the sea bed, with no surface appearance.

Figure 4.4 presents the interpreted depth slice of 2m. rectified in a map of the area, along with the measured GPS points of the sea wall marked as a shapefile.

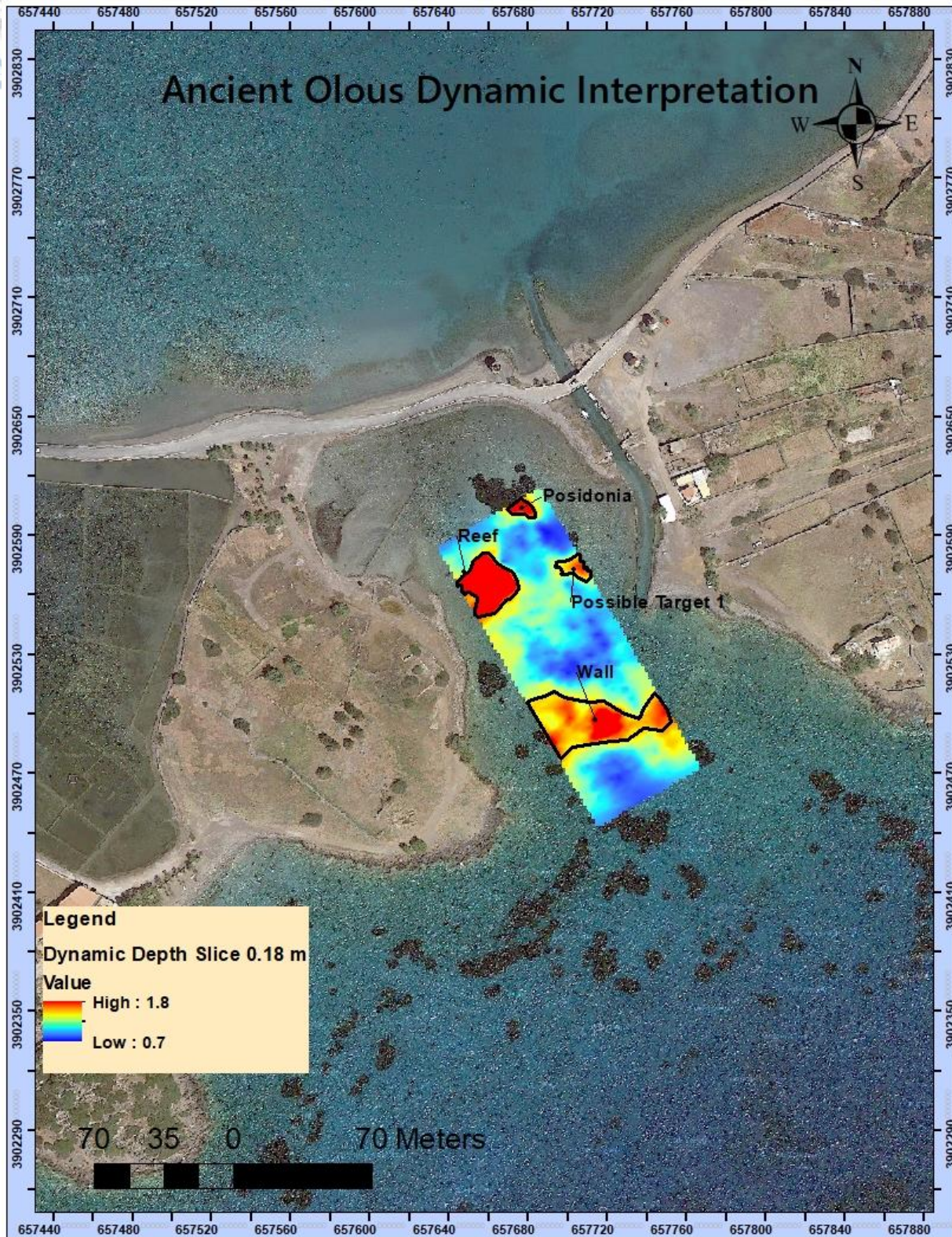


Figure 4.1: Diagrammatic Interpretation of the 3D inversion results of the Dynamic ERT method at the South bay of Ancient Olous at a depth of about 0.2 m

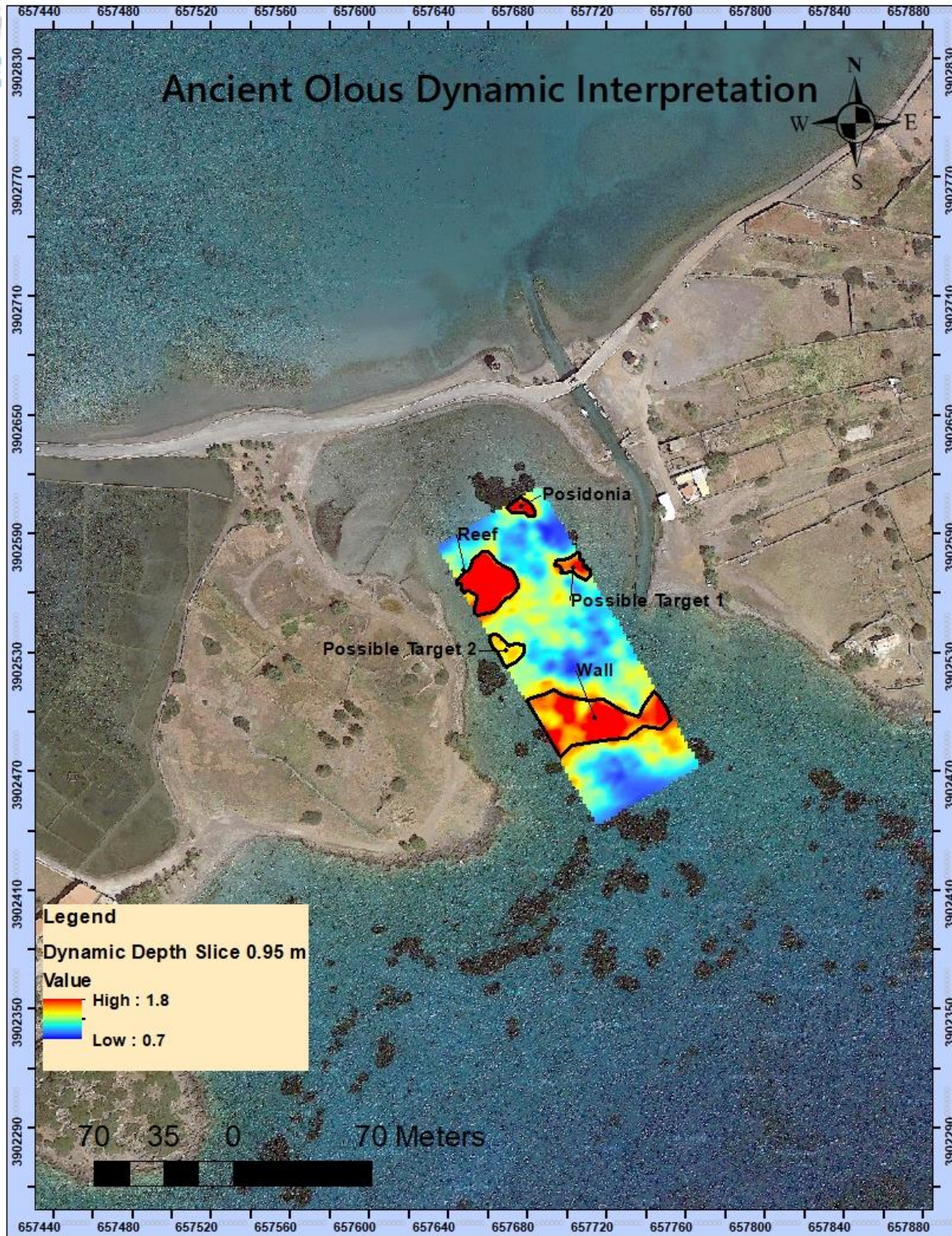


Figure 4.2: Diagrammatic Interpretation of the 3D inversion results of the Dynamic ERT method at the South bay of Ancient Olous at a depth of about 1 m

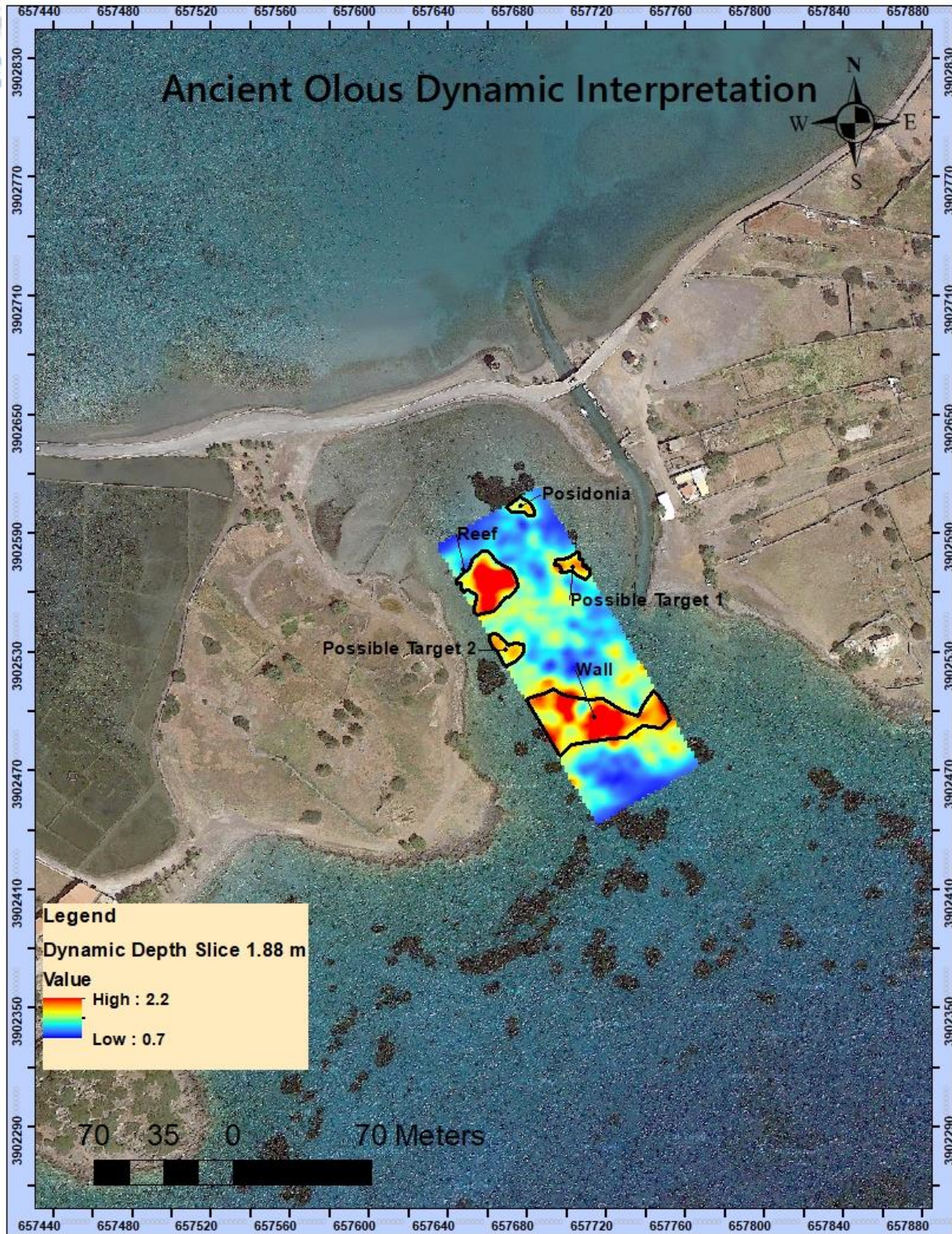


Figure 4.3: Diagrammatic Interpretation of the 3D inversion results of the Dynamic ERT method at the South bay of Ancient Olous at a depth of about 2 m

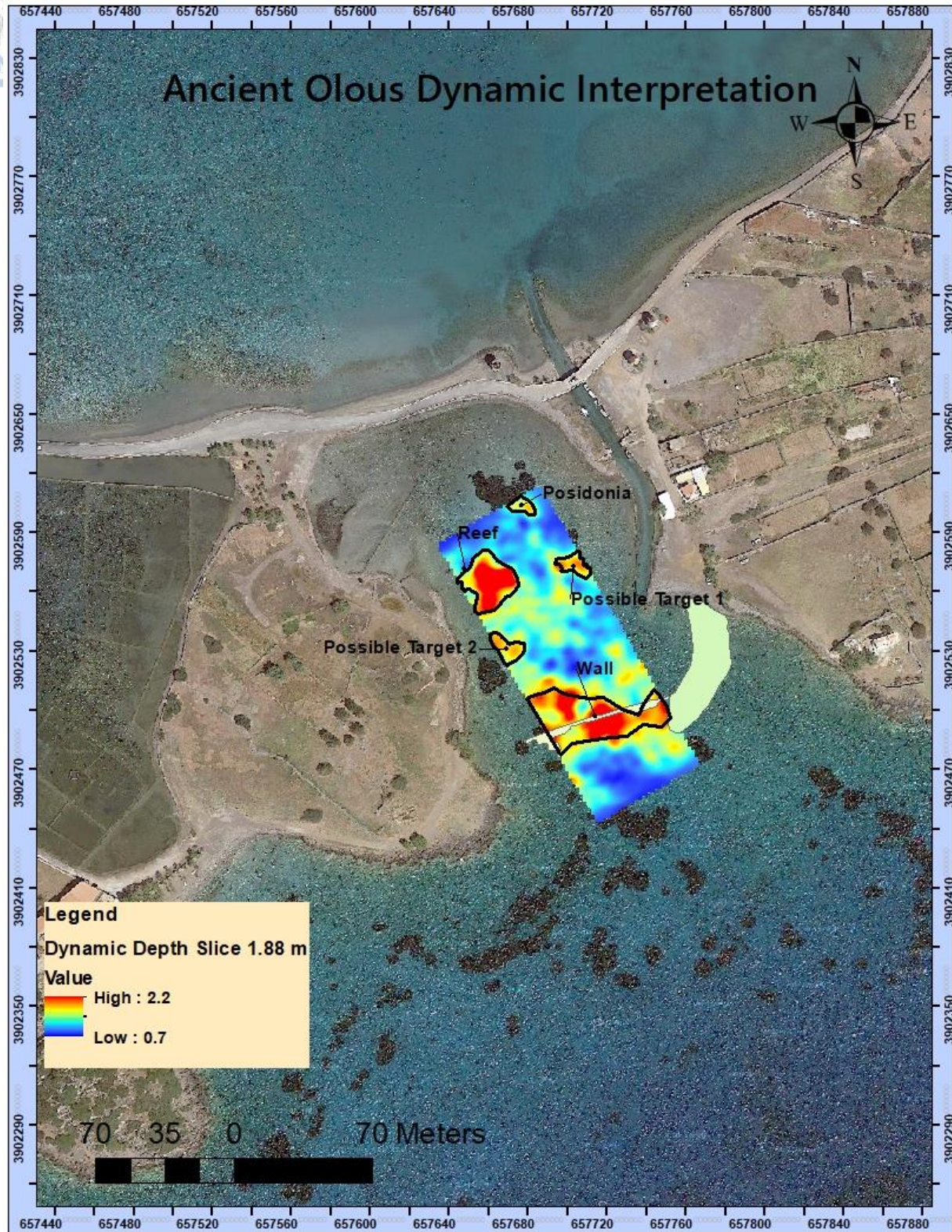
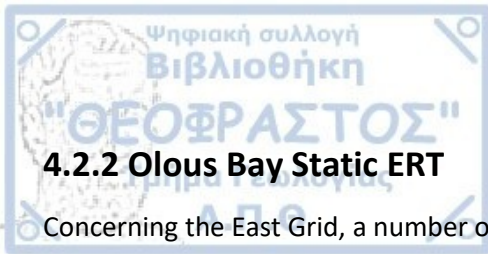


Figure 4.4: Diagrammatic Interpretation of the 3D inversion results of the Dynamic ERT method at the South bay of Ancient Olous at a depth of about 2 m with the rectification of the sea Wall



4.2.2 Olous Bay Static ERT

Concerning the East Grid, a number of resistive anomalies were detected in the southern half of the grid. Those anomalies appear in a parallel and vertical direction to each other, so it is highly possible that they belong to remnants of an anthropogenic building complex. The resistive anomalies are marked with lines in **Figure 4.5** and **Figure 4.6**. Another anomaly appears in the northern half of the grid, marked with a circle which is related to a geological feature of the area, possibly beach rock since it appears in continuously in all respective depth slices up to a depth of more than 2m below the sea bed.

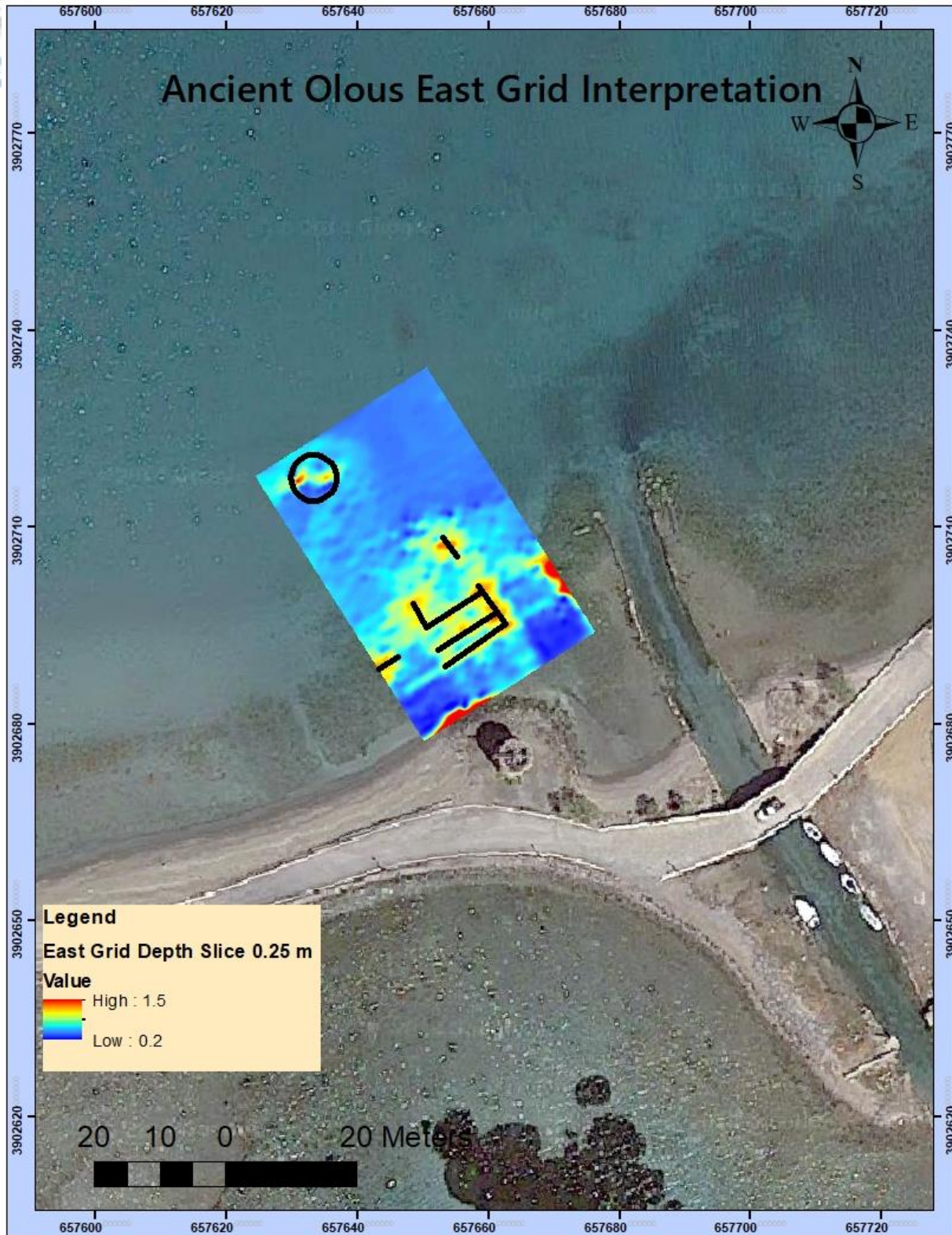


Figure 4.5: Diagrammatic Interpretation of the 3D inversion results at the East Grid of Ancient Olous at a depth of about 0.25 m below the sea bed

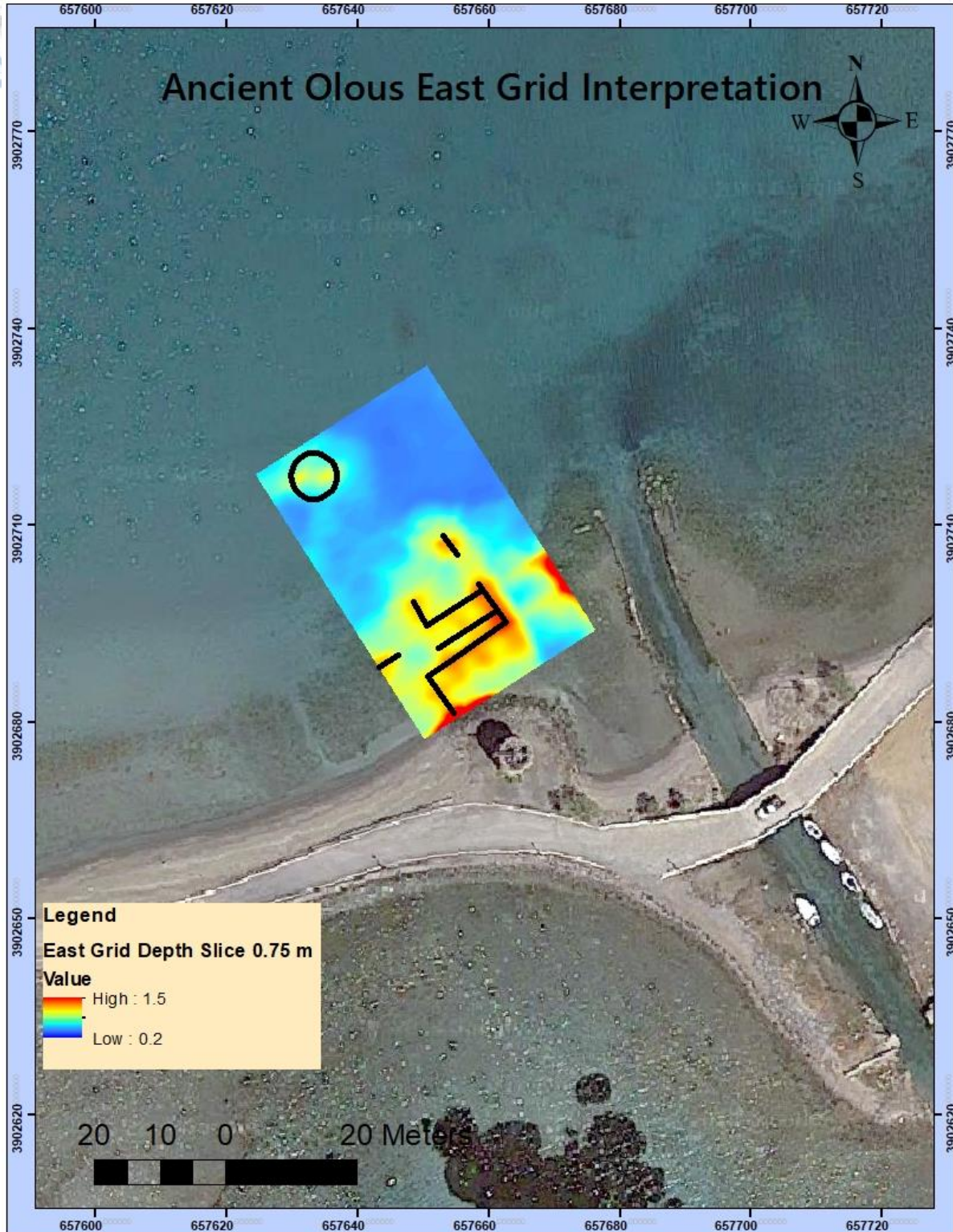


Figure 4.6: Diagrammatic Interpretation of the 3D inversion results at the East Grid of Ancient Olous at a depth of about 0.75 m below the sea bed



Concerning the West grid, two resistive anomalies appear at the southern part of the grid parallel to each other, that are most probable related to archaeological targets. The group of anomalies forming a square further to the north seem to belong to a submerged building construction with dimensions of 5x5m. Another group of anomalies appear next to the square, forming what appears to be part of another building or room. It must be noted that remnants of a building or wall were identified and documented in the area of those anomalies. Finally, the northern linear resistive anomaly correlates with the footprint of the beach rock that was mapped during the field measurements with in situ diving (*Figure 4.7, Figure 4.8*).



Figure 4.7: Diagrammatic Interpretation of the 3D inversion results at the West Grid of Ancient Olous at a depth of 0.25 m below the sea bed.



Figure 4.8: Diagrammatic Interpretation of the 3D inversion results at the West Grid of Ancient Olous at a depth of 0.75 m below the sea bed.



Chapter 5– Conclusions

In this chapter, an overview of the work described above will be presented. Some general conclusions and remarks will be drawn, and finally some suggestions for future endeavors and research will be made.

Overall, Electrical Resistivity Tomography (ERT) and magnetic gradiometry geophysical methods presented in this thesis were successfully used to primarily provide crucial information about the buried anthropogenic structures in the littoral areas of investigation, and secondarily information about the geological background of those areas.

Specifically, the Skhardanas Dynamic ERT survey achieved to pinpoint many archaeological structures in the shallower parts of the bay with the utilization of the ultra-shallow lines and draw the general geological profile of the deeper parts of the bay. This is not a small feat, considering the difficulties presented by the terrain and the weather. The dynamic ERT survey in both the ultra-shallow and the deeper part of the bay managed to reconstruct the resistivity model below the seabed enhancing the information context regarding the archaeological structures and the general geological setting of the bay. From the technical point of view the in situ difficulties imposed by the rocky sea bottom added extra difficulties in collecting high quality data. More specifically the thickness of the graphite electrodes of the marine cable used in the survey made harder the smooth movement of the cable on the sea bottom since it was occasionally getting stuck at the sharp rocks. Thus such kind of multimode cable seemed to be unsuitable for a survey in such a rocky area.

The Multisensor Magnetic Gradiometry applied in the Stadio Bay of Delos managed to detect a number magnetic anomalies and areas of investigation related to anthropogenic structures verifying visible structures and outlining at the same time completely new buried below the sea bottom. The importance of this survey is dual, based on the introduction for the first time of a fully underwater multisensor gradiometry instrumentation to map the magnetic properties below the sea bed in rocky ultra shallow marine area.

Concerning the Static ERT survey performed in the North Bay of ancient Olous, the results on both grids were deemed very satisfactory, since they managed to uncover an unknown building complex and to verify the existence of a beach rock formation.



Finally, the dynamic ERT survey in the south bay of ancient Olous also presented more than satisfactory results. This survey in particular, proved that both the data collection as well as the inversion techniques used during the processing were right on mark, as it is considered very difficult to produce a fully 3D inverted model of the substratum in a dynamic survey, let alone pinpoint an already known fortress wall expanding our knowledge on the actual horizontal and vertical expansion and two unseen possibly archaeological targets.

All in all, underwater areas of archaeological interest are and must be considered as endangered and threatened by more aggressive agents than their dry land counterparts. The continuous rise of the sea level in a global scale, as well as the tectonic regime of each region, water salinity, wave exposure, sea currents, algae related erosion and sand movements are only few of those agents. On the other hand, due to their unapproachable location on the sea bed, they are naturally protected from the diachronic actions of vandals and looters.

However, the unapproachable nature of those areas, not only protects them, but also obscures them from the eyes of the scientific community willing to research them, as well as from the local residents who are sometimes unaware of the cultural wealth hidden near them.

Keeping the facts mentioned above in mind, this thesis presented how the employment of geophysical methods can extend from terrestrial to shallow marine environments. This transition leads to completely different environmental conditions resulting in new challenges for the application of the corresponding methodologies.

Taking all of the above into consideration, the following deductions can be made:

- a) The distinct conditions and challenges posed by the shallow marine environment as well as the chronic lack of funding for research, explains why geophysical applications for the solving of archaeological problems in such areas started to be utilized very recently. The results of this thesis prove that marine geophysics can be accurately used for solving such problems. However, more research and testing is required in order for the methods to reach their full potential. Further polishing the existing techniques and their protocols, adapting the methodological flowcharts and even establishing new techniques will lead to a decrease in the data collection time and to an increase to the collected data quality, and overall maximize the accessibility of information regarding the current state of submerged archaeological sites.



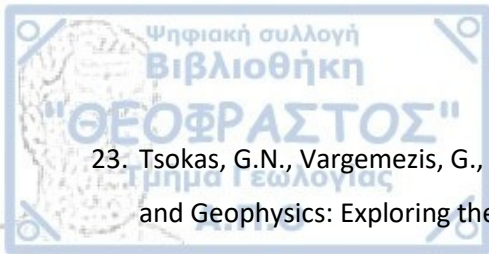
- b) The approval of marine geophysics as a toolset suitable for littoral archaeological investigations by the scientific community in general and by the archaeologists in specific, will eventually lead to the creation of a fully tested series of procedures that will be used in many other similar shallow offshore environments. This in turn will establish the branch of marine geophysics in archaeological surveys, giving underwater archaeology a new set of tools for approaching coastal zones more globally, easily combining the results of underwater surveys with the results of land archaeological sites. Finally, this will contribute to the upgrade of geophysical methods both in theoretical and in practical levels, help the marine archaeology branch further increase its influence and effectiveness and in overall enrich the knowledge in the wider fields of science and human studies.
- c) All the above, can help bring the wider public more in contact with the coastal and marine archaeological sites in Greece and in a global scale. Sharing the information about those submerged sites with local communities will contribute to ensuring their protection, as well as play a role in the community's overall education. Naturally, this whole process will also open many opportunities for financial activities, motivating the development of such areas to visitable sites and upgrading those regions both economically as well as culturally.



1. Aguila, J.F., McDonnell, M.C., Flynn, R., Hamill, G.A., Ruffell, A., Benner, E.M., Etsias, G., Donohue, S. Characterizing groundwater salinity patterns in a coastal sand aquifer at Magilligan, Northern Ireland, using geophysical and geotechnical methods. *Environmental Earth Sciences*, 81:231, 2022.
2. Bruneau, P., Ducat, J., Brunet, M., Farnoux, A., Moretti, J.C. *Guide of Delos*. Athens and Paris Ecole française d' Athenes and Editions de Boccard, 2010.
3. Combes, V., Eglinger, A., Andre-Mayer, A.S., Teitler, Y., Jessell, M., Zeh, A., Reisberg, L., Heuret, A., Gibert, P. Integrated geological-geophysical investigation of gold-hosting Rhyacian intrusions (Yaou, French Guiana) from deposit-to district-scale. *Journal of South American Earth Sciences*, 114, 103708, 2022.
4. Farquharson, C.G., Oldenburg, D.W. Non-linear inversion using general measures of data misfit and model structure. *Geophys. J. Int.* 134, 213-227, 1998
5. Fox, R.C., Hohmann, G.W., Killpack, T.J., Rijo, L. Topographic effects in resistivity and induced-polarization surveys. *Geophysics*, 45, 1, 1980.
6. Fukuyo, N., Clark, G., Purcell, A., Parton, Ph., Yokoyama, Y. Holocene sea level reconstruction using lagoon specific local marine reservoir effect and geophysical modeling in Tongatapu, Kingdom of Tonga. *Quaternary Science Reviews*, 244, 106464, 2020.
7. Gaffney, C., *Detecting Trends in the Prediction of the Buried Past: A Review of Geophysical Techniques in Archaeology*. *Archaeometry*, 50, 313-336, 2008.
8. Georgiou, N., Dimas, X., Fakiris, E., Christodoulou, D., Geraga, M., Koutsoumpa, D., Baika, K., Kalamara, P., Ferentinos, G., Papatheodorou, G. A Multidisciplinary Approach for the Mapping, Automatic Detection and Morphometric Analysis of Ancient Submerged Coastal Installations: The Case Study of the Ancient Aegina Harbour Complex. *Remote Sensing*, 13, 4462, 2021.
9. Linford, N. The application of geophysical methods to archaeological prospection. *Reports on Progress in Physics*, 69, 2205-2257, 2006.
10. Mourtzas, N.D. A palaeogeographic reconstruction of the seafront of the ancient city of Delos in relation to Upper Holocene sea level changes in the central Cyclades. *Quaternary International*, 1-16, 2011.



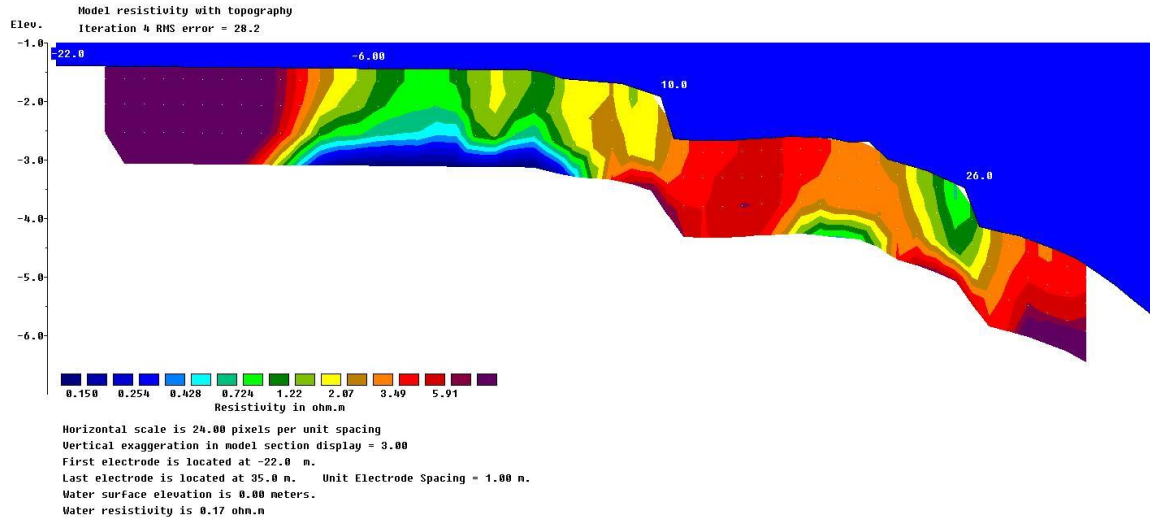
11. Onaca, A., Gachev, E., Ardelean, F., Ardelean, A., Persoiu, A., Hegyi, A. Small is strong: Post – Lia resilience of Europe’s Southernmost glaciers assessed by geophysical methods. *CATENA*, 213, 106143, 2022.
12. Orfanos, C., Leontarakis, K., Apostolopoulos, G. Surface wave tomography using active sources in engineering applications: A 3D experiment at a test site of known conditions. *Journal of Applied Geophysics*, 200, 104617, 2022.
13. Osorio-Granada, A.M., Jigena-Antelo, B., Vidal Perez, J.M., Hernandez-Pardo, O., Leon-Rincon, H., Munoz-Perez, J.J. Potential fields modeling for the Cayos Basin (Western Caribbean Plate): Implications in basin crustal structure. *Marine Geology*, 449, 106819, 2022.
14. Pacheco-Ruiz, R., Adams, J., Pedrotti, F., Grant, M., Holmlund, J., Bailey, C. Deep sea archaeological survey in the Black Sea – Robotic documentation of 2,500 years of human seafaring. *Deep-Sea Research Part I*, 152, 103087, 2019.
15. Papadopoulos, N. Shallow Offshore Geophysical Prospection of Archaeological Sites in Eastern Mediterranean. *Remote Sensing*, 13, 1237, 2021.
16. Papadopoulos, N., Oikonomou, D., Cantoro, G., Simyrdanis, K., Beck, J. Archaeological prospection in ultra-shallow aquatic environments: the case of the prehistoric submerged site of Lambayanna, Greece. *Near Surface Geophysics*, 19, 677-697, 2021.
17. Papazachos, V. Introduction in Applied Geophysics, 1996 (in Greek).
18. Renkewitz, H, Matz, S., Thomas, S., Schwendner, J., Albiez, J. Evaluation of high-end laserscanner for underwater archaeology. *OCEANS 2021: San- Diego – Porto*, 2021 .
19. Schwardt, M., Wilken, D., Rabbel, W. Attenuation of Seismic Multiples in Very Shallow Water: An Application in Archaeological Prospection Using Data Driven Approaches. *Remote Sensing*, 13, 1871, 2021.
20. Sharma, S., Thakur, S., Sharma, T. Application of Geophysical Methods in Tunnel and Oil Exploration. *IOP Conference Series: Earth and Environmental Science*, 889, 012015, 2021.
21. Simyrdanis, K., Papadopoulos, Cantoro, G. Shallow Off-Shore Archaeological Prospection with 3-D Electrical Resistivity Tomography: The Case of Olous (Modern Elounda), Greece. *Remote Sensing*, 8, 897, 2016.
22. Theodoulou, Th., Tourtas, A. Searching for Ancient Olous in the sea bottom and in the shores of Elounda (2017-2021). *DIATOPO: Diachronic Landscapes of Cretan Civilization, Featuring the sea and mountain wealth of Mirabello*, 31-50, 2022 (in Greek).



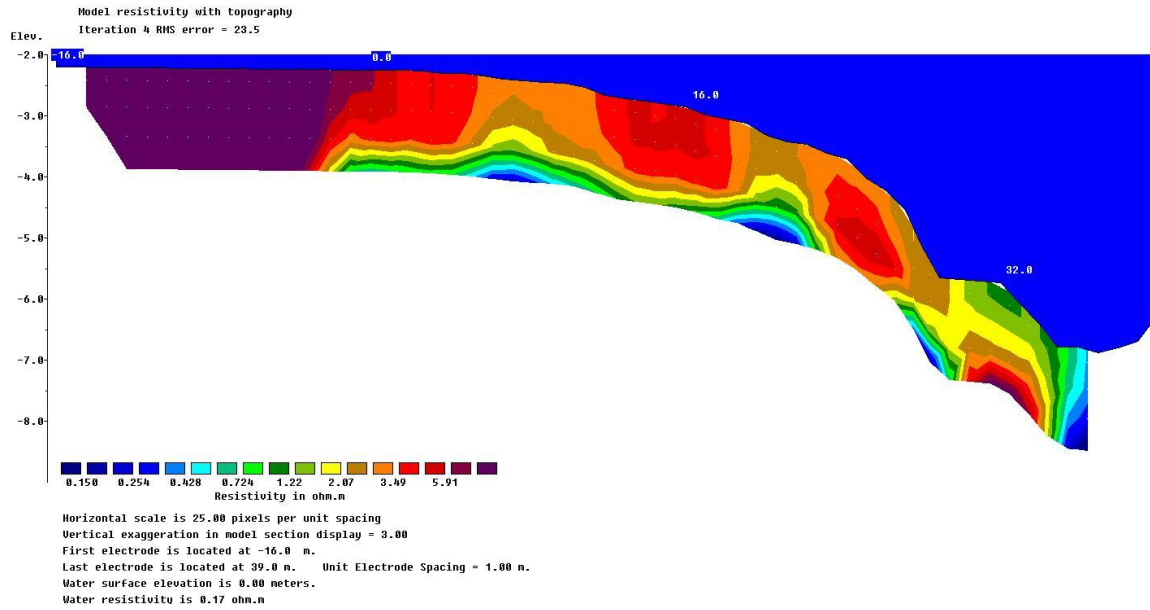
23. Tsokas, G.N., Vargemezis, G., Tsourlos, P., Drougou, S., Saatsoglou-Paliadeli, Ch. Archaeology and Geophysics: Exploring the Archaeological Site of Vergina (1984-2004), 2006 (in greek).
24. Tsourlos, P. Modelling, Interpretation and Inversion of Multielectrode Resistivity Survey Data. D.Phil. Thesis, University of York, 1995.
25. Zarmakoupi, M. Hellenistic and Roman Delos: the city and its emporion, Archaeological Reports, 61, 115-132, 2015.

Appendix A – Results of 2D Inversion of the Skhardanas Data Set

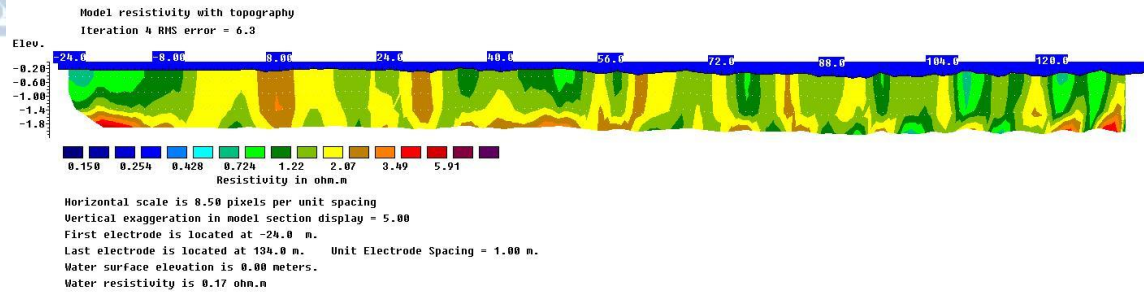
001.bin



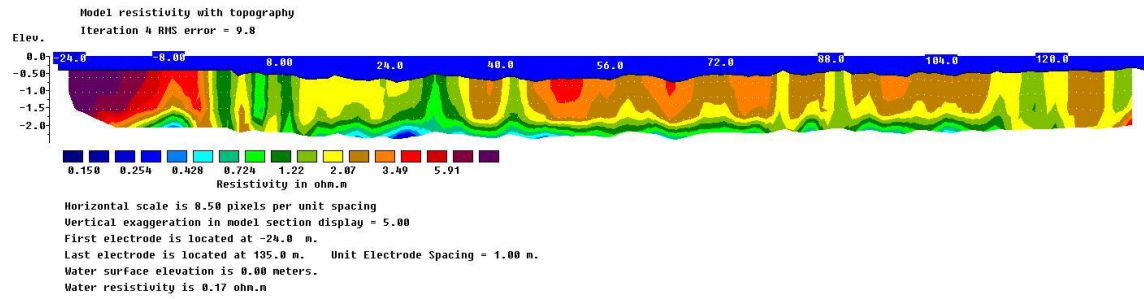
002.bin



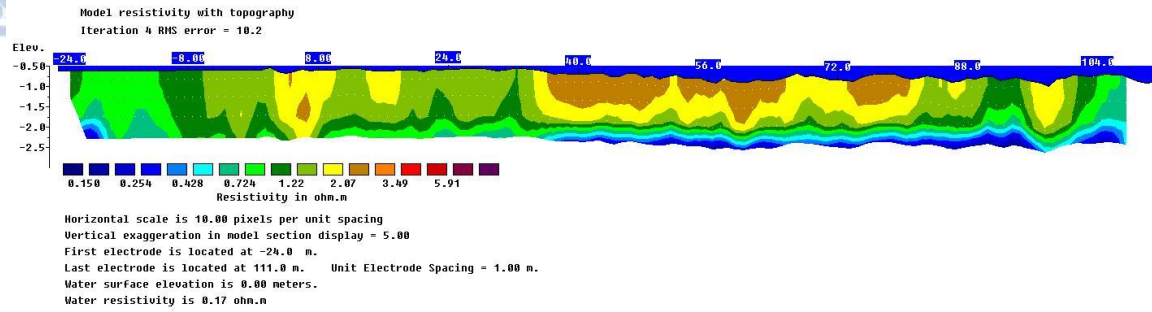
003.bin



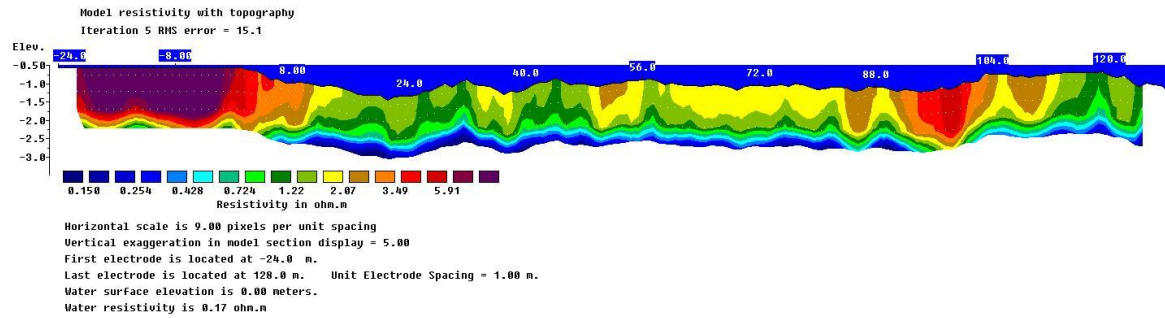
004.bin



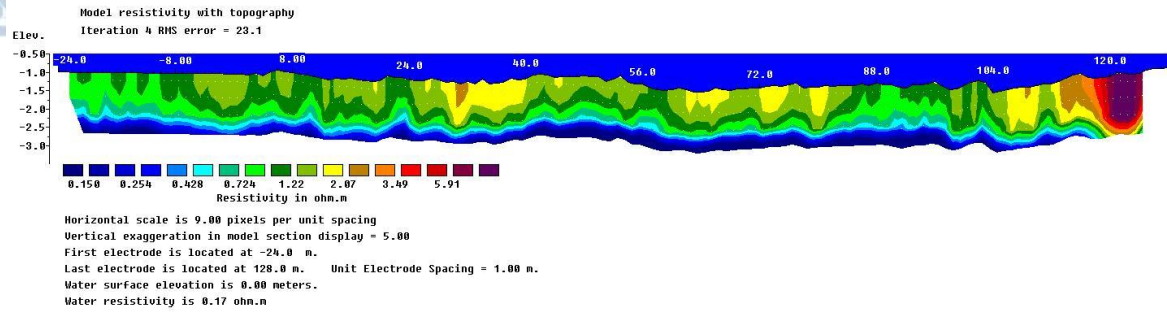
005.bin



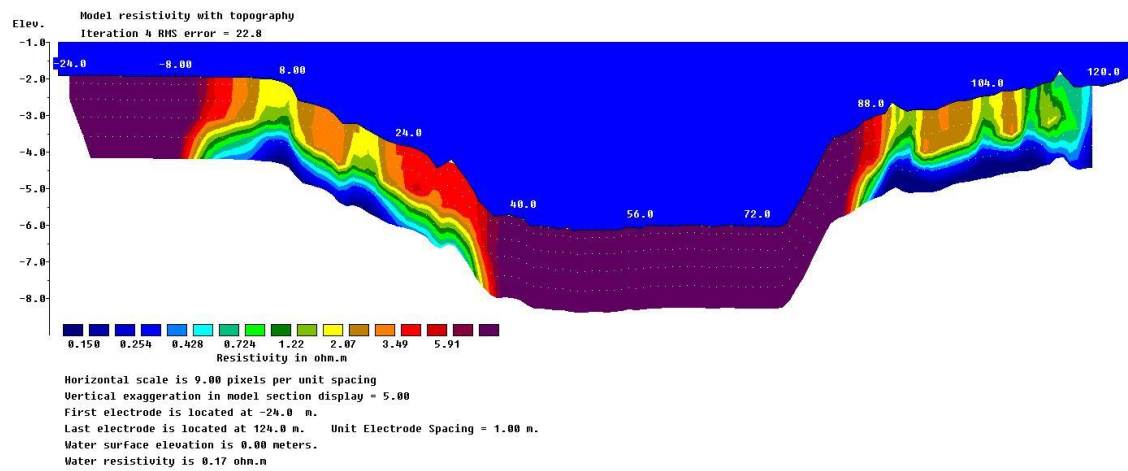
006.bin



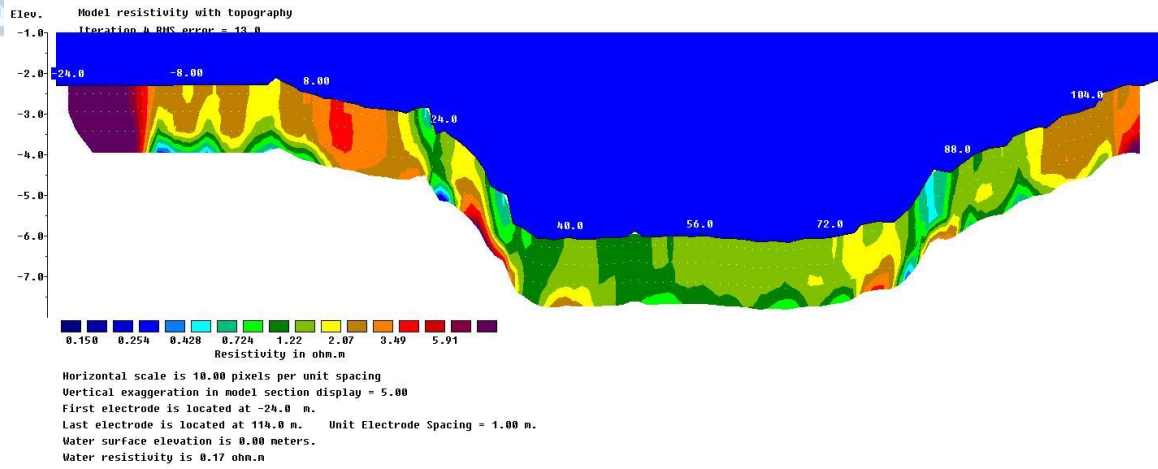
007.bin



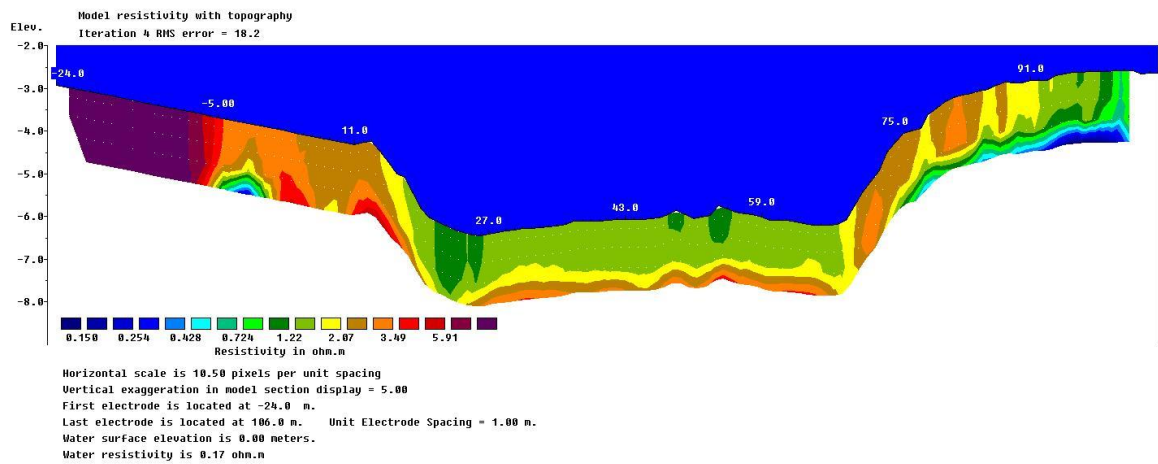
008.bin



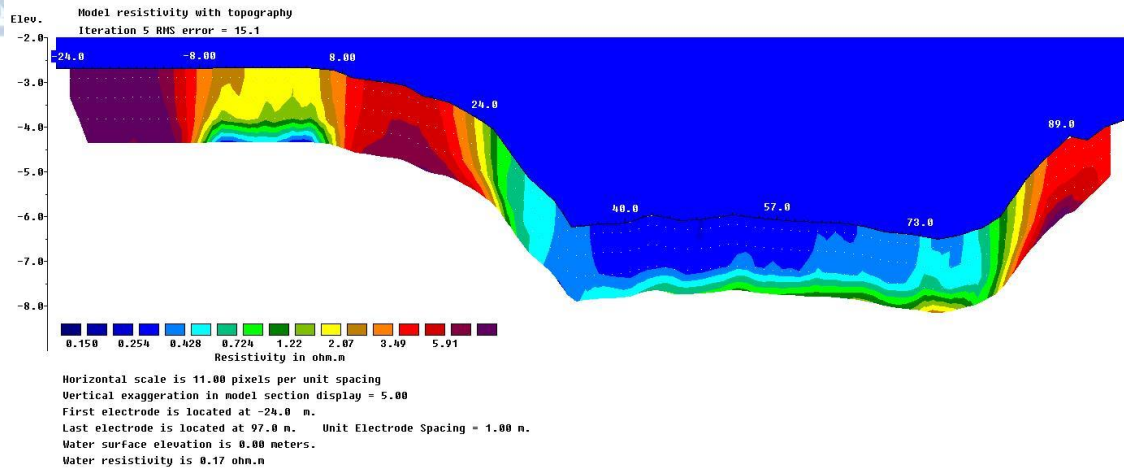
009.bin



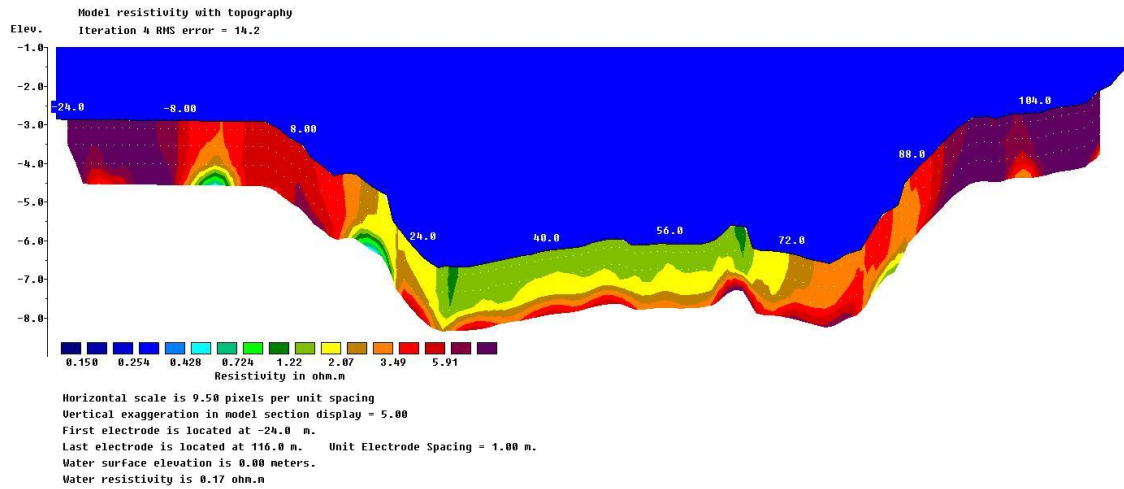
010.bin



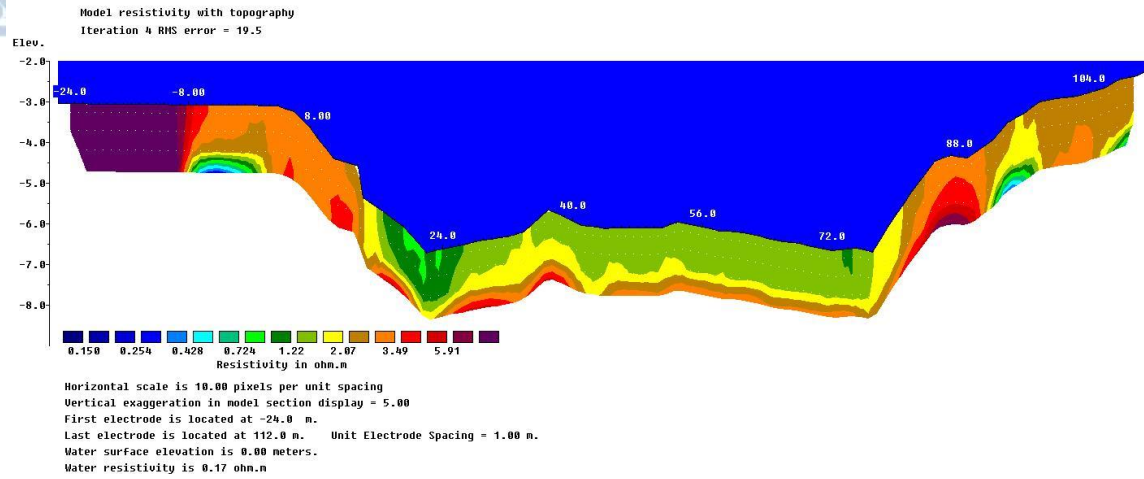
011.bin



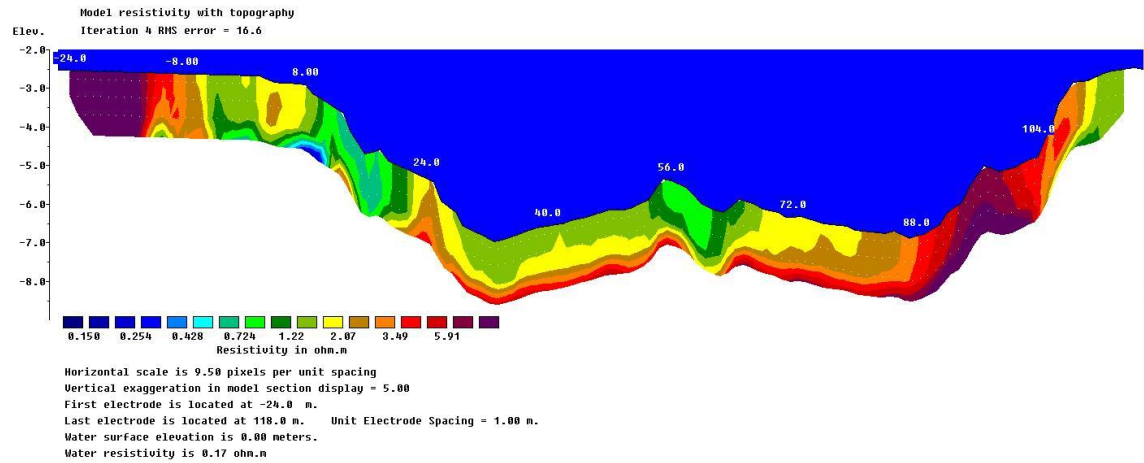
012.bin



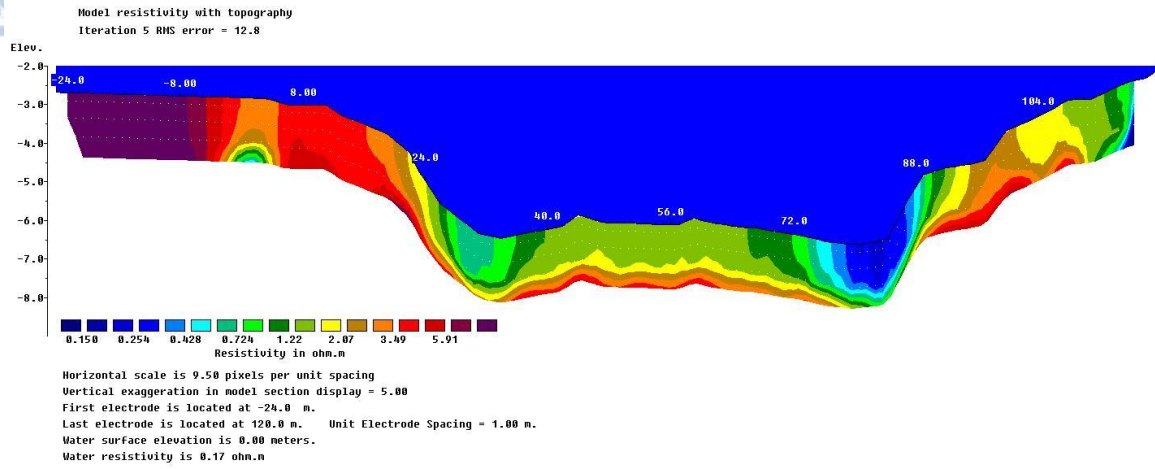
013.bin



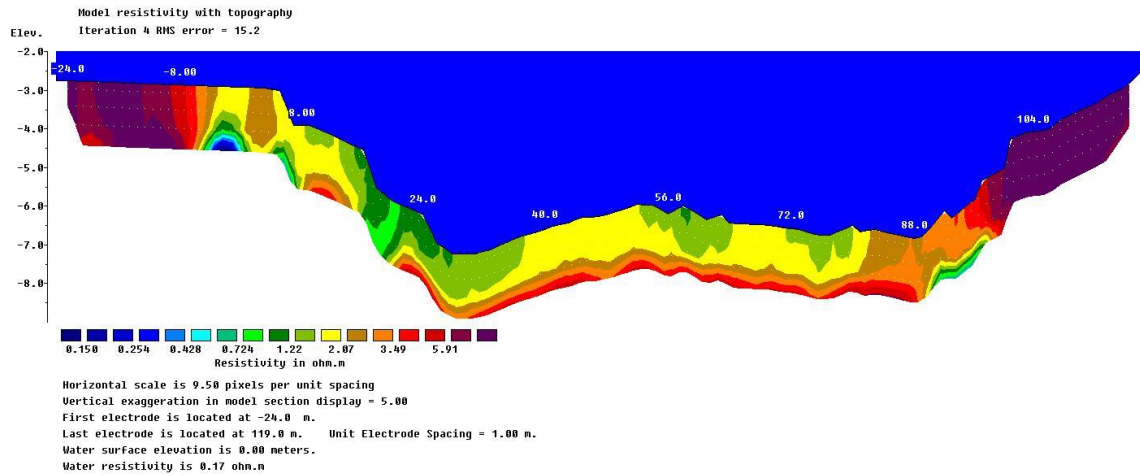
014.bin



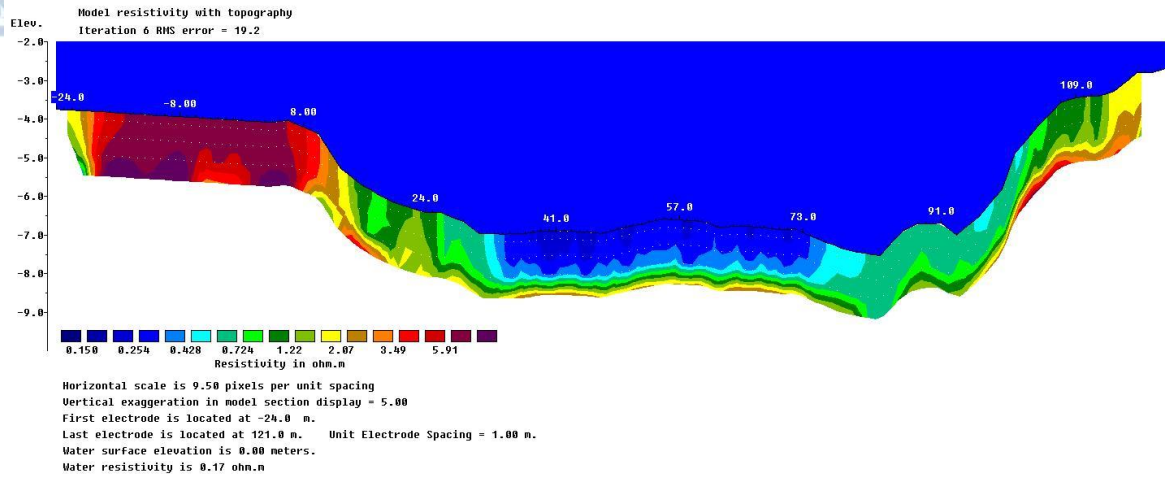
015.bin



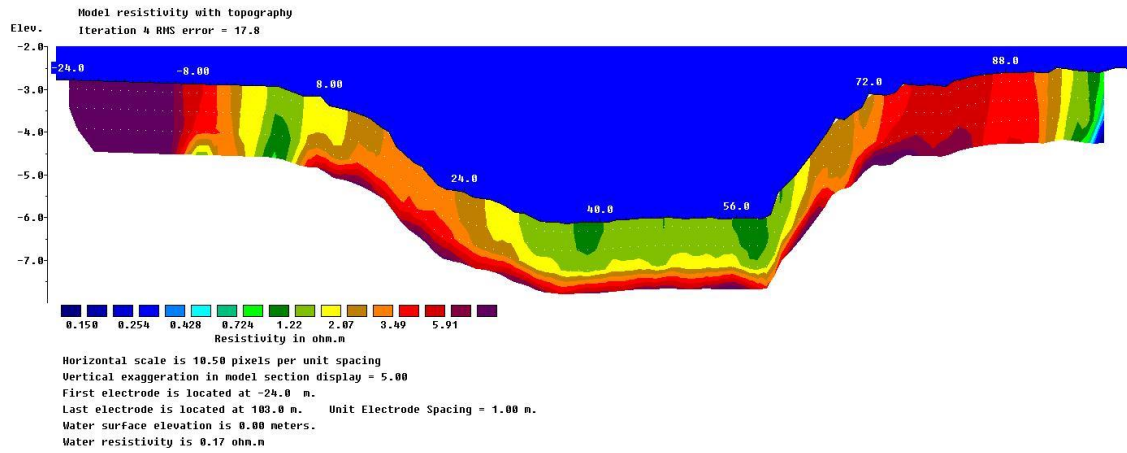
016.bin



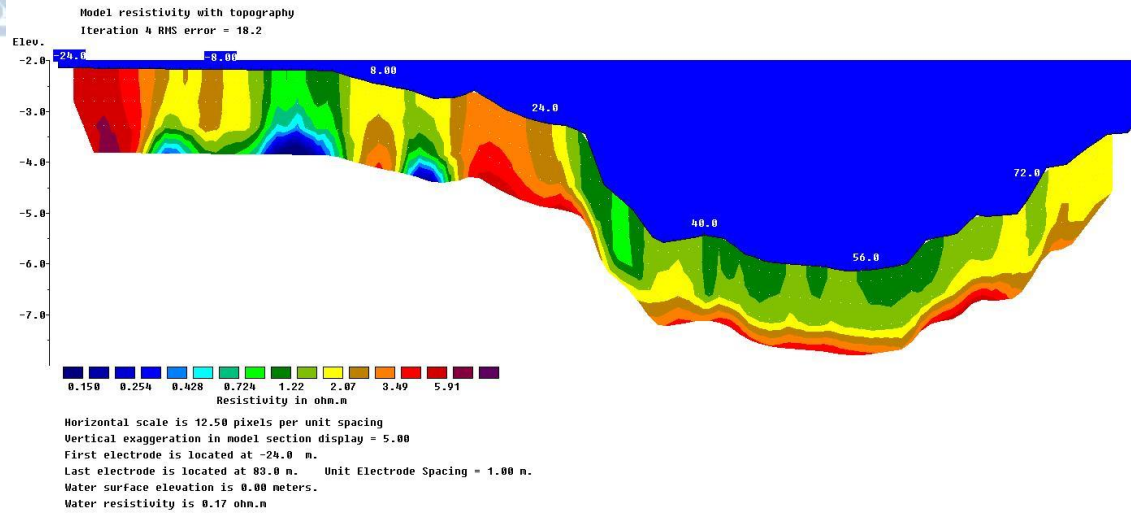
018.bin



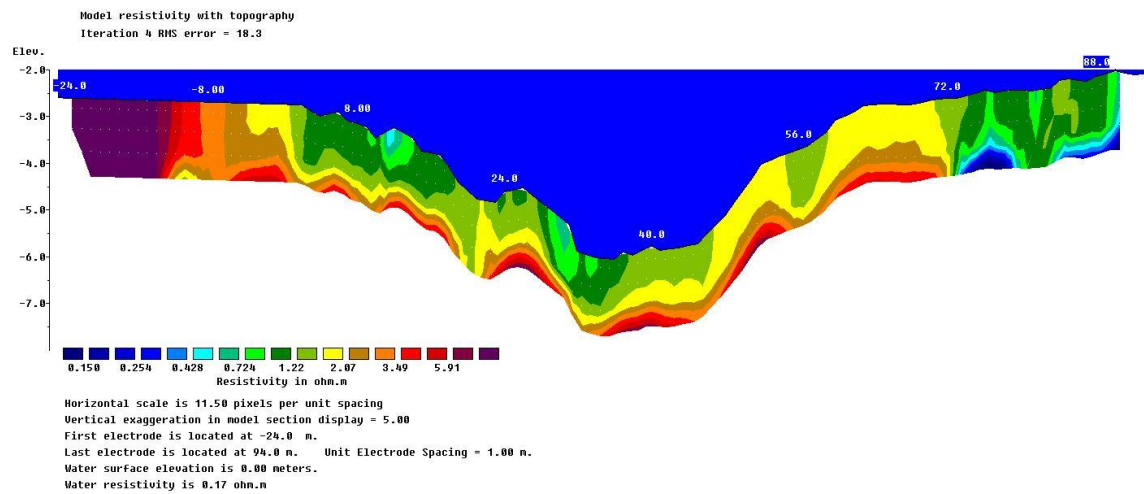
020.bin



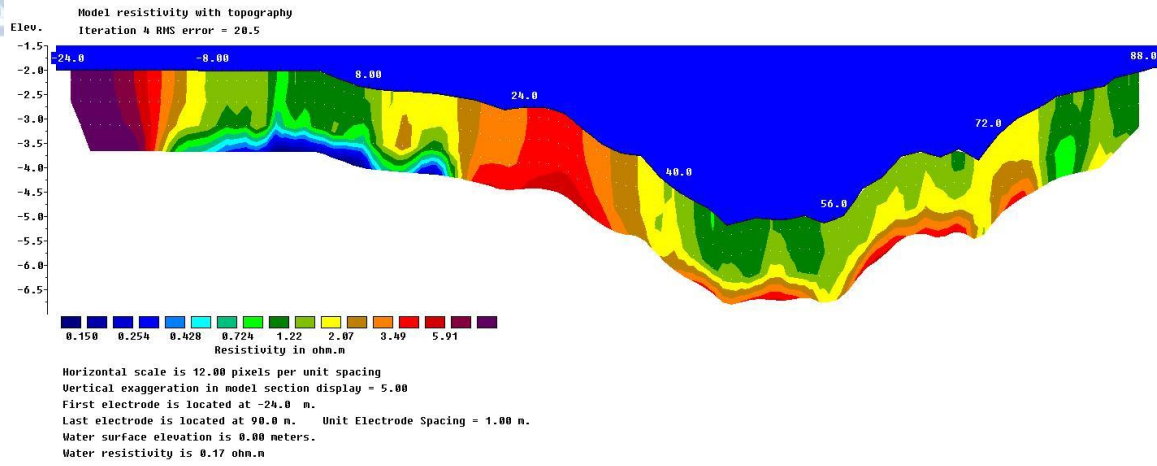
021.bin



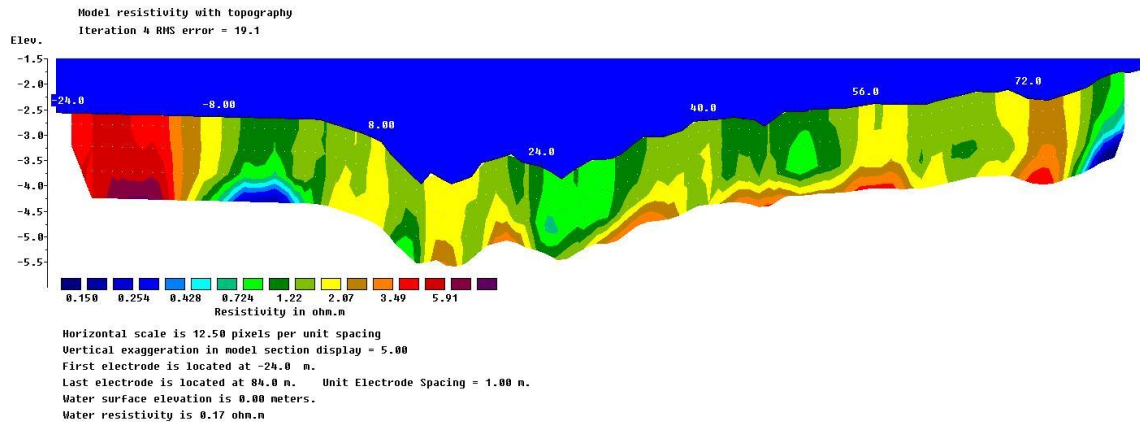
022.bin



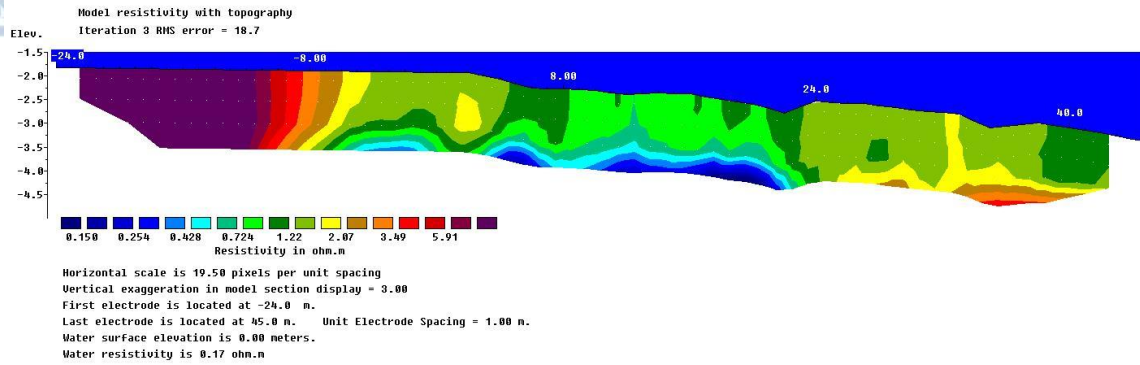
023.bin



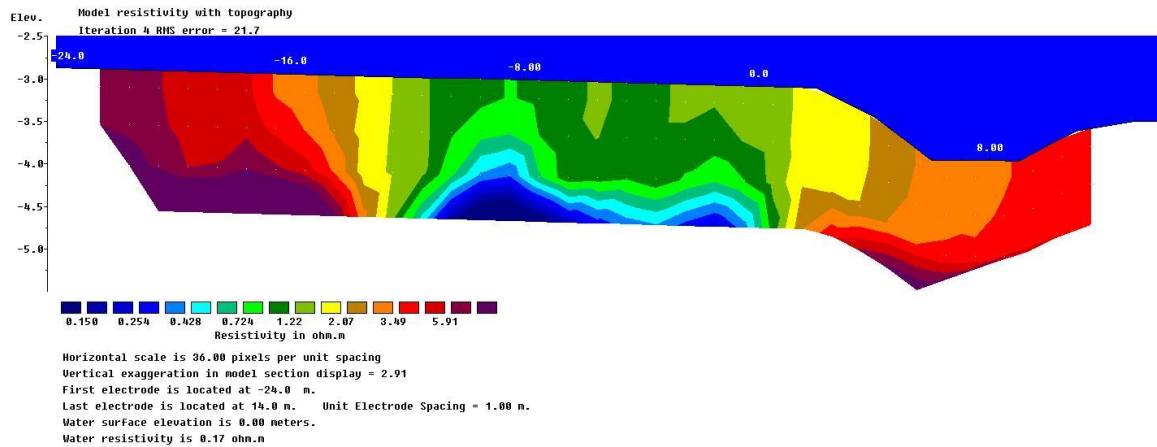
026.bin



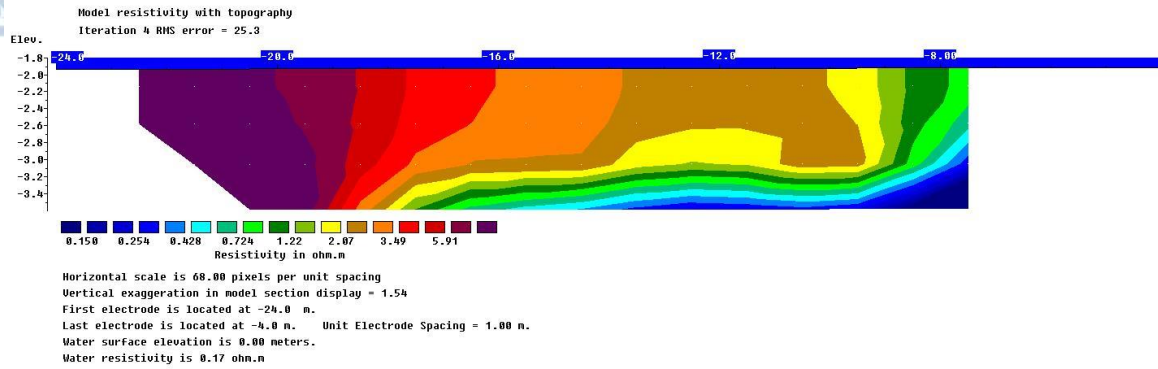
027.bin



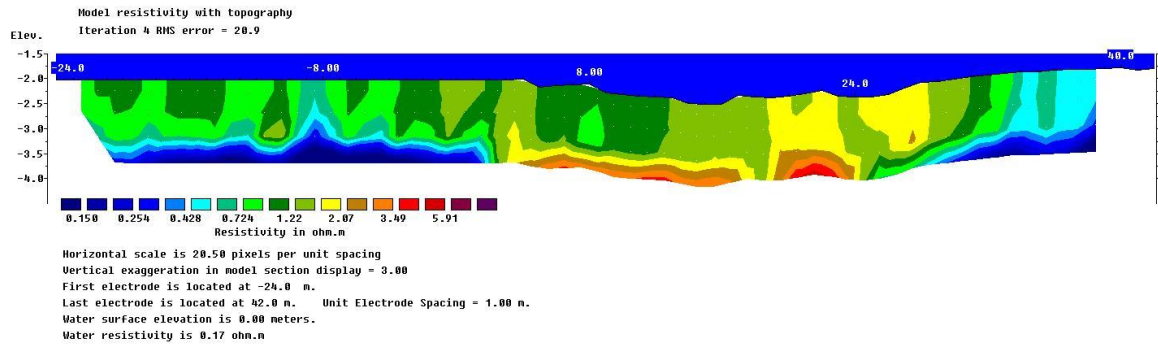
029.bin



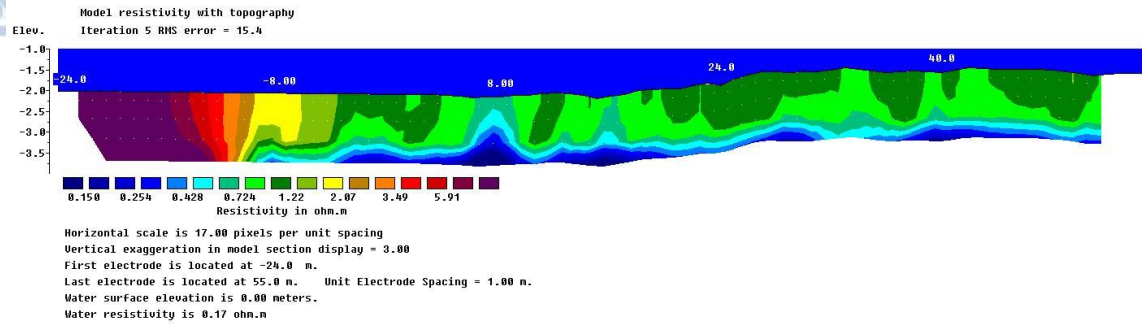
030.bin



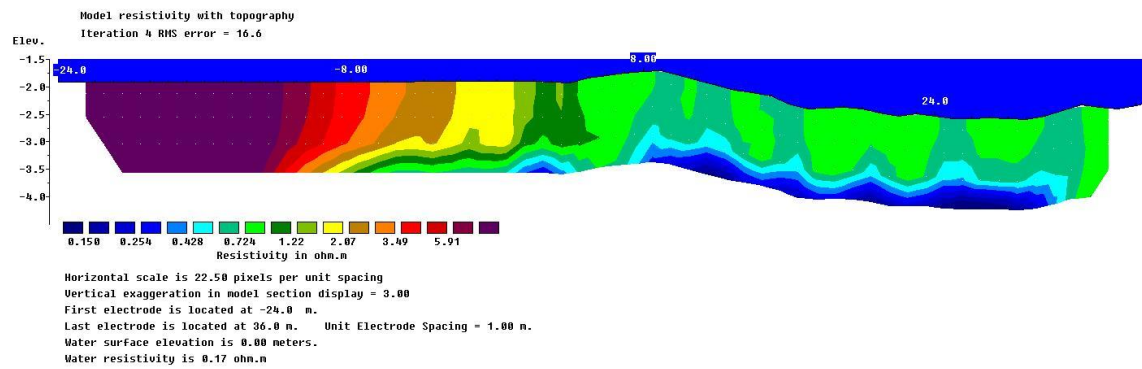
032.bin



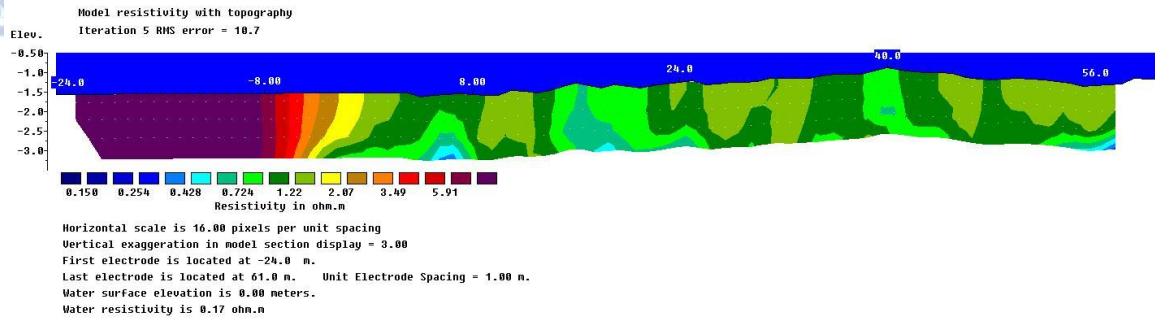
033.bin



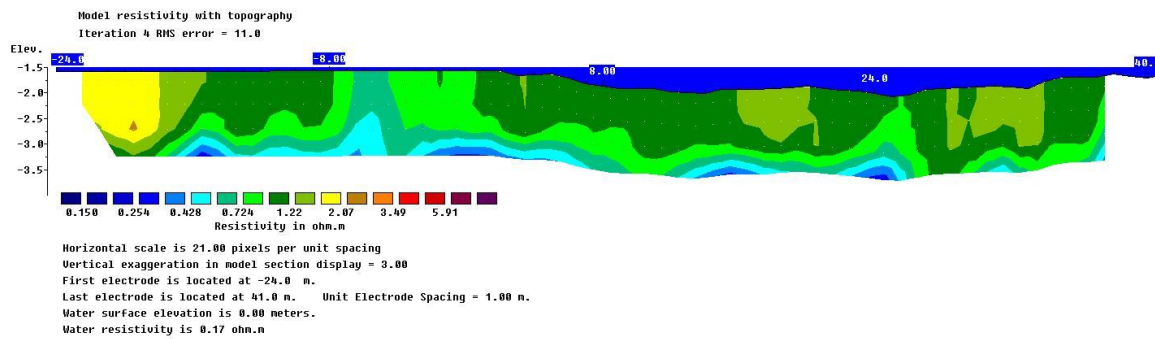
034.bin



036.bin



037.bin





Appendix B – Inversion parameters

1) Skhardanas and Static Olous data sets Inversion Parameters

Inversion settings

Initial damping factor (0.01 to 1.00)

0.1500

Minimum damping factor (0.001 to 0.75)

0.0200

Local optimization option (0=No, 1=Yes)

1

Convergence limit for relative change in RMS error in percent (0.1 to 20)

5.0000

Minimum change in RMS error for line search in percent (0.5 to 100)

0.5000

Number of iterations (1 to 30)

7

Vertical to horizontal flatness filter ratio (0.25 to 4.0)

0.3000

Model for increase in thickness of layers(0=default 10%, 1=default 25%, 2=user defined)

2

Number of nodes between adjacent electrodes (1, 2 or 4)

4

Flatness filter type, Include smoothing of model resistivity (0=model changes only,1=directly on model)

1

Reduce number of topographical data points? (0=No,1=Yes. Recommend leave at 0)

0

Carry out topography modeling? (0=No,1=Yes)

1

Type of topography trend removal (0=Average,1=Least-squares,2=End to end)

0

Type of Jacobian matrix calculation (0=Quasi-Newton, 1=Gauss-Newton, 2=Mixed)

1



Increase of damping factor with depth (1.0 to 2.0)

1.1000

Type of topographical modeling (0=None, 1=No longer supported so do not use, 2=uniform distorted FEM, 3=underwater, 4=damped FEM, 5=FEM with inverse Swartz-Christoffel)

4

Robust data constrain? (0=No, 1=Yes)

0

Cutoff factor for data constrain (0.0001 to 0.1)

0.0500

Robust model constrain? (0=No, 1=Yes)

0

Cutoff factor for model constrain (0.0001 to 1.0)

0.0050

Allow number of model parameters to exceed data points? (0=No, 1=Yes)

1

Use extended model? (0=No, 1=Yes)

0

Reduce effect of side blocks? (0=No, 1=Slight, 2=Severe, 3=Very Severe)

1

Type of mesh (0=Normal,1=Fine,2=Finest)

2

Optimise damping factor? (0=No, 1=Yes)

1

Time-lapse inversion constrain (0=None,1&2=Smooth,3=Robust)

3

Type of time-lapse inversion method (0=Simultaneous,1=Sequential)

0

Thickness of first layer (0.25 to 1.0)

0.4159

Factor to increase thickness layer with depth (1.0 to 1.25)

1.1000

USE FINITE ELEMENT METHOD (YES=1,NO=0)

1

WIDTH OF BLOCKS (1=NORMAL WIDTH, 2=DOUBLE, 3=TRIPLE, 4=QUADRUPLE, 5=QUINTIPLE)

1

MAKE SURE BLOCKS HAVE THE SAME WIDTH (YES=1,NO=0)

1

RMS CONVERGENCE LIMIT (IN PERCENT)

0.100



USE LOGARITHM OF APPARENT RESISTIVITY (0=USE LOG OF APPARENT RESISTIVITY, 1=USE RESISTANCE VALUES, 2=USE APPARENT RESISTIVITY)

0

TYPE OF IP INVERSION METHOD (0=CONCURRENT,1=SEQUENTIAL)

0

PROCEED AUTOMATICALLY FOR SEQUENTIAL METHOD (1=YES,0=NO)

0

IP DAMPING FACTOR (0.01 to 1.0)

0.250

USE AUTOMATIC IP DAMPING FACTOR (YES=1,NO=0)

0

CUTOFF FACTOR FOR BOREHOLE DATA (0.0005 to 0.02)

0.00010

TYPE OF CROSS-BOREHOLE MODEL (0=normal,1=halfsize)

0

LIMIT RESISTIVITY VALUES(0=No,1=Yes)

1

Upper limit factor (10-50)

50.000

Lower limit factor (0.02 to 0.1)

0.020

Type of reference resistivity (0=average,1=first iteration)

0

Model refinement (1.0=Normal,0.5=Half-width cells)

1.00

Combined Combined Marquardt and Occam inversion (0=Not used,1=used)

0

Type of optimisation method (0=Gauss-Newton,2=Incomplete GN)

0

Convergence limit for Incomplete Gauss-Newton method (0.005 to 0.05)

0.005

Use data compression with Incomplete Gauss-Newton (0=No,1=Yes)

0

Use reference model in inversion (0=No,1=Yes)

0

Damping factor for reference model (0.0 to 1.0)

0.01000

Use fast method to calculate Jacobian matrix. (0=No,1=Yes)

0



Use higher damping for first layer? (0=No,1=Yes)

1

Extra damping factor for first layer (1.0 to 100.0)

5.00000

Type of finite-element method (0=Triangular,1=Trapezoidal elements)

1

Factor to increase model depth range (1.0 to 5.0)

1.000

Reduce model variations near borehole (0=No, 1=Yes)

0

Factor to control the degree variations near the boreholes are reduced (2 to 100)

5.0

Factor to control variation of borehole damping factor with distance (0.5 to 5.0)

1.0

Floating electrodes survey inversion method (0=use fixed water layer, 1=Incorporate water layer into the model)

1

Resistivity variation within water layer (0=allow resistivity to vary freely,1=minimise variation)

1

Use sparse inversion method for very long survey lines (0=No, 1=Yes)

0

Optimize Jacobian matrix calculation (0=No, 1=Yes)

0

Automatically switch electrodes for negative geometric factor (0=No, 1=Yes)

1

Force resistance value to be constant with the geometric factor (0=No, 1=Yes)

0

Shift the electrodes to round up positions of electrodes (0=No, 1=Yes)

0

Use difference of measurements in time-lapse inversion (0=No,1=Yes)

0

Use active constraint balancing (0=No,1=Yes)

1

Type of active constraints (0=Normal,1=Reverse)

0

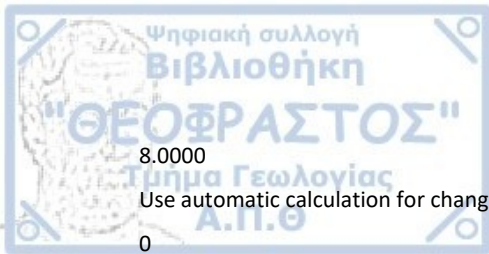
Lower damping factor limit for active constraints

0.2000

Upper damping factor limit for active constraints

2.5000

Water resistivity variation damping factor



Use automatic calculation for change of damping factor with depth (0=No,1=Yes)

0

Type of I.P. model transformation (0=None, 1=square root, 3=range)

1

Model Chargeability Lower Limit (mV/V) for range

0.00

Model Chargeability Upper Limit (mV/V) for range

900.00

Use I.P. model refinement (0=No, 1=Yes)

1

Weight for I.P. data (1 to 10)

1.00

I.P. model damping factor (0.05 to 1.0)

0.25

Use program estimate for I.P. model damping factor (0=No, 1=Yes)

0

Type of I.P. smoothness constraint (1=Same as resistivity, 0=Different)

1

Joint or separate I.P. inversion method (1=Separate, 0=Joint)

1

Apparent I.P. cutoff value (300 to 899 mV/V)

899.00

Use diagonal filter (0=No, 1=Yes)

0

Diagonal filter weight (0.2 to 5.0)

1.00

Limit range of data weights from error estimates? (0=No, 1=Yes)

0

Lower limit of data weights (0.2 to 0.5)

0.30

Upper limit of data weights (2.0 to 5.0)

3.00

Use same data weights from error estimates for different time series? (0=No, 1=Yes)

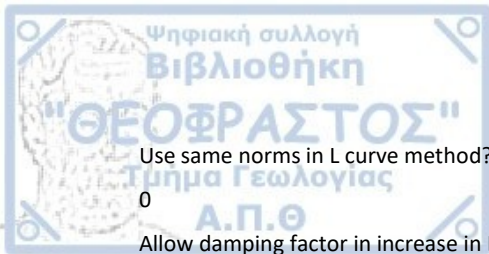
0

Calculate model resolution? (0=No, 1=Yes)

0

Use L curve method? (0=No, 1=Yes)

0



Use same norms in L curve method? (0=No, 1=Yes)

0

Allow damping factor in increase in L curve method? (0=No, 1=Yes)

1

Type of borehole damping method (0=Horizontal distance from nearest borehole, 1=Distance from nearest active electrode)

0

Use fast Jacobian calculation for dense data sets? (0=No,1=Yes)

0

Use higher damping factors at sides of model? (0=No,1=Yes)

1

Adjust damping factors for distances between the blocks in the model? (0=No,1=Yes)

1

Number of electrodes in segment for sparse inversion method for very long survey lines.

250

Time-lapse damping factor.

0.25

Reduce time-lapse damping with each iteration? (0=No,1=Yes)

1

Filter input data using gemetric factor? (0=No,1=Yes)

0

Automatically remove negative apparent resistivity values? (0=No,1=Yes)

0

Automatically remove Gamma type arrays? (0=No,1=Yes)

0

Topography distortion damping factor (0.1 to 2.0)

0.750

Use zero reference I.P. model value? (0=No, 1=Yes)

0

2) Dynamic Olous Data Set Inversion Parameters

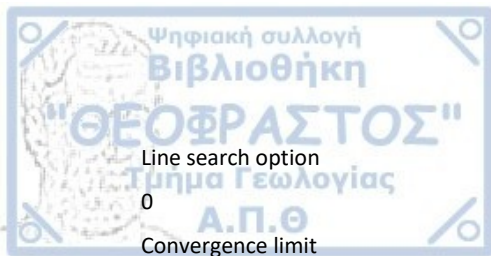
Inversion settings

Initial damping factor

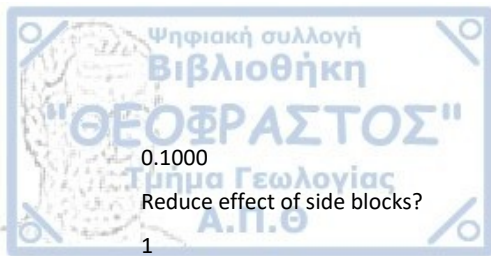
0.1000

Minimum damping factor

0.0100



5.0000
Minimum change in RMS error
0.2000
Number of iterations
5
Number of iterations to recalculate Jacobian matrix
100
Vertical to horizontal flatness filter ratio
0.5000
X horizontal flatness filter weight
1.0000
Y horizontal flatness filter weight
1.0000
Flatness filter weight for half-size layers
1.0
Number of nodes between adjacent electrodes
2
Normalise potentials
0
Flatness filter type, Include smoothing of model resistivity
0
Increase of damping factor with depth
1.0100
Type of topographical modeling
0
Factor for damped topography model
0.50
Type of topography trend removal
0
Robust data constrain?
1
Cutoff factor for data constrain
0.1000
Robust model constrain?
1
Cutoff factor for model constrain



Optimise damping factor?

0

Thickness of first layer

0.3500

Factor to increase thickness layer with depth

1.1000

Number of half-size layers

0

Divide half-size layers vertically (1=YES,0=NO)

0

Factor to increase model depth range

1.0000

USE FINITE ELEMENT METHOD (YES=1,NO=0)

1

RMS CONVERGENCE LIMIT (IN PERCENT)

5.000

USE LOGARITHM OF APPARENT RESISTIVITY (0=LOG OF APP. RESIS., 1=RESISTANCE, 2=APP. RESIS.)

0

TYPE OF IP INVERSION METHOD (0=CONCURRENT,1=SEQUENTIAL)

1

PROCEED AUTOMATICALLY FOR SEQUENTIAL METHOD (1=YES,0=NO)

1

IP DAMPING FACTOR

0.250

USE AUTOMATIC IP DAMPING FACTOR (YES=1,NO=0)

0

CUTOFF FACTOR FOR LOW POTENTIALS (0.0005 to 0.02)

0.00010

LIMIT RESISTIVITY VALUES(0=No,1=Yes)

1

Upper limit factor (10-50)

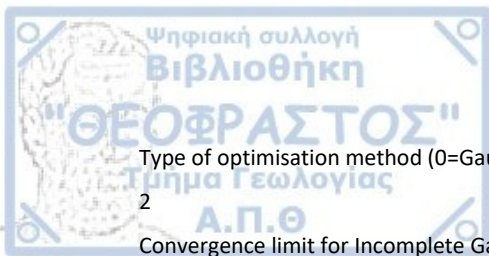
50.000

Lower limit factor (0.02 to 0.1)

0.020

Type of reference resistivity (0=average,1=first iteration)

0



Type of optimisation method (0=Gauss-Newton,2=Incomplete GN)

2

Convergence limit for Incomplete Gauss-Newton method

0.01000

Use data compression with Incomplete Gauss-Newton (0=No,1=Yes)

0

Use reference model in inversion (0=No,1=Yes)

0

Damping factor for reference model

0.07000

Type of initial model (0=Homogeneous,1=approx.inverse)

0

Time-lapse inversion constrain

1

Type of time-lapse inversion method

0

Type of time reference model,0=first,1=preceding

0

Reduce effect of side blocks? (0=No,1=Yes)

1

Use higher damping for first layer? (0=No,1=Yes)

1

Extra damping factor for first layer

5.00000

Automatically re-sort data points (0=No, 1=Yes)

1

Automatically switch electrodes for negative geometric factor (0=No, 1=Yes)

1

Automatically force apparent resistivity values to be positive (0=No, 1=Yes)

0

Scale Incomplete Gauss-Newton method (0=No, 1=Yes)

1

Type of scaling for Incomplete Gauss-Newton method (1=First, 1=Second 3=Third order)

1

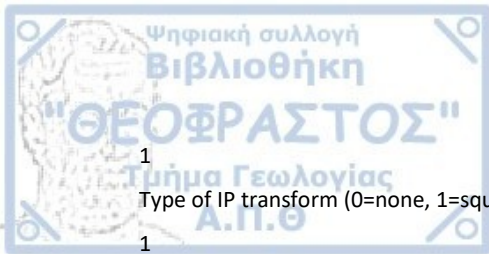
Use uniform filter weights (0=No, 1=Yes)

1

Type of data compression (0=Simple, 1=Aggressive)

1

Type of IP constraints (0=always smooth, 1=same as resistivity)



1
Type of IP transform (0=none, 1=square-root, 3=range)

1

Lower limit for IP model value (-50 to +10 mV/V)

0.0

Upper limit for IP model value (650 to 900 mV/V)

800.0

Optimize use of CPU cache (0=No, 1=Yes)

1

Precision of cache optimization routines (0=Standard, 1=High)

1

Use parallel SSE computations (0=No, 1=Yes)

1

Use multi-core support (0=No, 1=Yes)

1

Reference model resistivity multiplication factor (0.1 to 10)

1.00

Disable convergence checking (0=No, 1=Yes)

0

Try to optimise model at each iteration (0=No, 1=Yes)

0

Use approximate IP inversion (0=No, 1=Yes)

0

Use horizontal diagonal filter (0=No, 1=Yes)

0

Use vertical diagonal filter (0=No, 1=Yes)

0

Use vertical cross-diagonal filter (0=No, 1=Yes)

0

Long electrode inversion mesh settings (0=Use same size, 1=Use smaller mesh)

0

Point electrode inversion settings (0=Use nearest nodes, 1=Use distorted grid)

0

Use more than 8GB RAM for finite-difference and finite-element methods (0=No, 1=Yes)

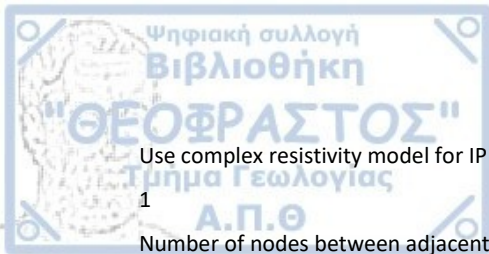
1

Type of time lapse inversion constraint (0=None,1=Smooth,2=Blocky)

1

Cross time model damping factor

0.2000



Use complex resistivity model for IP inversion (0=No, 1=Yes)

1

Number of nodes between adjacent borehole electrodes

2

Use active constraints (0=No, 1=Yes)

0

Type of active constraints

0

Parameters used for active constraints

0

Minimum damping for active constraints

0.000

Maximum damping for active constraints

0.000

Weight for diagonal components

1.000

Use optimized forward modeling routines for sparse electrodes (0=No, 1=Yes)

1

Use optimized routines for Intel CPUs (0=No, 1=Yes)

1

Use fast Jacobian calculation for dense data sets (0=No, 1=Yes)

0

Use assembly language subroutines? (0=No, 1=Yes)

1

Calculate model resolution? (0=No, 1=Yes)

0

Type of method to estimate topography. (0=Nearest 4 points, 1=All points)

1

Use apparent IP data in resistivity inversion. (0=No, 1=Yes)

0

Use direct calculation of IP Jacobian matrices. (0=No, 1=Yes)

1

Use geometric factor relative error to remove unstable arrays? (0=No, 1=Yes)

1

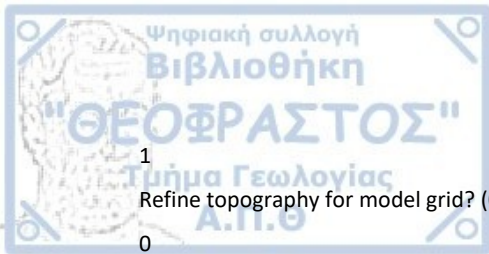
Geometric factor relative error cutoff values. (3 to 15)

5.00

Use extended boundary nodes for mesh? (0=Standard, 1=Medium, 2=Highly)

0

Use SSE registers in multi-CPU workstations? (0=No, 1=Yes)



1
Refine topography for model grid? (0=No, 1=Yes)

0

Vertical mesh size (0=Default,1=Finer,2=Finest)

0

Reduce time-lapse damping factor after each iteration (0=No,maintain constant value,1=Yes,reduce)

1

Precision of calculations to solve least-squares equation using direct Gauss-Newton method (0=Double,1=Single)

0

Type of reference model constraint (0=uniform,1=adaptive)

0

Try to load all potentials into RAM for Jacobian calculation (0=No, 1=Yes)

1

Use AVX instructions (0=SSE, 1=AVX, 2=FMA/AVX2)

0

Use combined Marquardt and Occam inversion (0=No, 1=Yes)

0

Weight for Marquardt method

0.100

Value of data compression cut-off factor (0.001 to 0.01)

0.00200

Automatically remove negative calculated apparent resistivity when using logarithm? (0 or 1)

0

Extend range of horizontal filter? (0,1,2)

0

Use the same reference damping factor for the I.P. model? (0=No,1=Yes)

1

I.P. damping factor value (0.01 to 1.00)

0.070

Use zero reference I.P. model value? (0=No, 1=Yes)

0

Default number of extra iterations to add (0 to 10)

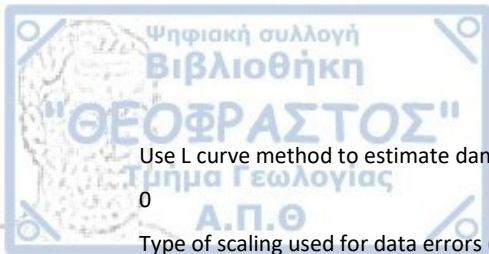
1

Use amplitude of potentials in non-linear complex resistivity forward model to calculate apparent resistivity and IP values. (0 or 1)

0

Automatically continue inversion when number of iterations reached for models with large meshes if program has not converged? (0 or 1)

1



Use L curve method to estimate damping factor? (0 or 1)

0

Type of scaling used for data errors (0=average weights 1.0, 1=minimum weight 1.0)

0

Automatically reset settings for pole-pole data? (0 or 1)

1

Number of times to subdivide mesh in x-direction (1 to 5)

1

Number of times to subdivide mesh in y-direction (1 to 5)

1

Number of model blocks to extend subdivided mesh (1 to 6)

5

Type of approximation of Jacobian values of model blocks for data points outside segment. (0 or 1)

1

Calculate point-spread function and covariance matrix? (0 or 1)

0

Reduce variations near electrodes using sensitivity values? (0 or 1)

0

Damping factor increase to reduce variations

4.000

Rate of damping factor reduction with sensitivity

2.500

Cutoff sensitivity values to set higher damping factor (0.10 to 0.60)

0.200

Number of bottom buffer nodes (6 to 14)

12

End of file